Wall-Resolved Large Eddy Simulation of a Wing-Body Junction

High-Fidelity Data Generation for Data-Driven Turbulence Modelling

J.A. Alberts

Supervisor
Dr. Richard Dwight
Associate Professor
Aerodynamics Research Group
Faculty of Aerospace Engineering, TU Delft
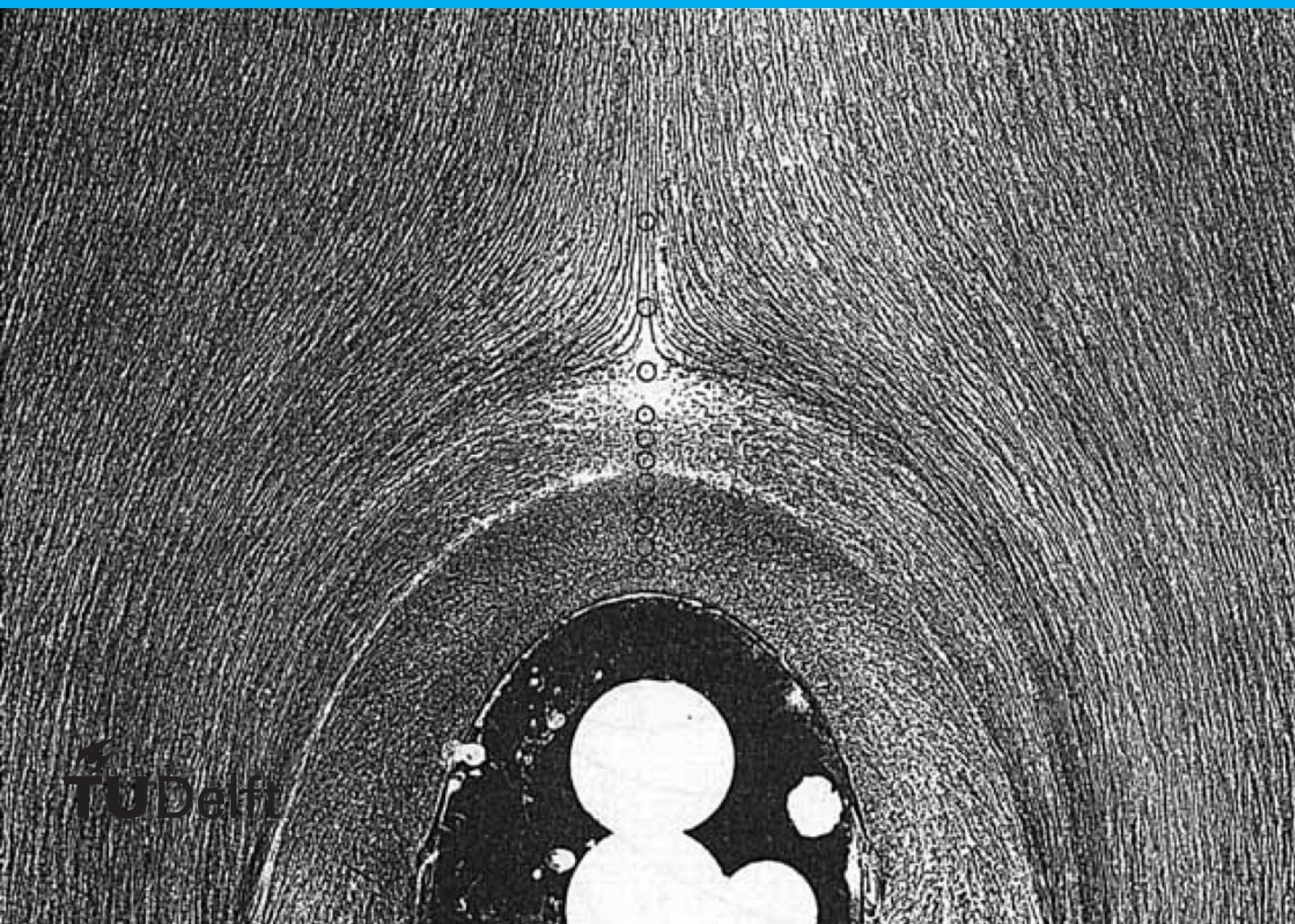
Wall-Resolved Large Eddy Simulation of a Wing-Body Junction

High-Fidelity Data Generation for Data-Driven Turbulence Modelling

by

J.A. Alberts

to obtain the degree of Master of Science
at the Delft University of Technology,
to be defended publicly on Monday February 8, 2021 at 14:00 PM.

Student number:	4292111	
Project duration:	September 17, 2019 – February 8, 2021	
Thesis committee:	Dr. R. P. Dwight,	TU Delft, supervisor
	Prof. Dr. Ing. G. Eitelberg ,	TU Delft
	Dr. S. J. Hulshoff ,	TU Delft
	Dr. D. Modesti,	TU Delft

An electronic version of this thesis is available at `http://repository.tudelft.nl/`.

TUDelft Delft University of Technology

Acknowledgements

Abstract

A wall-resolved Large Eddy Simulation (LES) of a wing-body junction is performed. The aim is to generate high-fidelity junction flow data to be used in a data-driven turbulence modelling approach, specifically to improve the accuracy of RANS-simulations in junction flows. The simulation is performed on a 61.5 million C-grid body fitted mesh in the pimpleFoam solver of OpenFOAM, with a turbulent channel flow precursor providing the unsteady inlet boundary condition. Analysis of the wall-resolved LES shows that the simulation accurately captures the complex flow phenomena in the wing-body junction flow including intermittency for the present inflow condition. Comparisons of the wall-resolved LES with a coarse-grid RANS simulation and the wall-modelled LES of Srikumar [2019] show that the wall-resolved LES in the present study is an improvement over the other two numerical methods. Most notably, an improvement in terms of the prediction of the location and magnitude of the mean spanwise vorticity and the mean turbulent kinetic energy of the horseshoe vortex systems was observed. Especially the RANS-simulation was unable to accurately capture the complex flow physics in the junction due to the limitations of RANS-methods, which are unable to accurately capture Reynolds stress anisotropy due to the Boussinesq hypothesis. An analysis of the high-fidelity junction flow data was performed to indicate regions where the Boussinesq hypothesis breaks down. The most notable region where the Boussinesq hypothesis was found to be not valid, was the region in close proximity to the wing-body junction upstream of the wing. Due to the breakdown of the Boussinesq hypothesis in the junction region, significant improvements of the accuracy of junction flow RANS-simulations can potentially be achieved by using the high-fidelity data from the present study in a data-driven turbulence modelling approach.

Contents

List of Symbols

Abbreviations

BF	Bluntness Factor
DES	Detached Eddy Simulation
DNS	Direct Numerical Simulation
DSM	Differential Reynolds Stress Model
HSV	Horseshoe Vortex
LES	Large Eddy Simulation
LEVM	Linear Eddy-Viscosity Model
MDF	Momentum Deficit Factor
NLEVM	Non-Linear Eddy-Viscosity Model
RANS	Reynolds-Averaged Navier Stokes
TCF	Turbulent Channel Flow

Greek symbols

δ	Boundary Layer Thickness	[m]
$\delta*$	Displacement Thickness	[m]
ϵ	Dissipation Rate	$[\frac{\text{m}^2}{\text{s}^3}]$
$\gamma_{a_{ij}S_{ij}}$	Angle of alignment between a_{ij} and S_{ij}	$[-]$
κ	von Kármán constant	$[-]$
Λ	Sweep Angle	$[°]$
μ	Dynamic Viscosity	$[\text{Pa} \cdot \text{s}]$
ν	Kinematic Viscosity	$[\frac{\text{m}^2}{\text{s}}]$
ν_t	Eddy Viscosity	$[\frac{\text{m}^2}{\text{s}}]$
ω	Specific Dissipation Rate	$[\frac{\text{m}^2}{\text{s}^3}]$
ρ	Density	$[\frac{\text{kg}}{\text{m}^3}]$
τ_w	Wall Shear Stress	$[\frac{\text{N}}{\text{m}^2}]$
θ	Momentum Thickness	[m]

Latin symbols

a_{ij}	Reynolds Stress Anisotropy Tensor	$[\frac{\text{m}^2}{\text{s}^2}]$
b_i	Width of the Inflow Patch	[m]
b_p	Width of the Precursor	[m]
c	Chord Length	[m]
C_f	Friction Coefficient	$[-]$
D	Obstacle Diameter	[m]
f_i	Body Forces	[N]
g_j	Gradient of the Streamline-aligned Velocity	$[\frac{1}{\text{s}}]$
H	Form Factor	$[-]$
h_i	Height of the Inflow Patch	[m]
h_p	Height of the Precursor	[m]
k	Turbulent Kinetic Energy	$[\frac{\text{m}^2}{\text{s}^2}]$
l	Obstacle Height	[m]
l_p	Length of the Precursor	[m]
m	Marker function of Gorlé et al. [2014]	$[-]$

p	Pressure	[Pa]
R_0	Leading Edge Radius	[m]
Re	Reynolds Number	[−]
S_{ij}	Mean rate-of-strain tensor	$[\frac{1}{s}]$
s_j	Unit Velocity Vector along the streamline	$[\frac{1}{s}]$
S_T	Maximum distance from the leading edge to the location of maximum thickness of the wing	[m]
T	Thickness of the obstacle	[m]
U	Velocity	$[\frac{m}{s}]$
U_∞	Freestream Velocity	$[\frac{m}{s}]$
$\overline{u_i u_j}$	Reynolds Stress Tensor	$[\frac{m^2}{s^2}]$
u^+	Non-Dimensional Velocity	[−]
u_τ	Friction Velocity	$[\frac{m}{s}]$
x_s	Location of the separation line	[m]
X_T	Chord-wise location of the maximum thickness of the wing	[m]
x_v	Location of the vortex core	[m]
y	Wall Distance	[m]
y^+	Non-Dimensional Wall Distance	[−]

1

Introduction

Junction flows are encountered in many engineering applications. A few examples of these kind of junction flows are the wing-body junction on an aircraft, hull-appendage flow on a ship, electrical component cooling and river/bridge flows. The flows around these junctions are highly complex interfering flows with three-dimensional separations. These separations are caused due to the combination of the boundary layer upstream of the junction interacting with the boundary layer that develops on the obstacle and the high adverse pressure-gradient due to the presence of the obstacle, see Gand et al. [2010b].

The drag induced due to the presence of junctions is estimated to be approximately 5% of the total drag of subsonic transport aircraft, see Filippone [2000]. Therefore, it is of key importance for aircraft manufacturers to understand the behaviour of these complex junction flows to minimise the so called interference drag. An example of an effective solution to reduce interference drag is the application of leading edge fillets/fairings at wing-body junctions, see Devenport et al. [1992a].

Due to the importance of understanding the behaviour of junction flows, a large amount of research has been done to study the wing-body junction, both experimentally and numerically. The experiments of Devenport and Simpson [1990] investigates the behaviour of the turbulent boundary layer as it encounters a cylindrical wing-body junction to understand this complex three-dimensional flow. Next to the fact that these experiments help to understand the complex phenomena in junction flows, they are often used to assess the validity of numerical simulations. For instance, Apsley and Leschziner [2001] tested the validity of a variety of RANS turbulence models to predict the complex flow around a wing-body junction. It was found that these models could not accurately predict the complex flow phenomena. Alternatively, Ryu et al. [2016] showed by performing a Large Eddy Simulation (LES) of a junction flow, that high-fidelity methods can better predict these complex flows. However, performing high-fidelity simulations is computationally expensive and can therefore not be used for design purposes.

Due to the assumptions made in deriving the Reynolds-Averaged Navier Stokes equations combined with the procedure to find closure models, RANS methods have limitations in their prediction capabilities of flows around complex geometries. As a result of the increase in computational power and the availability of large and diverse data sets, research has been focused on informing turbulence models with data to enhance and improve performance of these models. Informing of turbulence models by data is done by means of machine learning, see Duraisamy et al. [2019].

Due to the fact that there is no database of high-fidelity junction flow data available in literature which can be used for data-driven turbulence modelling, the main goal of the thesis will be to generate a high-fidelity data set for a data-driven turbulence modelling approach to improve the accuracy of RANS simulations in junction flows. This will be achieved by performing a wall-resolved Large Eddy Simulation (LES) of the wing-body junction originally studied experimentally by Devenport and Simpson [1990].

This report is structured as follows: Chapter 2 presents the literature review focusing on the research in the field of junction flows. Also, a section on data-driven turbulence modelling will be presented. The research objective and research questions which are formed based on the literature review are presented in Chapter 3. Chapter 4 presents the numerical methodologies used to conduct the numerical studies of the present research. Followed, by the results of these numerical studies presented in Chapter 5. Finally, the conclusions and recommendations are presented in Chapter 6.

2

Literature Review

In this chapter, the literature review will be presented. The goal of the literature review is to get a better understanding of junction flows and to investigate the gaps in literature. The structure of this chapter will be as follows: First, the physics of junctions flows will be presented and their common flow features. This is followed by a section which presents the numerical studies which are conducted on junction flows. Here, a distinction is made between RANS, DES and LES simulations. Finally, a section is presented on methods to control and minimise the interference drag due to the junction. In the final section of this literature review, a short introduction to machine learning turbulence modelling will be given as the data generated in this project has the objective to be employed in a data-driven turbulence model.

2.1. Physics of Junction Flows

Junction flows are complex three-dimensional flows which are commonly encountered in various engineering applications such as wing-body junctions. The dominating flow feature which is characteristic for a junction flow is called the horseshoe vortex (HSV), which is created by the combination two effects, see Fleming et al. [1993]. The first effect is due to the large adverse pressure gradient in streamwise direction created by the obstacle, which causes roll up of the fluid and generates multiple horseshoe vortices. The primary vortices have the same rotational orientation as the vorticity in the approaching boundary layer. To preserve streamline topology, secondary vortices have opposite vorticity, see Simpson [2001]. The second effect that creates this flow structure is due to the transverse vorticity in the incoming turbulent boundary layer getting skewed and stretched as it is convected past the obstacle. These legs of spanwise vorticity on each side of the obstacle have opposite direction, as can be seen from Figure 2.1, which describes schematically a horseshoe vortex. Bradshaw [1987] describes the process of the generation of streamwise vorticity, given a shear layer with spanwise vorticity, as Prandtl's secondary flow of the first kind. Once the vorticity has been generated, the vorticity typically gets diffused and reduced by the Reynolds stresses and viscous stresses.

The vortices are unsteady in size, location, circulation and number. Simpson [2001]; Furthermore, these vortices induce velocity components on their neighbouring (secondary) vortices and on themselves. As a result, diffusion of vorticity, due to Reynolds stresses and viscous stresses, may result in the merger of vortices to a combined vortex. Alternatively, vortices may move helically around one another as they move downstream under certain conditions.

The junction flow can be visualised by means of oil-flow visualisation methods, such as presented in Figure 2.2. In the figure, there are a few points of interest. In Figure 2.2a, the first point of interest is the saddle point, located at X/T=-0.47. Devenport and Simpson [1990] refers to this as the line of separation, which is caused due to the large adverse pressure gradient near the leading edge of the obstacle which causes the flow to separate. Closer to the leading edge, at X/T = -0.28, one can see the line of low shear cross the symmetry plane. Unlike, the separation line, in the line of low shear, streamlines do pass the line, indicating the difference between the two lines. This results in two distinct regions, the first region is close to the wing and is a region with a high stream-wise shear due to strong flow reversal near the leading edge of the wing as an effect of the horseshoe vortex. The second region is between the saddle point and the line of low shear and is a region of low shear. Finally, Devenport and Simpson [1990] observed a line of separation and a line of attachment on the wing and the wall, respectively, close to the wing at X/T =-0.025. Dickinson [1986],
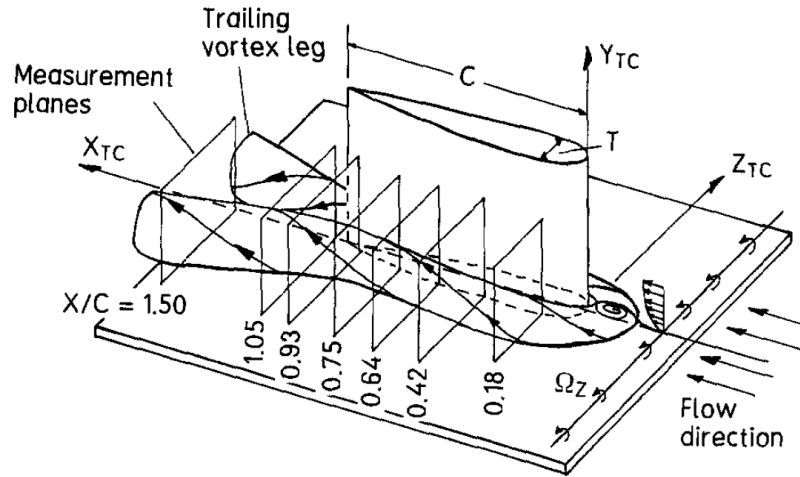
Figure 2.1: Representation of a horseshoe vortex around a wing-body junction.Fleming et al. [1993]

observed in this area a small counter rotating corner vortex.

At the trailing edge of the wing, Dickinson [1986] observed a "V-like" shape as depicted in Figure 2.2b. This "fish tail" structure was also observed by Fleming et al. [1993] and Ölcmen and Simpson [1995]. They explain the fish tail structure due to the pressure recovery at the trailing edge, resulting in a reduced streamwise velocity, and the presence of the horseshoe vortex, which induces spanwise velocities, and thus, resulting in a deflection of the flow.
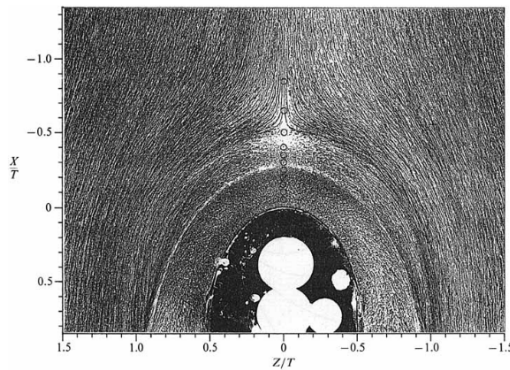
(a) Oil-flow visualisation of the line of separation and line of low shear. Results from Devenport and Simpson [1990].
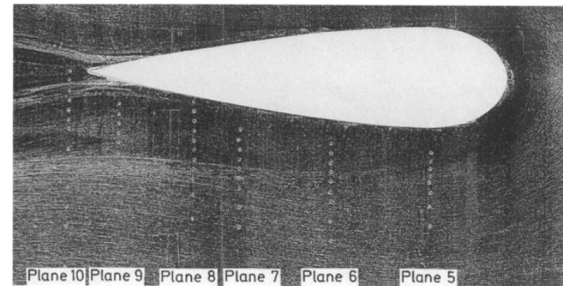
(b) Oil-flow visualisation of the fish tail shape at the trailing edge. Results from Fleming et al. [1993]

Figure 2.2: Oil-flow visualisations of the junction flow.

2.1.1. Parameters affecting the junction flow

Research of Fleming et al. [1993] introduced a new parameter to quantify the effects of the moment thickness of the boundary layer and the thickness of the obstacle on the junction flow structure. This new parameter is the Momentum Deficit Factor (MDF) and is presented in (2.1), which is a function of the Reynolds number based on the thickness of the obstacle, Re_T, the momentum thickness of the boundary layer, θ, and the thickness of the obstacle, T:

$$MDF = (Re_T)^2 \left(\frac{\theta}{T} \right). \tag{2.1}$$

For a higher MDF, Fleming et al. [1993], observed the following effects on the flow: smaller streamwise velocity distributions, vorticity is concentrated closer to the wall, the vertical distance of the vortex core is decreased and the spanwise separation of the horseshoe vortex its legs is increased in wake region. Furthermore, the vortex structure is more elliptical and the non-dimensional core vorticity increases. Fleming et al.
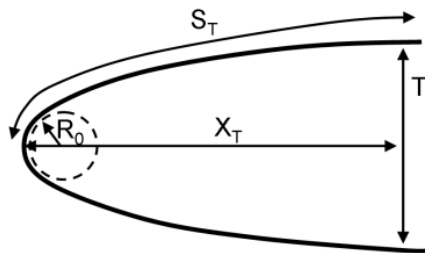
Figure 2.3: Geometrical representation of the Bluntness Factor parameters.Gand et al. [2010a]

[1993]; If the HSV is located close enough to the wall, the vorticity will be rapidly diffused due to the Reynolds stresses and viscous stresses, see Bradshaw [1987].

It was found by various authors that the geometry of the leading edge of the wing affects the strength and position of the horseshoe vortex. Kubendran et al. [1986] found that the path of the horseshoe vortex and the strength of the vortex is dependant on the slenderness of the wing leading edge. Furthermore, Mehta [1984] found experimentally that for appendages with a higher bluntness, the horseshoe vortex was stronger and more structured, by testing various appendage nose shapes. Fleming et al. [1991] introduced the Bluntness Factor (BF) to quantify the effect of the leading edge geometry on the strength and size of the horseshoe vortex. The parameters which are used to define the Bluntness Factor are described in Figure 2.3. R_0, is the leading edge radius, X_T, is the chord-wise location of the maximum thickness of the wing, T. S_T is the maximum distance from the leading edge to the location of maximum thickness along the wing. The bluntness factor is defined in (2.2):

$$BF = \frac{1}{2} \frac{R_0}{X_T} \left(\frac{T}{S_T} + \frac{S_T}{X_T} \right).$$

(2.2)

The effect of the angle of attack on the junction flow is investigated by several authors. Shizawa et al. [1996] investigated the effect of the angle of attack on the flow around a constant-thickness cylindrical wing with a semi-circular nose. For an increasing angle of attack, it was observed on the suction side of the airfoil that the horseshoe vortex remained at the same vertical distance from the wall, but moved away from the wing in the streamwise direction. Furthermore, increased levels of turbulent kinetic energy and shearing stresses were observed. At the pressure side, it was observed that the centre of the leg of the horseshoe vortex moved away (vertically) from the wall, but remained at the same distance of the wing.

Wood and Westphal [1992] reported that the pressure distribution near the leading edge of a lifting wing-body junction was only slightly affected. Furthermore, the HSV-leg at the suction side of the wing was found to be always stronger.

Ahmed and Javed Khan [1995] did research on the effect of the wing sweep angle on the junction flow at zero angle of attack. Both forward and backward sweep were analysed. It was found that in the plane of symmetry, the primary and secondary separation points were strongly affected by wing sweep. The vortex moves towards the geometry for backsweep, and away from the geometry for forward sweep. San et al. [2014] investigated the effect of several wing sweep angles at several angles of attack. Four horseshoe vortex modes were identified: separation, attached, bubble and bluff-body wake mode. At an angle of attack below 5 degrees and at a sweep angle below 12 degrees backsweep, separation occurs. For a wing with backsweep at a low angle of attack, the attached mode occurs. The bluff-body mode happens at a high angle of attack and a forward swept wing ($\Lambda<0°$) and the bubble mode occurs at high sweep angle (forward and backward) and high angles of attack.

Baker [1979] looked experimentally at the horseshoe vortex formed by a separating laminar boundary layer. For a horseshoe vortex system formed by the separation of the laminar boundary layer around a cylinder, Baker [1979] proposed that the non-dimensional location of the centre of the vortex core $\frac{x_v}{D}$ from the centre of the cylinder in the plane of symmetry and the non-dimensional location of the separation line, $\frac{x_s}{D}$, are a function of the variables presented in (2.3):

$$\frac{x_v}{D}, \frac{x_s}{D} = \text{fn}\left(\frac{UD}{v}, \frac{D}{l}, \frac{D}{\delta^*} H, \frac{u'_y}{U}\right).$$
(2.3)

In this equation, D is the obstacle diameter, l is the obstacle height, U is the freestream velocity of the fluid, δ^* is the boundary layer displacement thickness, H is form factor, u'_y is the the turbulence distribution in the boundary layer and v is the kinematic viscosity. In the experiments, Baker varied $\frac{UD}{v}$ and $\frac{D}{\delta^*}$, assuming that the variation of H and $\frac{D}{l}$ is small. Furthermore, u'_y was not be varied in the experiment. For increasing the Reynolds number in the laminar region, three different HSV systems were observed: steady HSV systems with 2, 4 and 6 vortices as the Reynolds number increases, HSV systems with regular oscillatory behaviour and HSV systems with irregular unsteady behaviour. The location of primary HSV in a steady system, $\frac{x_v}{D}$ increases with the Reynolds number and decreases with $\frac{D}{\delta^*}$. A similar research was carried out by Baker [1980] for the turbulent boundary layer. It was found that the location of the separation line decreases as $\frac{U\delta^*}{v}$ increases and $\frac{D}{\delta^*}$ increases.

2.1.2. Bimodal Behaviour of the Horseshoe Vortex

Large turbulent stresses near the vicinity of the junction vortex cannot be explained simply by means of conventional turbulent mixing. Devenport and Simpson [1990] were the first to explain this behaviour by means of a bimodal (double-peaks) probability-density functions of U- and V-velocities in the region of the mean vortex due to the low-frequency bimodal oscillations of the horsehsoe vortex system. These pdfs are produced by the velocity variation over time which switches between two states, a backflow mode, which has a large negative U-velocity, and a zero-flow mode, which has a U-velocity close to zero. This bimodal behaviour causes high pressure fluctuations and high heat transfer rates in the region of the junction. Simpson [2001];

In Figure 2.5, the probability density functions for the U-velocity fluctuations for various values of Y/T at a given value of X/T of the experiments of Devenport are shown. The pdfs are approximately Gaussian for Y/T larger than 0.05. For, Y/T<0.05, the bimodal behaviour of the probability density function can be observed. Depending on the height of the measurement, the biomodal pdf's have a different shape, however, always one peak is always centered close to zero and the second peak is always negative, indicating the the zero-flow mode and the backflow mode respectively. In Figure 2.4, the dashed line shows the extend of the bimodal region for the U-velocity component.

Bimodal pdf's are also present for the V- and (U-V)-velocity fluctuations but not for the W-velocity fluctuations. The peaks of these biomodal regions for the V- and (U-V)-velocity fluctuations are found at different locations of the probability density functions. In order to identify the peaks corresponding to the correct flowmodes (backflow mode and zero-flow mode), the area of a peak in the V-velocity fluctuations pdf should correspond to the area of the corresponding flow mode in the U-velocity fluctuation pdf. From the pdf's with U- and V- velocity fluctuations, a velocity vector field for the backflow mode and zero-flow mode can be generated and are indicated in Figure 2.4a and Figure 2.4b, respectively. Note in these figures that only the bimodal region, indicated by the dashed line in these figures, changes.

Several other authors identified and looked into the bimodal behaviour of the junction flow. Rife et al. [1992], observed the same bimodal behaviour as observed by Devenport and Simpson [1990]. Furthermore, Rife et al. [1992] observed an increase of the pressure fluctuations in the bimodal region. The characteristic unsteadiness is produced by turbulent structures with a low frequency between $\frac{fT}{U}$ of $6x10^{-3}$ and 0.5. The following authors identified the bimodal behaviour of the junction flow in their numerical experiments: DES of Paik et al. [2007], LES of the flow around a cylinder of Kirkil et al. [2008], LES of Gand et al. [2010a] around a simplified wing body junction and in LES simulations of Ryu et al. [2016].
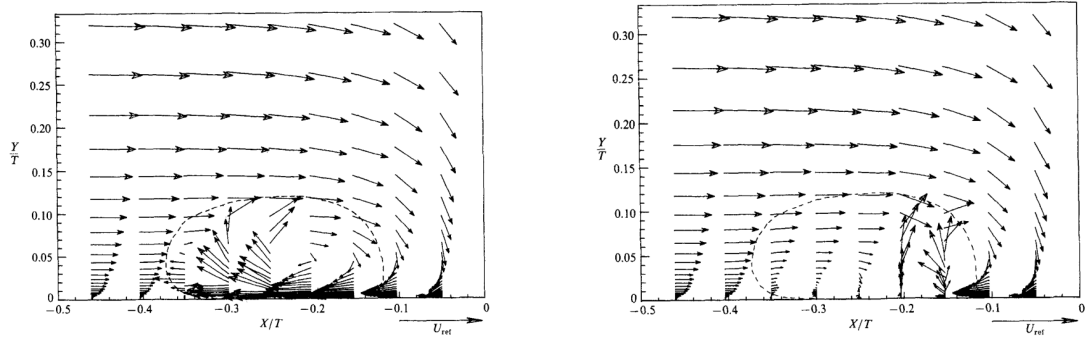
(a) Velocity vectors of the backflow mode. The dashed line indicates the extent of the biomodal region.

(b) Velocity vectors of the zero-flow mode. The dashed line indicates the extent of the biomodal region.

Figure 2.4: Velocity vectors of the two flow modes from Devenport and Simpson [1990]
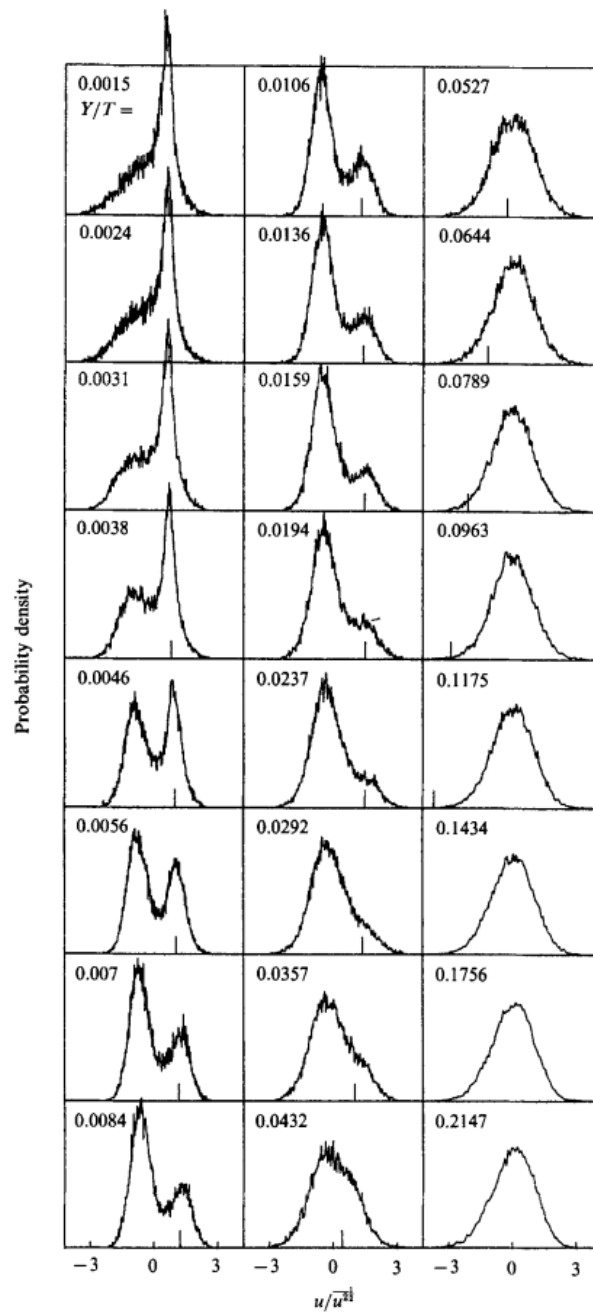
Figure 2.5: Probability Density Functions for U-velocity fluctuations from the experiments of Devenport and Simpson [1990]. Measurements taken at X/T=-0.2 and Z/T=0.0 for varying Y/T.

Figure 2.6: Oil-flow visualisation of the corner separation at a pitch angle of 5 degrees of the NASA experiment. Kegerise et al.;

2.1.3. Corner Separation

A lesser investigated area of the junction flow is the area near the trailing edge of the junction, where corner separation can occur. Fundamental research of Gessner [1973] shows that the transverse gradients of the Reynolds shear stresses are responsible for the corner separation. Gessner refers to the corner separation as Prandtl's secondary flow of the second kind. Barber [1978] was the first to investigate intersection losses in junction flows. They suggested that intersection losses are dominated by the size of the horseshoe vortex and the incoming boundary layer thickness. A thin incoming boundary layer would result in large intersection losses.

In a study of Gand et al. [2010a], an experimental, RANS and LES investigation into a wing-body junction was carried out. In the experimental campaign, no corner separation was observed, however, RANS simulations did predict corner separation. This shows the lack of accuracy of RANS in these complex flow fields. Dandois [2014], implemented a quadratic constitutive relation in the Reynolds-averaged Navier-Stokes equations, to improve the prediction of corner flow separation. It was found that the implementation of the quadratic constitutive relation improved the prediction of corner flow separation without affecting the rest of the simulation.

A study of Gand et al. [2010b] shows that the understanding of the corner separation is limited. The experiment of Gand et al. [2010b] was designed with a low bluntness factor, which according to literature, should be a favourable condition for corner separation. However, no corner separation was observed in the experiments. Gand et al. [2010b] suggests that an increase in the Reynolds number might affect the presence of corner separation in junction flows.

Since there is a limited understanding of corner separation and current turbulence models are unable to reliably predict the onset and extent of three-dimensional flow separations which occur in wing-body junction flows, NASA carried out an experiment at subsonic conditions for a full-span wing-fuselage model. Kegerise et al.; The geometry of the wing was specifically chosen such that with an increase in pitch of the model, the corner flow separation would change from a small volume to a large separation. The goal of the experiments was to generate a high-quality publicly available database which will ultimately help to improve the predictive capabilities of this complex flow phenomenon. An oil-flow visualisation of the corner separation is presented in Figure 2.6.

2.2. Numerical Studies of Junction Flows

Next to experimental studies, a large amount of numerical studies on junction flows have been performed. Apsley and Leschziner [2001], tested in total 12 RANS turbulence models in their capabilities of prediction the junction flow around a NACA0020 airfoil. Here, a distinction was made between Linear Eddy-Viscosity models (LEVM), Non-Linear Eddy-Viscosity Models (NLEVM) and Differential Reynolds Stress Models (DSM). These turbulence models were compared to experimental data. Comparisons were made for: pressure fields on the wall and the airfoil and comparisons were made of the velocity, turbulent kinetic energy and shear and normal stresses in the symmetry plane and in planes normal to the streamwise flow direction along and

downstream the airfoil. Overall, no close agreement was found for the RANS simulations in terms of the mean flow field and turbulence quantities when comparing the results to experimental data. However, when a comparison between the different kind of turbulence models was made, the DSM models were better in predicting the complex flow than the LEVM and NLEVM models. Furthermore, Apsley and Leschziner [2001], concluded that from the models of the LEVM type, the SST model was the model which came closes to the performance of the DSM models in terms of mean flow structures. Although, it should be noted that it was found that the SST-model is highly-sensitive to adverse-pressure gradients which cause separation.

Paciorri et al. [2005] tested two commonly used eddy viscosity models, namely, the one-equation Spalart-Allmaras model and the two-equation k-ϵ model. It was found that the size of the HSV was underestimated by both methods, however, that the results were good enough to have engineering relevance. In the experiment, the Spalart-Allmaras model performed slightly better than the k-ϵ model.

Paik et al. [2007] carried out numerical simulations of the junction flow by means of a Detached Eddy Simulation (DES) approach. The DES is a hybrid RANS/LES method which depending on the grid size is switched between RANS mode and LES mode. In standard DES, the boundary layers are treated as a URANS method. Due to the fact that the location of the HSV is located in the boundary layer close to the wall, a refinement is required to capture the HSV, resulting in the premature activation of the LES mode. As a result, Paik et al. [2007] observed flow fields in the HSV region, which were over-energised and laminar like. To tackle this issue, a lengthscale was introduced which ensured that near the wall, up to halfway between the HSV and the wall, URANS mode was active. The DES with modified lengthscale was based on a Spalart-Allmaras model and matched properly with the experimental data of the mean flow and turbulence statistics of the junction flow. Only, the location of the HSV was predicted somewhat upstream with respect to the experimental data. In the results of Paik et al. [2007], the bi-modal behaviour of the HSV was observed.

Fu et al. [2007] did a standard DES and a delayed DES, both based on a weakly nonlinear k-ω model. They reported for the standard DES simulation, similar results asPaik et al. [2007]. Hence, earlier flow separation and a more upstream location of the HSV with respect to the experimental data. However, the Delayed Detached Eddy Simulation (DDES) showed great agreement with the experimental data. This can be explained due to the fact that DDES is tuned such that close to the wall, the hybrid simulation is ensured to be in RANS mode and therefore solving the issue of mesh-induced separation which was observed in the DES of Paik et al. [2007].

In the works of Alin and Fureby [2008], RANS, DES and wall-modelled LES simulations were performed and compared to the experimental data of Pierce and Shin [1992]. In comparison with RANS and DES, improved results were obtained with the wall-modelled LES simulation. Good agreement of the separation location of the flow in front of the junction was found in the LES. Furthermore, improvement of the prediction of the HSV downstream of the obstacle was found with respect to RANS and DES results. Hence, proving the potential of LES to properly resolve the junction flow.

Ryu et al. [2016] performed a wall-resolved LES of the cylindrical "Rood" wing typically used in junction flow studies which consists of a 3:2 elliptical nose and a NACA0020 tail. They performed a course and fine grid LES. As a subgrid-scale (SGS) model, the Vreman model was used. Furthermore, a k-ω SST RANS simulation was performed and results were compared to the results of Devenport and Simpson [1990]. In terms of corner flow physics, the fine LES accurately resolved the primary vortex and three secondary vortices. The courses grid, did not resolve all the vortices and the strength of the vortices was less with respect to the fine mesh simulation. The RANS simulation did not show any of the secondary vortices, and furthermore, the primary vortex was located closer to the leading edge, more elliptically shaped and had less strength. This is explained due to the fact that linear eddy-viscosity models are limited in their capability to resolve the anisotropy of the Reynolds stresses. However, the refined LES, did properly capture the turbulence statistics and bi-modal behaviour of the junction flow. Furthermore, Ryu et al. [2016] investigated the effect of different SGS-models on the turbulence statistics. The Vreman-model, the dynamic Smagorinsky model and a SGS-model based on Volumetric-Strain Stretching (VSV) were used. They noted that qualitatively, the subgrid-scale models showed different performance. Most notably, differences were observed in rms turbulence quantities and turbulence damping near the nose of the wing-body junction.

Gand et al. [2010a] did experimental and numerical research, including both RANS and LES simulations, of a wing-body junction with a low bluntness factor to model the onset of corner separation. Even though, the conditions should have been favourable for corner separation, no corner separation was observed in the

experiments conducted by Gand et al. [2010a]. The numerical simulations showed the limitations of RANS for junction flows, as the RANS simulations predicted corner separation, even though, in the experiments, these corner separations were not present. Furthermore, Gand et al. [2010a] concluded that LES is the best way to deal with junction flows, since the results of the LES simulations were very close to those of the experiments. Furthermore, satisfactory results were also observed for LES at an angle of attack of 10 degrees.

Overall, from the studies in this literature review, it is evident that RANS can not properly capture all the flow physics of junction flows. This can be explained due to the limitations of the Boussinesq hypothesis commonly used in RANS-methods, which can not resolve the anisotropy of the Reynolds stresses. Furthermore, RANS is unable to capture any unsteadiness. In contrast of RANS, LES is able to properly capture the highly unsteady dynamics and turbulence statistics of the junction flow. Therefore, LES would be the best option to analyse junction flows numerically. The drawback of LES is the high computational cost, making it infeasible for design optimisation.

2.3. Controlling Drag in Junction Flows

One important component of the total drag of the flow around an object in junction flows is the interference drag. This drag is the component of the drag which is due to the interaction of the wing and the body. In other words, the total drag of the wing-body junction is generally higher than the individual drag of the wing and body, which is the interference drag.

According to Kubendran et al. [1984], interference drag is consists of three parts. The first part is due to the secondary flow which distorts the velocity profiles in the junction and the merging of two boundary layers, which cause an increase in the wall shear stress. Secondly, there is an induced drag component due to the loss of energy to the secondary flow structure (the horseshoe vortex) in the junction. The final component of the interference drag is due a modified growth of the viscous layer, which affects the pressure drag. Kubendran et al. [1984] found that for his experiment, the interference drag effect was small and negative. Hence, a favourable interference effect.

For subsonic transport aircraft, the interference drag is approximately 5% of the total drag. Filippone [2000] Therefore, the design of junctions is important for aircraft manufacturers. Hence, the large amount of research done over the years to minimise the effects of drag induced by junctions. An overview of this research is given below.

2.3.1. Fairings/Fillets

A common method to reduce the interference drag on aircraft is to use a fairing around the base of the wing. Devenport et al. [1990] demonstrates the effect of wrapping a fillet around the base of an idealised wing-body junction to the flow of a turbulent boundary layer. Figure 2.7a shows the fillet wrapped around the base of the wing-body junction. An uniform fillet radius of 0.53 the wing thickness was used. Devenport et al. [1990] concluded that wrapping a fillet around the base of the junction does not prevent the formation of a horseshoe vortex nor does the fillet remove the large-scale unsteady bimodal behaviour of the horseshoe vortex. Furthermore, increased spectral levels of surface pressure fluctuations are observed under the streamwise legs of the HSV. Also, the time-averaged boundary layer structure becomes more distorted due to the fillet, which could result in an increase in size and strength of the HSV. Finally, altering the angle of attack or changing the boundary layer thickness does not affect the effects caused by the fillet. From the measurements, no effects on the interference drag could be identified. Hence, a wrap-around fillet does not alter the flow around a wing-body junction in a desirable manner.

However, in contrast to the wrap-around filled, an experimental study from Devenport et al. [1992b] of an idealised wing-body junction at different angles of attack and different incoming boundary layer thicknesses showed that the implementation of a leading-edge fillet does modify the flow around the junction in a desirable way. The leading-edge fillet is a (large) fairing between the leading-edge of the wing and the surface of the body. An illustration of the leading-edge fairing is depicted in Figure 2.7b. Given that the wing-body junction was at an angle of attack of zero degrees, it was observed that for both boundary layer thicknesses, the fillet reduces the magnitude and extend of the adverse pressure gradients, which eliminates the leading-edge separation. Furthermore, the leading-edge fairing prevented the formation of the HSV, and therefore, no bimodal unsteadiness was observed. Also, a reduction of the magnitude of the surface pressure fluctuations was observed in the vicinity of the wing-body junction. Finally, a reduced skewing of the boundary layer as it passes the junction and a reduction of the non-uniformity of the wake were observed. At a non-zero angle

of attack, the fillet still modifies the flow in a desirable way, although the fillet was less effective with respect to the case at a zero angle of attack. This is because separation of the approach boundary layer occurs on the pressure side of the fillet due to local adverse pressure gradients. Furthermore, large skewing of the near-wall boundary layer occurs close to the separation region and unsteadiness on the pressure side of the wake is observed.

(a) A fillet wrapped around the base of an idealised wing-body junction.

(b) A leading-edge fillet applied to an idealised wing-body junction.
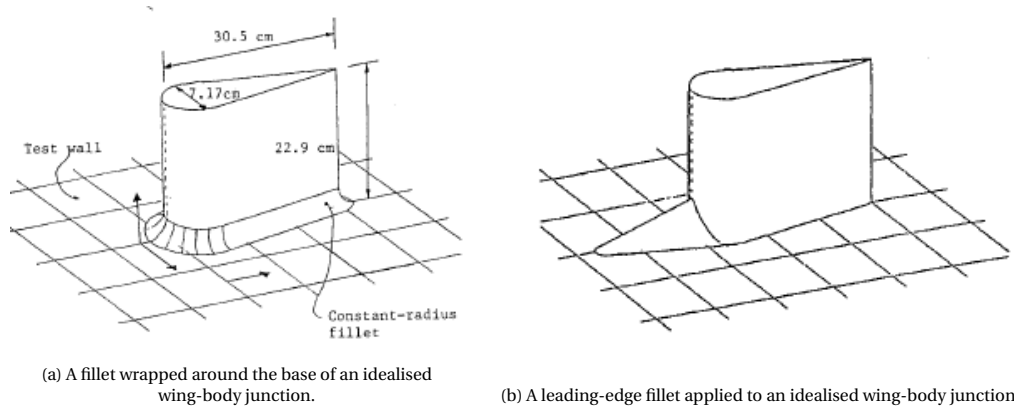
Figure 2.7: Possible fairings/fillets applied to an idealised wing-body junction.

Similarly to Devenport et al. [1992b], Kubendran et al. studied the effect of leading-edge fillets on a laminar junction flow. For a laminar junction flow, the pressure gradient in front of the wing-body junction is larger with respect to the turbulent case. Without a fillet, this results in the formation of a horseshoe vortex. Kubendran et al. found that by using a leading-edge fillet, the formation of the horseshoe vortex could be eliminated, by alleviating the steep adverse pressure gradient in front of the junction. Furthermore, the extent of the laminar flow region could be increased by the fillet, potentially resulting in a net drag reduction with respect to the original wing-body junction. Also, Kubendran et al. noted that in order for leading-edge fillets to work, the geometry of the fillets should be optimised for a pressure drag reduction and minimising the friction drag penalty such that the fillet generates a net drag reduction. Two leading-edge fillets were tested, a fillet of one inch and a fillet of two inches. For the fillet of two inches, a net reduction in drag was found, while for the 1 inch fillet, the pressure drag reduction was found to be too small to account for the friction penalty due to the increased wetted area.

Bernstein and Hamid [1996] investigated the effect of an asymmetric curved leading-edge strake-like fillet on a swept (20°) wing-body junction. Due to the strake, the horseshoe vortex was less well defined and turbulence intensities were reduced in the vicinity of the junction at both a zero and nine degree angle of attack. However, the turbulence was spread over a larger part of the viscous region. However, it is unclear whether drag reduction in the junction region was achieved.

Huang et al. [2015] installed a tetrahedron in the corner of a cylinder-body junction in order to control the horseshoe vortices which are formed upstream of the junction. They analysed the junction flow by means of laser-assisted particle flow visualisation and particle image velocimetry in a water towing tank. The cylinder-body junction can induce a single vortex, dual vortex or triple vortex. They found that when a tetrahedron is installed upstream of the cylinder, a vortical flow mode, reverse flow mode or forward flow mode occurs depending on the geometrical parameters of the tetrahedron and the flow Reynolds number. The geometrical parameters are the normalised axial length, expansion angle and tilt angle, which are defined in Figure 2.8. The boundary layer upstream of the junction does not separate when the forward flow mode appears, which happens at large normalised axial lengths.

Cho and Kim [2009a] employed a chamfered leading-edge in order to negate secondary flow losses. They varied the depth and height of the chamfer to study the effect on the strength of the horseshoe vortex. They found that with a chamfered leading-edge, the total pressure loss can be reduced by 1.55%. Another study of Cho and Kim [2009b] investigated the effect of leading-edge fences on a wing-body junction to reduce the strength of the horseshoe vortex. They studied the effect of the installed fence height and the length of the fence and found that with a leading-edge fence a reduction of 4.0% of the total pressure loss could be achieved.

Green and Whitesides [2003] present a method for designing leading-edge fillets which eliminate flow separation in the junction. In this method, the skin-friction distribution upstream of the leading-edge of

(a) Top view of the tetrahedron in the study of Huang et al. [2015]

(b) Side view of the tetrahedron in the study of Huang et al. [2015]
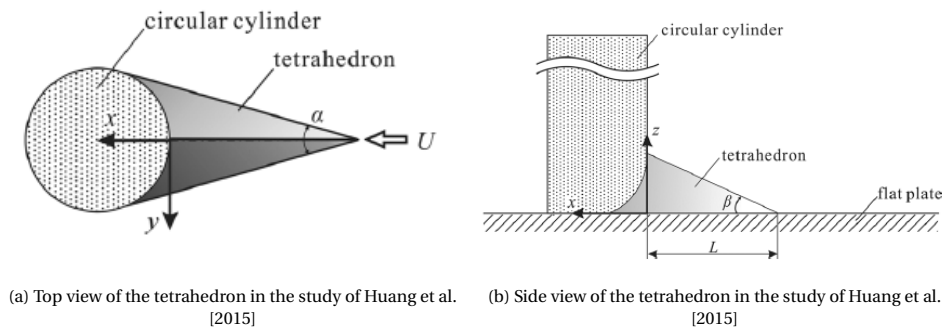
Figure 2.8: Geometric parameters to define the tetrahedron in the study of Huang et al. [2015]

the junction is determined, after which a target skin-friction distribution is specified which should eliminate flow separation. This results in a desired change in skin-friction, which by means of a design rule can be related to a change of the slope of the surface upstream of the junction. These slopes determine the shape of the new leading-edge fillet. By means of an iterative process the target skin-friction distribution can be achieved. Theys show that for two different wing-body junctions, flow separation was eliminated by means of this method. Furthermore, they argue that the design philosophy is more generally applicable to eliminate separation due to the fact that the method is based on a skin-friction/slope relationship instead of methods based primarily on trial- and-error approaches.

An alternative method to design leading-edge fairings is proposed by Van Oudheusden et al. [2004], which is based on an attachment-line approach. The method aims to eliminate separation at the leading-edge of the wing-body junction while maintaining a laminar wing. The method employs a panel-method to do an inviscid calculation of the flow around the fairing, which is followed by determining the boundary layer development on the attachment line along the body and fairing. Windtunnel testing showed that the method eliminates separation. However, further research has to be conducted whether the fairing performs as desired in off-design conditions (different angles of attack) or if drag reduction is achieved.

2.3.2. Boundary Layer Suction and Blowing

Next to the passive flow control techniques presented above to reduce the secondary flow losses, another common method to reduce these losses is the use of active flow control techniques such as boundary layer suction and boundary layer blowing. Philips et al. [1992] was the first to implement boundary layer suction to prevent the formation of the horseshoe vortex. The idea is to remove the boundary layer upstream of the wing-body junction by means of suction with the result that this eliminates the spanwise vorticity which causes the formation of the horseshoe vortex. The experiments of Philips et al. show that upstream boundary layer suction can reduce the size and strength of the horseshoe vortex. At a volumetric flow rate of 1.9 times the volumetric flow rate through the upstream boundary layer, boundary layer suction was able to almost completely eliminate the horseshoe vortex. However, streamwise vorticity was generated by means of the streamwise edges of the rectangular suction hole upstream of the wing-body junction and therefore, circulation could not be reduced to zero. They note that even though the boundary layer suction eliminates the large scale horseshoe vortex, a small horseshoe vortex might still exist due to the no-slip condition which requires the existence of a (small) boundary layer after the suction hole. However, it is expected that this small vortex has little to no effect on the flow field.

Johnson et al. investigated the effect of boundary layer suction and blowing on the wing-fuselage junction. In contrast to the study of Philips et al. [1992], a circular hole with a diameter of 20mm located 20mm upstream of the leading-edge of the junction was used. Also in the experiments of Johnson et al., the formation of the horseshoe vortex was attenuated due to boundary layer suction. Only a very weak vortex was formed due to the no-slip condition. At larger angles of attack, a vortex was observed at the pressure side of the wing and boundary layer suction proved to be a less effective solution. This can be explained due to size and geometry of the suction hole which is not wide enough to successfully remove the upstream boundary layer at larger angles of attack. Furthermore, it was found that boundary layer blowing attenuates the formation of the horseshoe vortex as well. However, larger vortical structures than the horseshoe vortex were created at by the flow plume at higher volumetric flow rates of boundary layer blowing.

Barberis et al. [1998] investigated the control of the formation of the horseshoe vortex by comparing a fillet upstream of the junction and boundary layer suction at two locations upstream of the junction. The fillet in the test did not show any noticeable decrease in the vortex structure, however, reduced levels of turbulent kinetic energy were observed in the separated region close to the wall. Boundary layer suction proved to be a very effective method to reduce the size of the vortex and moving the separation line closer towards the leading-edge of the junction. Furthermore, a dependency on the location of the suction slot was observed. The suction hole which was closer to the leading-edge of the junction was more efficient in reducing the size of the separated region.

Liu and Song [2017] used a novel technique to prevent the formation of the horseshoe vortex by determining the location where the mean streamlines are about to roll up in the turbulent wing-body junction. At this location, suction is applied at 1.2% of the flow rate of the upstream turbulent boundary layer. In the time-averaged flow field, neither a junction vortex nor a bi-modal probability density function of the fluctuating velocities is observed. Furthermore, in the instantaneous flow fields only a weak vortex was observed with a reduction of 68% of the fluctuating pressure. As a result, the flow around the wing-body junction becomes steady with respect to the vortical flow which was present in the case without suction.

Seal and Smith [1999] analysed the effect of localised suction on the horseshoe vortex in a cylinder-flat plate junction flow by means of particle image velocimetry. A constant suction rate was applied which ranged between 0% and 68% of the freestream velocity. Data was sampled from the symmtry plane and three downstream and cross-stream planes. The authors made the following observations: the horseshoe vortex appeared to be bi-stable, with a preference of two locations, a primary location where the horseshoe vortex resides the most of the time and a secondary location closer to the wall where the vortex is for a more limited period of time. Furthermore, they observed that the localised suction weakens the instantaneous vortex-surface interactions. Which results into weakening of the time-averaged horseshoe vortex in the symmetry plane. Also, it was observed that localised suction can weaken the downstream extension of the horseshoe vortex, however, with a larger downstream distance of the localised suction, the effect was less pronounced. Finally, it was observed that due to localised suction, the averaged-Reynolds stress levels were reduced in the symmetry and downstream planes. Therefore, Seal and Smith [1999] concluded that localised suction can be a viable approach to mitigate some of the negative effects of the horseshoe vortex.

2.3.3. Aerodynamic Shape Optimisation

Due to the increase in computational power and the development of efficient optimisation algorithms, the use of aerodynamic shape optimisation has become a powerful tool to investigate novel geometries to optimise the performance of wing-body junctions. Peigin and Epstein [2008] optimised wing-body junction for a generic business jet configuration by means of an optimisation algorithm which is based on a genetic algorithm. Inputs for the objective function of the optimisation are accurate full Navier-Stokes evaluations and these simulations are evaluated at realistic transonic flight cruise conditions. The optimisation achieved drag reductions in on- and off-design conditions.

Liu et al. [2017] optimised the wing-body junction by means of a hybrid FFD-RBF parameterisation approach. In this approach Free Form Deformation (FFD) Surface Parameterisation was employed to do aerodynamic shape design. The junction between the root of the wing and body has to be updated in the optimisation if the geometry of the root changes to preserve original connectivity between the wing and body. In order to preserve the original connectivity and handling the part update of the wing-body junction, a radial basis function (RBF) interpolation technique has been employed. As an optimisation algorithm, the novel Cuckoo Search algorithm has been employed while in order to reduce the high computational cost a Kriging surrogate model has been used with an expected improvement sampling criterion. Using the present system, Liu et al. [2017] optimised the DLR F4 wing-body model with the objective of drag reduction at constant lift with the constraint that the volume within the wing should not be reduced. A drag reduction of 4.63% was achieved while furthermore, the strength of the shock wave over the wing was alleviated.

Similarly to Liu et al. [2017], Sasaki et al. performed a design optimisation for a supersonic transport wing-body configuration with the goal to improve aerodynamic performance at Mach 2.0 and to reduce sonic boom at Mach 1.6. The optimisation was carried out by a mulitobjective genetic algorithm (MOGA), while evaluat-

ing the aerodynamic performance by means of Euler calculation. The geometry was defined by 131 design variables and based on these design variables, multiblock grids were generated. From the optimisation several Pareto solutions were found for the two different optimisation cases. It was observed that for all the Pareto solutions, the wing planform remained relatively constant, while the shape of the fuselage was different for the different Pareto solutions. They concluded from these results that in order to reduce both boom and drag, innovative/unconventional wing-body junctions are required.

Brezillon and Dwight [2011] employed an adjoint approach for the aerodynamic shape optimisation of a wing-body junction to eliminate flow separation. They demonstrated that the adjoint approach for aerodynamic shape optimisation can handle a large amount of design parameters by optimisation of the wing-body junction of the DLR-F6 configuration at Mach 0.75. Reynolds number of $3x10^6$ and a lift coefficient of 0.5. At this condition, the DLR-F6 has separated flow in the region between the upper part of the wing and the fuselage. The focus of the aerodynamic shape optimisation was to remove the separated flow while maintaining a constant lift coefficient of 0.5. The geometry was parameterised by the Free Form Deformation technique. They demonstrated that with a limited number of iterations, a reduction of 20 drag counts was achieved when optimising the shape of the fuselage while keeping the geometry of the wing constant. The resulting geometry was a double-dented fuselage.

Similarly to Brezillon and Dwight [2011], Xu et al. [2017] also optimised the DLR-F6 geometry to remove flow separation in the wing-body region. However, instead of employing a FFD-parameterisation technique, they employed a CAD-based parameterisation approach with more practical geometric and flow constraints. In this CAD-based optimisation the wing and fuselage of the junction are modelled by means of b-spline surfaces and the intersection line of these surfaces was determined with the in-house CAD-modeller. By means of this parameterisation method, Xu et al. [2017] found an optimised fuselage geometry with two distinctive bumps which suppressed the onset of flow separation in the wing-body junction and therefore show the potential of this CAD-based parameterisation method. A drag reduction of 12.4 drag counts was achieved.

Yi and Kim [2013] employed an adjoint-based design optimisation of vortex generators to control the horseshoe vortex in the wing-body junction of the DLR-F6 geometry without altering the geometry of the wing-body junction itself. To optimise the vortex generators, five design parameters were used: the chord length, the height, the angle of incidence, the streamwise-location of the vortex generator (x-location) and the spanwise location of the vortex generator along the wing (y-location). For a given set of flight conditions, the optimised vortex generators were able to increase the lift-to-drag ratio of the geometry of 4%, while also the strength of the junction vortex was decreased.

Song and Lv [2011] optimised a two-level wing-body junction fairing of a Civil Transport Aircraft by means of Kriging-based surrogate modelling. The geometry of the fairing was modelled by means a of b-spline representation. A drag reduction of 6.3 drag counts was achieved over a range of Mach numbers.

2.3.4. The Anti-fairing
Similar to the authors mentioned above, Belligoli et al. [2019] employed Aerodynamic Shape Optimisation to reduce the drag in wing-body junctions. For the shape optimisation they employed the capabilities of the software SU2, which can both solve the CFD simulations and the adjoint equations, which makes it very suitable for the aerodynamic shape optimisation. The geometry which was optimised is a semi-infinite NACA0015 wing mounted perpendicular to a flat plate at zero angle-of-attack. This geometry was chosen such that the result of the optimisation could be compared to the leading edge fairings as presented by Van Oudheusden et al. [2004]. A Free-Form Deformation method was employed in the optimisation algorithm. In contrast with the research presented above, Belligoli et al. [2019] decided to only optimise the flat-plate region of the junction while keeping the wing geometry constant to investigate the effect of the body on the drag. The FFD parameterisation was constraint such that the flat-plate was only allowed to deform in the spanwise-direction, inspired by the double-dented fuselage shape as presented by Brezillon and Dwight [2011]. The optimised form of the geometry is presented in Figure 2.9 and it is a concave and shallow dent around the geometry of the wing. The name of this novel wing-body junction comes from the fact that the geometry is the opposite of the typical wing-body junctions used in civil aircraft, hence, the name anti-fairing.

In order to keep the cost of the simulations in the optimisation low, Belligoli et al. [2019] used a fine enough mesh was used to capture the necessary flow features and bound the computational error. In order
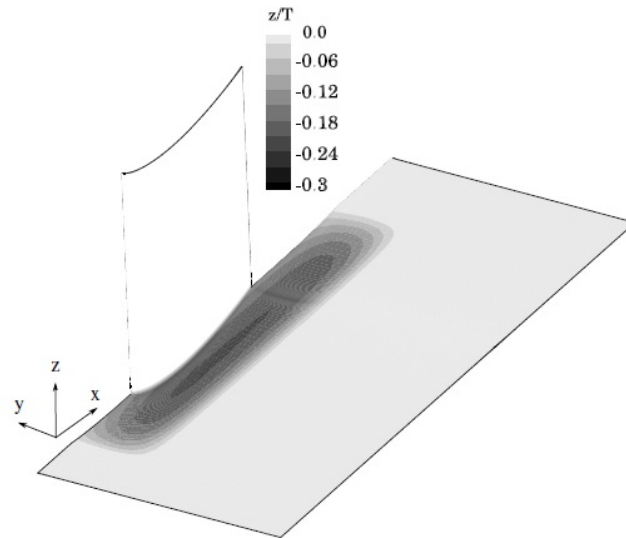
Figure 2.9: The anti-fairing geometry of Belligoli et al. [2019].

to validate the drag reduction of the optimised geometry, an experimental and numerical study of the anti-fairing was conducted. Additionally, a comparison between the anti-fairing and the short and long leading-edge fairings of Van Oudheusden et al. [2004] was made to gain insight in the effectiveness of the anti-fairing in comparison with more conventional fairings. The experimental study was carried out in the Low Turbulence Tunnel (LTT) of the Delft University of Technology by means of stereoscopic particle image velocimetry (SPIV). Next to the experimental study, a more refined numerical study was conducted. RANS simulations were performed with a hybrid structured & unstructured mesh. Structured, polyhedral cells were used in the boundary layer region with the cells closest to the wall satisfying y^+<1, while the unstructured cells were used in the rest of the domain. A mesh count of 11.5 millions cells were used in a steady, fully turbulent RANS simulation with the Spalart-Allmaras turbulence model. The mean normalised streamwise velocity contours downstream of the wing of the experimental study are presented in Figure 2.10..

a) Comparison of baseline (left) and antifairing (right) effect on the wake

b) Comparison of large-fairing (left) and small-fairing (right) effects on the wake
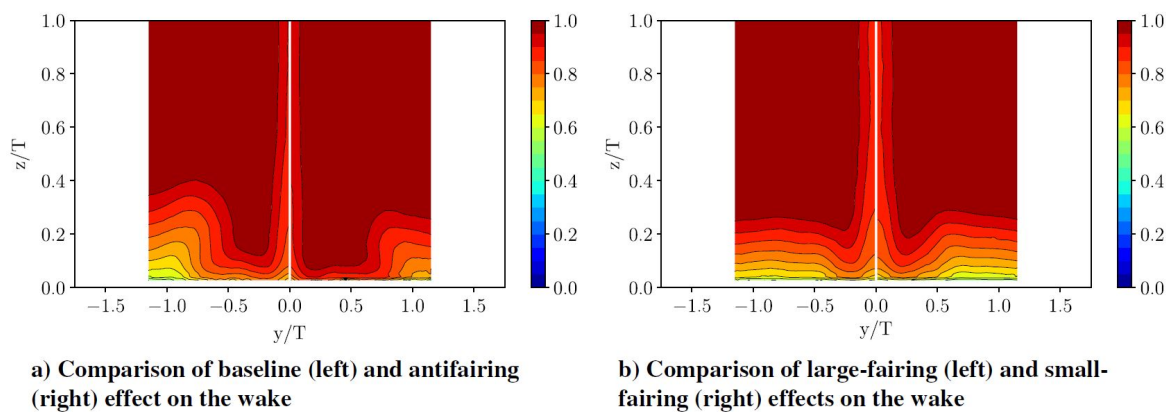
Figure 2.10: Mean normalised streamwise velocity contours in a plane X/T=5.33, downstream of the trailing edge of the wing, of the baseline (BS), Anti-fairing (AF), short-fairing (SF) and the long-fairing (LF) of the experimental study of Belligoli et al. [2019].

In Figure 2.10, the lumps of velocity deficit between y/T=+-0.5 and y/T=+-1.0 characterise the legs of the horseshoe vortex. From the experimental results, it can be observed that the leg of the horseshoe vortex of the anti-fairing has a larger distance from the vertical symmetry plane. This can be related to the Momentum Deficit Factor (MDF), for which a higher MDF results in a larger distance between the vortex legs. As both the baseline geometry and the anti-fairing geometry have the same thickness of the wing, it can be concluded that based on the relation in Equation 2.1, the momentum thickness of the boundary layer upstream of the

wing-body junction is higher for the anti-fairing case than the baseline case. Furthermore, it can be observed that the warping of the velocity deficit is large for both the baseline and anti-fairing case, indicating a strong horseshoe vortex. It should be noted that from these results, it can be concluded that the horseshoe vortex for the anti-fairing is slightly less strong than the baseline case. However, when comparing the results from Figure 2.10a with the results of the conventional fairings in Figure 2.10b, it can be observed that the extend of the horseshoe vortex is almost not detectable. This is in accordance with the working mechanisms of leading-edge fairings, which are designed to alleviate the adverse-pressure gradient which causes the formation of the horseshoe vortex, therefore reducing the drag. Hence, the drag reduction mechanism of the anti-fairing does not reduce the strength of the horseshoe vortex but instead seems to prevents momentum loss in the junction.

To get a better understanding of the drag reduction mechanisms of the anti-fairing, Belligoli et al. [2019] presented Figure 2.11a and Figure 2.11b, which show the comparison of the viscous and pressure drag components for the baseline and anti-fairing case and the evolution of the pressure coefficient in the symmetry plane over the anti-fairing are plotted, respectively. From Figure 2.11a, it can be concluded that the anti-fairing only had a small effect on the viscous drag while a large differences are observed in the pressure drag. These difference are observed in the beginning and end of the anti-fairing, where the highest curvatures of the anti-fairing are observed. Upstream of the wing, a net reduction of the pressure drag component is observed which is larger than the increase in drag at the rear of the anti-fairing. This results in a net-reduction of the drag of the anti-fairing. These drag forces at the rear and front of the anti-fairing are caused by the high pressure regions in the front and rear of the anti-fairing as observed from Figure 2.11b. The normal to the surface is inclined at an angle due to the concave shape of the anti-fairing as show in Figure 2.11b. This results in a force in the front of the anti-fairing which opposes the drag force and a force in line with the drag force at the rear of the anti-fairing. Due to the action of viscous forces, the pressure recovery is incomplete, resulting in a net-reduction of the drag. The anti-fairing geometry achieved a reduction of 5.96 drag count in CFD, while the conventional leading-edge fairings of Van Oudheusden et al. [2004] achieved a drag reduction of 0.20 and 0.12 drag counts for the long-fairing and short-fairing, respectively. From the experimental results, a drag reduction of 7.75 drag counts was observed for the anti-fairing.

(a) Comparison of the viscous drag and pressure drag components of the baseline geometry and the anti-fairing geometry. Source: Belligoli et al. [2019]

(b) Pressure coefficient at z/T=0 and the contour of the anti-fairing geometry at y/t=0.9. The dashed vertical lines indicate the regions of high curvature. Source: Belligoli et al. [2019]
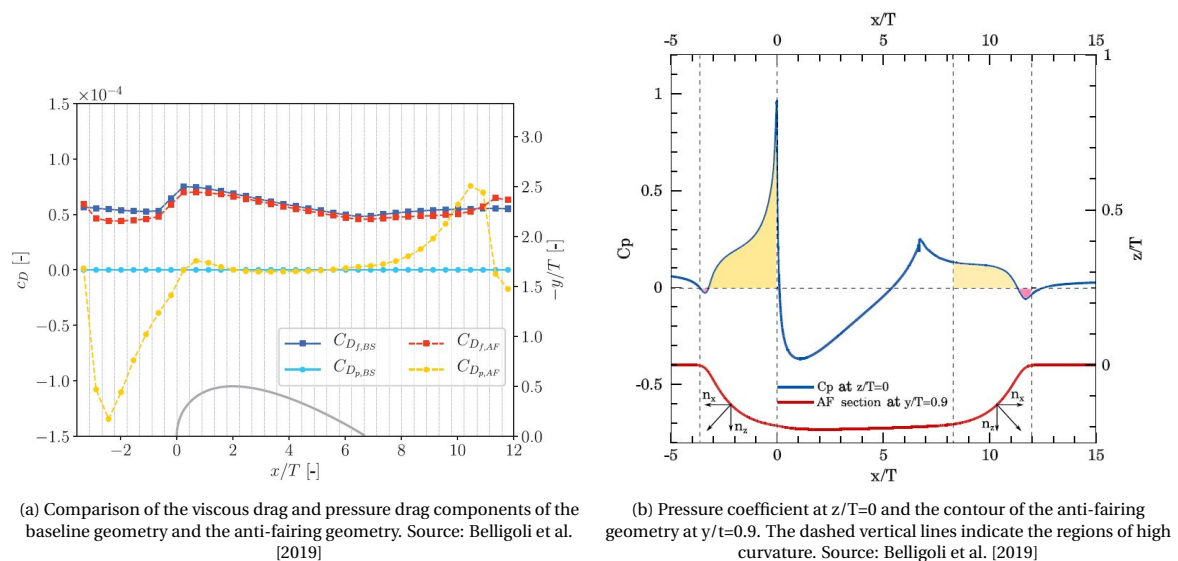
Figure 2.11: Comparison of the viscous drag and pressure drag components of the anti-fairing and the evolution of the pressure coefficient in the symmetry plane over the anti-fairing. Source: Belligoli et al. [2019]

From the study of Belligoli et al. [2019], it can be seen that the anti-fairing has potentially better drag-reducing capabilities with respect to conventional methods. Another advantageous aspect of the anti-fairing is that it is a passive flow control device and therefore does not require any active flow control mechanisms to be integrated in the wing. However, Belligoli et al. [2019] reported a difference between the drag reduction observed from the experimental study and the RANS simulations. This might be explained due to the limitations of RANS simulations, which can not capture all the complex flow physics present in junction flows. Therefore, Belligoli et al. [2019] recommended to perform a large-eddy simulation in order to get a bit understanding on

the effects of the turbulent quantities on the performance of the anti-fairing.

Srikumar [2019] conducted a follow-up on the study of Belligoli et al. [2019]. In their research, Srikumar [2019] performed a wall-modelled large-eddy simulation to investigate the effect of the anti-fairing on the turbulent quantities in the junction region and their effect on the shape and size of the horseshoe vortex. For the LES simulation, the in-house solver INCA was used, which is an implicit solver. This means that the truncation error in the discretisation of the convective terms are used as the subgrid-scale model. More specifically, the Adaptive Local Deconvolution Method was used as proposed by Hickel et al. [2006] as a discretisation scheme. Two LES-simulation were performed, a baseline simulation which was similar to the case of Ryu et al. [2016] and a simulation with the anti-fairing. For validation, the baseline case was compared to literature. The boundary layer profile upstream of the wing, the mean surface pressure coefficient, the mean spanwise vorticity in the symmetry plane and the turbulent kinetic energy in the symmetry plane were compared. The results of the wall-modelled LES were validated satisfactory, beside the magnitude of the turbulent kinetic energy in the horseshoe vortex, which was under predicted by the simulation as can be seen from Figure 2.12.
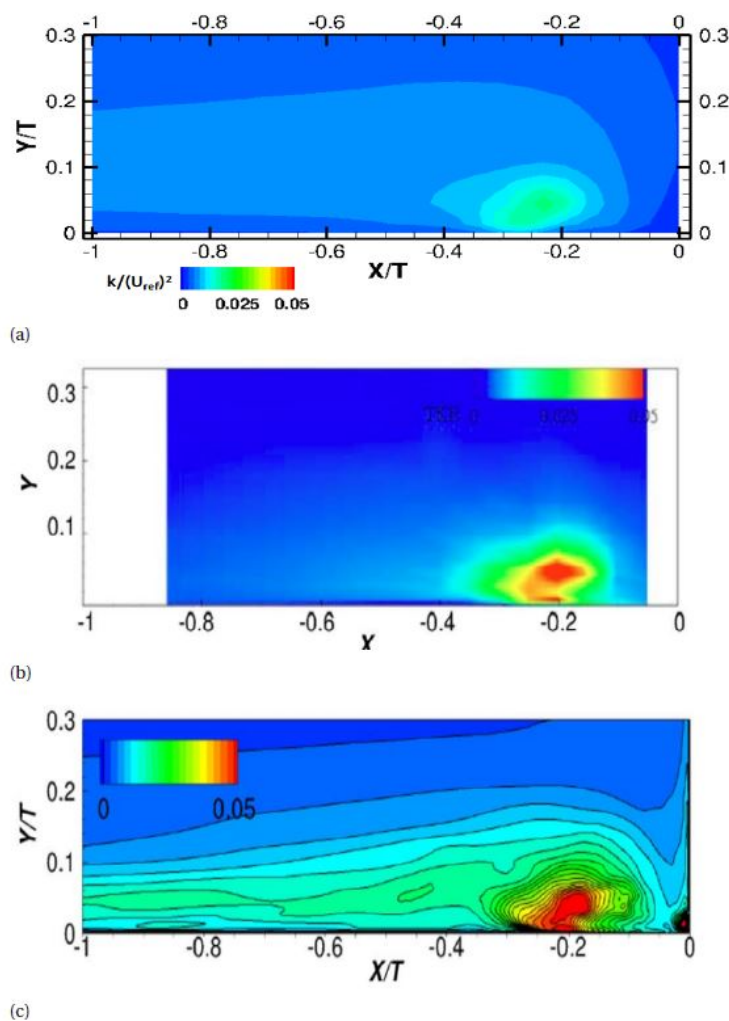
Figure 2.12: Turbulent kinetic energy in the symmetry plane upstream of the wing-body junction. a) Results of Srikumar [2019] b) Experimental Results of Devenport and Simpson [1990] c) Results of wall-resolved LES of Ryu et al. [2016]

From the validated simulations, the effects of the anti-fairing on the wing-body junction were studied. Srikumar [2019] found that the anti-fairing significantly reduced the size and magnitude of the horseshoe-vortex. A reduction of 40% of the peak turbulent kinetic energy was observed. Furthermore, the centre of the horseshoe vortex was located farther upstream and closer to the wall in the anti-fairing case. This can be explained due to the convex curvature of the anti-fairing upstream of the junction which results in an

increased momentum thickness and a reduction in turbulent kinetic energy. The observations are in line with the observations of Fleming et al. [1993] for higher values of the MDF. Similarly, it was observed that the horseshoe vortex moved away from the wing in the spanwise direction, which is another indication that the anti-fairing increases the MDF.

Furthermore, Srikumar [2019] observed corner separation in both cases, originating from a corner vortex. The corner separation was attributed to the wall-modelling used in the large eddy simulation. An increase in turbulent quantities was observed as the horseshoe vortex traversed the wing. This is attributed to the concave dent in the spanwise direction, which resulted in an increase in the Reynolds shear stress and mean turbulent kinetic energy as the HSV traversed the concave dent. Furthermmore, Srikumar [2019] computed drag coefficients were determined by means of the momentum deficit analysis for varying wing spans up to y/T=0.3. This height was chosen as for heights larger than y/T=0.4, spurious and nonphysical vertical velocities were observed in the wake of the wing. Within this height, Srikumar [2019] found a drag reduction of 1.8% of which the propulsive effect of the anti-fairing was the dominant effect which caused the drag reduction. However, further analysis showed that also a net reduction in skin-friction was observed due to an increase in momentum thickness in upstream boundary layer and due to dampening of the turbulence upstream of the wing.

Next to the wall-modelled LES studies, Srikumar [2019] studied the effect of varying the anti-fairing it's depth and the effect of varying the thickness of the upstream boundary layer in a set of RANS-simulations. A point of minimum drag was found of the total system of an anti-fairing depth of AF_{depth}/T=0.208. Furthermore, they observed that for a thicker boundary layer both the pressure drag and viscous drag decreased of the combined system, resulting in a decrease in the overall drag.

From the literature above, several categories of drag reduction approaches have been suggested. Leading edge devices such as fairings and fillets are common passive devices which are used as a tool to reduce the strength or completely eliminate the horseshoe vortex, reduce the associated turbulent stresses and therefore reduce the associated interference drag. Furthermore, active flow control devices show great potential in reducing the interference drag, however, a drawback is that it can be a complicated system to integrate in the wing-body junction. Furthermore, the location and design of both these passive and active flow control devices is an important factor to allow for the best flow control around these wing-body junctions. For instance, as reported by Kubendran et al., it is possible for these passive devices that the net-increase in skin friction outweighs the reduction in interference drag, which could potentially cause an increase in the total drag of the system. In order to account and optimise for the placement and design of these devices or the wing-body junction itself, aerodynamic shape optimisation can be a solution. One of the most promising novel aerodynamic geometries is the anti-fairing, which has from preliminary analysis better drag reducing capabilities with respect to other discussed methods and is a passive device. Furthermore, the wall-modelled LES of Srikumar [2019], showed that indeed a drag reduction is achieved by the anti-fairing by also capturing the effect of the turbulent quantities. However, due to the fact that a wall-modelled approach was used, the turbulent kinetic energy in the centre of the horseshoe vortex was under-predicted. Furthermore, Srikumar [2019] observed spurious and non-physical velocities above y/T=0.4, which affected the drag reducing analysis over the entire span of the wing. Due to the fact that the wall-modelled LES approach was not able to completely capture the complex flow mechanisms at play in a junction flow, together with the lack of an existing database of high-fidelity junction-flow data which could be used for a data-driven turbulence modelling approach, forms the motivation to conduct a wall-resolved large eddy simulation of a wing-body junction.

2.4. Data-Driven Turbulence Modelling

Turbulence is an important characteristic of fluid flows which has an influence on the performance of a vast amount of engineering applications. Due to the influence of turbulence on the performance of these engineering devices, it is important to have knowledge of turbulence in a flow and being able to determine its effect on an engineering application. Therefore, continuous research is conducted to develop techniques which allow to simulate and predict turbulent flows.

To represent the large range of temporal and spatial scales of turbulent motions and its chaotic nature is challenging. However, in order to represent these turbulent motions, many different theoretical and numerical approaches have been developed. With the increase of computational power, Direct Numerical Simulation (DNS) of a number of turbulent flows and processes have been completely resolved which shed light on the physics of these turbulent processes. However, due to the large computational cost, this method is

not suitable for most engineering applications. Therefore, several models exist which provide engineering approximations to directly solving the Navier-Stokes equations, such as the RANS and LES methods. The RANS methods are derived by an averaging procedure applied towards the Navier-Stokes equations and require closure methods to represent the turbulent stresses which derive from the averaging procedure. Due to the averaging procedure, the RANS-method are based entirely on models to approximate the turbulent scales of motion and is therefore significantly cheaper than a DNS procedure. The Reynolds-averaging procedure of RANS methods will be explained in detail in Chapter 4.2. In a Large Eddy Simulation, the large turbulent scales of motion are directly resolved by the solver while only the effect of the unresolved scales on the large scales is modelled.

Many turbulence models rely on the Boussinesq Hypothesis (also called turbulent-viscosity-hypothesis). In the Boussinesq hypothesis, the intrinsic assumption is made that the Reynolds stress anisotropy tensor is determined by the mean velocity gradients and the specific assumption is made that there is an alignment between the Reynolds stress anisotropy tensor and the mean rate-of-strain tensor S_{ij}, hence, the following equation for the Reynolds stress anisotropy tensor should hold:

$$a_{ij} = \overline{u'_i u'_j} - \frac{2}{3} k \delta_{ij} \approx -2\nu_t S_{ij}. \tag{2.4}$$

In the equation above, u'_i is the i'th component of the velocity fluctuations field, k is the turbulent kinetic energy, ν_t is the eddy viscosity and S_{ij} is the mean strain rate tensor and is defined as $\frac{1}{2}(\frac{\partial U_i}{\partial x_j} + \frac{\partial U_j}{\partial x_i})$. Many models rely on the Boussinesq Hypothesis due to the fact that it gives acceptable results in simple shear flows (Pope [2000]) as these flows follow the specific assumption, but also, due to the fact that the eddy viscosity adds numerical convergence to the model. However, in many flows, the Boussinesq hypothesis is not valid in regions of the flow. Pope [2000] gives examples of flows of which the velocity gradient tensor is more complex than in a simple shear flow, in which the Boussinesq hypothesis is known to fail. Some examples of these flows are swirling flows and flows with streamline curvature.

Alternatively, closures to the RANS-equations have been developed that try to remedy the deficiencies of the Boussinesq hypothesis. Reynolds Stress Transport Models (RSTM) solve an extra transport equation for every component of the Reynolds stress, resulting in six additional equations to be solved. These models do not rely on the Boussinesq hypothesis and are therefore better in predicting Reynolds stress anisotropy, however, are more costly due to more equations have to be solved.

Due to the assumptions made in deriving the RANS equations and the introduction of closure models for the RANS-equations introduce inaccuracies and potentially limit the predictive power of the method. Experimental results are typically used to calibrate the closure models of the RANS-equations However, with the increase in the availability of high-fidelity data sets and computational power, recent research has been focused on informing RANS turbulence models with data by means of machine learning and statistical inference to enhance and improve the performance of these models. Duraisamy et al. [2019];

In order to formulate a RANS closure model, a set of assumptions and simplifications is made to arrive at the closure model from the Navier-Stokes equations. These assumptions and simplifications can introduce errors. During the derivation of a RANS-closure, Duraisamy et al. [2019] suggests that errors can be introduced at four different levels of the derivation. The first level (L1) is due to the application of the time-averaging in the derivation of the Reynolds-Averaged Navier-Stokes equations in combination with the non-linearity of the Navier-Stokes equation, which results in the an undetermined system of equations. Hence, the need of closure models to close the system of equations. In other words, there are infinitely many instantaneous flow fields in time that result in the same time-averaged flow field. All these instantaneous flow-fields evolve differently in time and thus introduce uncertainties. Due to the averaging process in the derivation of the RANS-equations, the L1-level of uncertainty and is unavoidable.

The Level-2 uncertainty is related to the operational and functional representation of the Reynolds stress. To develop closure-models, a model-representation has to be made which relates the time-averaged fields to the instantaneous flow fields to remove the uncertainties introduced by the Reynolds-decomposition. For an incompressible flow, the unclosed term is the Reynolds stress tensor. An exact expansion of the Reynolds stress can be derived by means of the Cayley-Hamilton theorem and was first done by Pope [1975]. Typical assumptions made at the L2-level are Linear Eddy viscosity models (LEVM) and Reynolds-Stress models (RSM).

The Level-3 uncertainty is due to the uncertainty in the functional form within a model. Typically, algebraic or differential equations are used to represent the physical processes that the model tries to model. A large variety of choices for independent variables exist, however, the one- and two-equation models are the
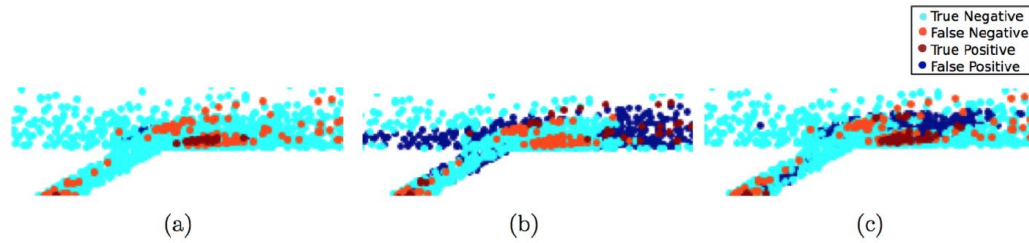
Figure 2.13: Classifier predictions of the validity of the linearity assumption of the Boussinesq hypothesis for a) Support Vector Machine Classifier, b) Adaboost Decision Tree Classifier and c) Random Forest Classifier in an inclined jet in crossflow case. Source: Ling and Templeton [2015]

most popular. Additional source terms might be added to these models to account for known sensitivities of these models, such a source term to correct for the near-wall dynamics of the flow. Hence, assumptions of the functional form of a turbulence model introduce uncertainties at the L3-level.

Finally, the Level-4 uncertainty is due to the uncertainty in the calibration of model coefficients within a model. Given a complete functional form of a model, the model coefficients should be tuned accordingly such that the contribution of the various effects the model tries to model with the closure are represented properly.

To identify regions of uncertainty in RANS-simulations, several authors have developed different techniques. Gorlé et al. [2014] introduced an analytical marker function which is designated to indicate in which regions of general flow fields the results of linear-eddy viscosity models are possibly not accurate. They note that the specific assumption of the Boussinesq Hypothesis notes holds only for parallel shear flows and therefore, the hypothesis breaks down in complex three-dimensional flows. The marker functions is designed such that it identifies regions which deviate from parallel shear flows.

Ling and Templeton [2015] explored the potential of using machine learning methodologies to explore the accuracy of RANS-solutions in a fluid flow domain by means of classification algorithms. The three machine learning algorithms that Ling and Templeton [2015] employed were the Support Vector Machine (SVM), Adaboost Decision tree and random forests. The machine learning algorithms were trained on a database of canonical flows for which validated DNS or LES data was available. The models were used to classify the uncertainty of the RANS-simulation on a cell-by-cell basis on several of the assumptions made in the RANS-approach. These assumptions were the non-negativity of the eddy-viscosity, the linearity of the Boussinesq hypothesis and the isotropy of the eddy viscosity. Ling and Templeton [2015] found that the models trained on the DNS/LES data could generalise and give acceptable results for flows different than those they were trained on. Furthermore, they found that the random forests had the best performance of the three algorithms in combination with its easy implementation due to the fact that it had the lowest class-averaged error. In comparison with the analytical marker of Gorlé et al. [2014], the random-forest approach shows a substantial improvement. In Figure 2.13, one can see the performance of the three different classification algorithms of an inclined jet in cross-flow case, which tests the (non-)linearity of the Boussinesq hypothesis. In the figure, the true positive and false negative points indicate where the RANS-assumption is violated, while the true negative and false positive points indicate the region where the RANS-assumption was valid.

Even though the results of the studies above indicate the location of the failure of turbulence models and give a better understanding of this phenomenon, the results of these studies are difficult to use to improve the predictions of turbulence models. However, as a result of the increase in the availability of high-fidelity data sets and computational power, recent research has been focused on informing RANS turbulence models with data by means of machine learning to enhance and improve the performance of these models.

Duraisamy et al. [2019] have given an overview of data-driven turbulence modelling and concluded that augmented turbulence models have the potential to lead to credible and useful models. The use of data-driven approaches is a recent development in turbulence modelling. Oliver and Moser [2011] and Cheung et al. [2011] were the first to assign posterior probability density functions to model parameters of turbulence models by using DNS data. Edeling et al. [2014] used a similar statistical inference approach to infer model coefficients.

Wang and Dow [2011] used full-field DNS velocity data to solve an inverse-RANS problem. They used the velocity field data from DNS to find the turbulent viscosity field that reproduces the flow field closest to

that of the DNS data. Similar full-field inversion approaches were used by Xiao et al. [2016] and Singh and Duraisamy [2016].

The methods presented above are not easily generalisable, therefore, it is desirable to use discrepancy function which can be used in flows with similar flow features. For instance, in order to reconstruct discrepancies in the anisotropy tensor, Tracey et al. [2013] used machine learning. Machine learning provides methods to generate a map between a quantity of interest and data. When applying these ML strategies, it is important to ensure objectivity and rotational invariance of the data-driven Reynolds stress models. Duraisamy et al. [2019]; Pope [1975] presented a general expansion of the Reynolds stress tensor. The work of Ling et al. [2016] used a neural network with embedded invariance to approximate the coefficients of the expression of Pope. Similarly, Weatheritt and Sandberg [2016] used symbolic regression and a genetic algorithm to infer the coefficients of the expression of Pope.

Instead of estimating the anisotropic part of Reynolds stress tensor itself, Schmelzer et al. [2019] determines the residual of the estimated Reynolds stress by the k-ω model by comparing with high-fidelity data. A machine learning approach based on an elastic net regularisation is used to promote sparsity within the generated models. This approach requires full-field data, hence the present study.

3

Research Aim, Research Objective and Research Questions

In this chapter, the research aim, research objective and research questions which are developed for the research project and based on the literature review will be discussed.

3.1. Research Aim & Research Objective

In the introduction, the goal/aim of this research project has already been briefly described as follows: "to generate a high-fidelity data set for a data-driven turbulence modelling approach to improve the accuracy of RANS simulations in junction flows". From this research aim and the available literature as presented in the literature review, the following research objective has been established:

> "*The objective of the research is to generate high-fidelity junction flow data, to be used in a data-driven turbulence modelling approach to improve the accuracy of RANS simulations in junction flows, by performing a wall-resolved Large Eddy Simulation of the wing-body junction originally studied experimentally by Devenport and Simpson [1990].*".

In order to achieve the research objective, three sub objectives have been developed. The first sub-objective is to validate whether the wall-resolved Large Eddy Simulation properly captures the complex flow mechanisms in the junction flow by comparing the data to experimental and numerical data.

The second sub-objective is to investigate the differences between the wall-resolved LES simulation and several other numerical methods. To do so a coarse-mesh RANS simulation will be performed to compare to the wall-resolved LES simulation. Furthermore, as the present research is based on a recommendation of the research of Srikumar [2019], a comparison to the wall-modelled LES of Srikumar [2019] will be made to identify whether the wall-resolved LES will be an improvement.

The final sub-objective will be to identify the areas of interest in junction flows in which data-driven turbulence models can provide a significant improvement with respect to conventional turbulence models by looking at the Boussinesq hypothesis validity in the domain, specifically in the symmetry plane upstream of the wing.

3.2. Research Question(s)

From the research objective, three sub-objectives have been derived to investigate during the thesis. From these three sub-objectives, several research questions and sub-questions have been derived. Answering the sub-questions should provide the answer to the main-research questions.

The first research question relates to the validation of the wall-resolved LES simulation. In order to be certain whether the data which will be used for data-driven turbulence modelling is accurately representing the junction flow, the data will be compared to experimental and numerical validation data. Answering the first research-question, should give confidence about the quality of the wall-resolved LES simulations.

The second and third research question relate to the second sub-objective and investigate how the results of a RANS simulation and the wall-modelled LES differ to those of the wall-resolved LES in the present study.

The final research question focuses on identifying of which areas in the computational domain are of specific interest for data-driven turbulence modelling of junction flows. This will be achieved by looking at the Boussinesq validity of the flow in the domain in the symmetry plane upstream of the wing.

1. Does the wall-resolved LES capture all the flow physics observed in (experimental and numerical) junction flow validation data correctly?

    (a) How do the observations of location, size and strength of the horseshoe vortex in the wall-resolved LES compare to the experimental validation data?

    (b) How do the boundary layer profiles in the symmetry plane of the domain, the pressure distribution and the mean flow streamlines at the bottom wall of the wall-resolved LES simulation compare to the experimental and numerical validation data?

    (c) Does the wall-resolved LES simulation capture the bimodal dynamics of the horseshoe vortex system?

    (d) How do the corner flow physics of the wall-resolved LES simulation compare to the observations of the numerical validation data of Ryu et al. [2016].

2. How does a RANS-simulation perform in comparison to the wall-resolved LES simulation in capturing the complex three-dimension junction flow?

    (a) How do the location and peak levels of the turbulent kinetic energy and spanwise vorticity at the core of the horseshoe vortex, estimated by the wall-resolved LES, compare to the RANS-simulation?

    (b) How do the near-wall boundary layer profiles compare of the RANS-simulation in comparison to the wall-resolved LES?

    (c) How does the pressure distribution and mean flow visualisation at the bottom wall of the RANS-simulation compare to that of the wall-resolved LES simulation?

3. Are the results of the wall-resolved LES an improvement with respect to the wall-modelled LES performed by Srikumar [2019]?

    (a) How does the location and strength of the turbulent kinetic energy peak at the core of the horseshoe vortex as predicted by the wall-resolved LES compare to the results of the wall-modelled LEs of Srikumar [2019]?

    (b) How does the location and strength of the spanwise vorticity peak at the core of the horseshoe vortex as predicted by the wall-resolved LES compare to the results of the wall-modelled LEs of Srikumar [2019]?

4. In which regions of the domain, specifically in the symmetry plane upstream of the wing, is the Boussinesq hypothesis not valid and could a data-driven turbulence modelling approach provide an improvement with respect to conventional turbulence models?

    (a) At which locations in the symmetry plane upstream of the wing does the flow not satisfy parallel shear flow?

    (b) At which locations in the symmetry plane upstream of the wing does the Reynolds stress tensor not align with the mean strain-rate tensor?

    (c) At which locations in the symmetry plane upstream of the wing does the ideal eddy viscosity become negative?

    (d) How does the Boussinesq TKE production compare to the true TKE production based on the Reynolds stress tensor?

4

Numerical Methodology: LES & RANS

In this Chapter, the methodology to perform the required simulations will be presented. From the research objective, the goal of this project is to generate a set of high-fidelity junction flow data, which will be used in a data-driven turbulence modelling approach to improve the accuracy of RANS simulations in junction flows. To acquire this high-fidelity junction flow data set, a wall-resolved Large Eddy Simulation (LES) will be performed of a flat plate & wing junction to capture the unsteady and turbulent nature of the flow in the junction. In order to check the validity of the simulation, the flow parameters used in the numerical study are similar to those in the experiments of Devenport and Simpson [1990]. To initialise the LES simulation, a RANS-simulation will be performed, while for the inflow condition of the LES simulation, a library of inflow data will be generated by means of a precursor simulation. The numerical methodology for these simulations is presented in this Chapter.

4.1. Numerical Methodology: Large Eddy Simulation

First the numerical methodology and theory behind a large eddy simulation will be presented. First the equations which govern the simulation will be discussed. This is followed by an in depth presentation of the boundary conditions required to set-up the Large Eddy Simulation. Finally, the geometry & computational domain, information about the solver, information about the mesh generation and information about the required computational resources will be presented.

4.1.1. Governing Equations

The motion of (viscous) fluids is described by the Navier-Stokes equations. The equations are non-linear partial differential equations and are therefore difficult to solve analytically. As a result, the Navier-Stokes equations are solved numerically by means of a Direct Numerical Simulation (DNS). In a DNS, all the scales of motion in the flow are completely resolved. Due to the significant differences in length scales present in turbulent flows, a fine resolution of the mesh is required such that the mesh resolves the Kolmogorov scales, which are the characteristic scales of the smallest turbulent motions, Pope [2000]. The Kolmogorov scale is a function of the dissipation rate ϵ and the kinematic viscosity ν and vary with the Reynolds number. When increasing the Reynolds number, the Kolmogorov length- and time-scales decrease, resulting that directly solving the Navier-Stokes equations numerically by means of a DNS simulation can become quickly too expensive for higher Reynolds number flows. The Navier-Stokes equations for an incompressible, Newtonian fluid are presented in differential form in (4.1) and (4.2), respectively. Here, (4.1) is the continuity equation (conservation of mass) and (4.2) is the momentum equation (conservation of momentum) in the three directions of a Cartesian coordinate system.

$$\frac{\partial u_i}{\partial x_i} = 0 \tag{4.1}$$

$$\frac{\partial u_i}{\partial t} + u_j \frac{\partial u_i}{\partial x_j} = -\frac{1}{\rho}\frac{\partial p}{\partial x_i} + \nu \frac{\partial^2 u_i}{\partial x_j \partial x_j} + f_i \tag{4.2}$$

In the equations above, u_i indicates the velocity components along the three axis of a Cartesian coordinate system, p indicates the pressure and f_i indicates the body forces.

In order to reduce the computational cost with respect to DNS, a Large Eddy Simulation can be performed, in which the large three-dimensional turbulent unsteady scales are resolved while the effect of the small scales on the large scales, which are very expensive to resolve, is modelled. In terms of computational expenses, the computational cost of an LES simulation is in between that of a RANS-simulation and a DNS-simulation. As noted earlier, the computational cost of DNS simulations is too high to be a feasible option for high Reynolds number flows. Furthermore, a large percentage of the computational resources are allocated to resolving the smallest dissipative motions, while the larger scales contains most of the energy and flow anisotropy.

In an LES simulation, a separation of scales is made between scales which are resolved by the simulation and unresolved scales. This scale separation originates from the idea of Richardson [1922], who identified the energy cascade. In the energy cascade, kinetic energy is produced at the largest scales of motion. The kinetic energy is transferred to the smaller scales of motion by inviscid processes. At the smallest scales of motion the energy is dissipated due to viscous effects. The scale separation is achieved by a filter operation, after which the large three-dimensional unsteady scales (which are not universal and are affected by the geometry) are resolved by the simulation, while the effect of the small scales (which have to some extend a universal character) on the large scales is modelled. By modelling the effect of the small scales of motion on the large scale of motion, the computational cost of resolving the small scales in a DNS is removed.

There are a few conceptual steps involved in a Large Eddy Simulation. First, a filtering operation is defined to decompose the velocity field $U(x,t)$ into the sum of the filtered (resolved) velocity field, $\overline{U}(x,t)$, and the subgrid-scale (unresolved) velocity field, $u''(x,t)$. The filtered velocity field is a time-dependant three-dimensional velocity field and represent the motion of the large eddies. A similar operation is done for the pressure field. Based on these filter operations, the filtered LES equations are derived from the Navier-Stokes equations and are:

$$\frac{\partial \overline{u}_i}{\partial x_i} = 0, \tag{4.3}$$

$$\frac{\partial \overline{u}_i}{\partial t} + \frac{\partial \overline{u}_i \overline{u}_j}{\partial x_j} + \frac{1}{\rho}\frac{\partial \overline{p}}{\partial x_i} - \nu \frac{\partial^2 \overline{u}_i}{\partial x_j \partial x_j} = -\frac{\partial \tau_{ij}}{\partial x_j}, \tag{4.4}$$

$$\tau_{ij} = \overline{u_i u_j} - \overline{u}_i \overline{u}_j. \tag{4.5}$$

In these equations, the only term which has to be modelled is the subgrid-scale (SGS) tensor τ_{ij} and can be modelled explicitly or implicitly. The SGS-tensor, τ_{ij}, in Equation 4.4 is defined in Equation 4.5. Then, the filtered LES-equations are solved for $\overline{U}(x,t)$, which provides an approximation of the large-scale motions. Explicit modelling of the SGS-tensor provide explicit approximations of the SGS-tensor in the filtered LES-equations to solve the closure problem. A few examples of such models are the original Smagorinsky (1963) model, which was later used in a dynamic approach of Germano et al. [1991], the Vreman model of Vreman [2003] and the Wall-Adaptive Local-Eddy Viscosity (WALE) model of Ducros et al. [1998]. Alternatively, one can model the SGS-tensor implicitly within the discretisation and design the truncation error of this discretisation method such that it behaves as the SGS-model. An example of such a discretisation scheme is the adaptive local deconvolution method (ALDM) proposed by Hickel et al. [2006]. The LES solver in the present study uses the explicit Wall-Adaptive Local-Eddy Viscosity (WALE) model.

4.1.2. Inflow Boundary Conditions

In order to fully determine the system and define a well-posed mathematical problem, it is required to set the boundary conditions for the LES simulation. LES and DNS simulations on non-periodic domains require an inflow boundary condition which represents the contribution of resolved, unsteady and three-dimensional eddies at the inlet. The inflow boundary condition has to accurately represent the flow upstream of the computational domain, because a lack of information of the large number of space-time modes in transitional- and turbulent flows introduces errors. Ideally, one would like to have one long domain and let the flow develop from laminar to turbulent flow, however, this is computationally expensive and therefore in reality not a feasible solution. Therefore, several inflow generation techniques exist to generate inflow conditions for turbulent flows. There are three types of methods to generate turbulent inflow conditions:

1. **Synthetic Turbulence:** The idea of this method is to generate a realistic turbulent inflow field based on known data at the inlet. This is done by generating artificial velocity fluctuations with the same

statistical moments as the desired inflow. An ideal synthetic turbulence generator introduces turbulent structures which are specific for the problem at hand. These synthetic structures should satisfy the mean velocity profile, Reynolds stress tensor, turbulent kinetic energy spectrum and have correct phase information.

2. **Recycling/Rescaling:** This method generates an inflow condition based on the information contained downstream in the simulation. This information is then recycled to the inlet plane. Due to the fact that the boundary layer is increasing in thickness over this distance, a rescaling method is required at the inlet before it can be used to generate a suitable inlet condition.

3. **Precursor Methods:** This method generates an inflow condition based on stored simulation data with the required instantaneous inflow data over the entire time history of the flow. This can be from an external source or can be generated concurrently as a precursor simulation.

An ideal synthetic turbulence inflow condition should satisfy to a set of flow conditions specific to the problem at hand as presented above. To satisfy these conditions for a specific flow case is also one of the most challenging tasks in generating synthetic turbulence at the inlet. For instance, according to Keating et al. [2004], it is crucial to satisfy the proper phase information as it determines the shape and sizes of the generated eddies. Current synthetic turbulence generators are far from ideal synthetic turbulence generators and therefore are not able to correctly generate true physical turbulence. Dhamankar et al. [2018]; Furthermore, due to the approximate nature of synthesised turbulence, a redevelopment region is required in the domain which is needed to develop real turbulence. This requires additional computational resources for the main simulation which are not required for precursor based techniques and recycling/rescaling techniques. Furthermore, it makes it difficult to impose exact flow properties to the boundary layer. Due to the lack of accurate turbulence data at the location of the inlet and the fact that current synthetic turbulence generators are far from ideal, this method has been rejected.

The second method to generate an inflow condition is the recycling/rescaling boundary condition as proposed by Lund et al. [1998]. In the implementation of Lund et al. [1998], the recycling/rescaling boundary condition recycles and rescales the flow at the recycling plane downstream of the inlet and reintroduces it at the inflow plane, until it achieves a desired momentum thickness at the inlet. Different similarity laws are used in the method of Lund et al. [1998] to rescale the mean and fluctuating velocity components in the inner and outer regions of the boundary layer, respectively. In contrast to Lund its implementation of the boundary condition with two concurrent simulations, it is instead desirable to use the boundary condition in an internal-mapped mode in an extension of the domain, upstream of the wing. The internal-mapped mode reduces the complexity of having two concurrent simulations. The location of the downstream recycling plane in the domain is at 10 inlet boundary layer thicknesses. A limitation of this recycling/rescaling method is that the rescaling laws are only applicable in an equilibrium region, which should be added upstream of the actual inlet of the simulation. Furthermore, the rescaling of the flow at the inlet plane leads to a distortion of the flow structures at the inlet plane due to a wall-normal compression. Finally, the recycling/rescaling boundary condition is not present by default in OpenFOAM which is used for the present study. Implementation of Lund et al. [1998] its recycling/rescaling boundary condition and to properly parallelise the boundary condition such that it can efficiently perform with many cores, increases the complexity of the simulation significantly. Therefore, using this method was rejected.

The most suitable option was found to be the precursor methods. Due to the fact that the precursor method is based on a library of existing turbulent data, the method eliminates a large source of errors present in previously discussed results. However, the drawback of such methods is that if no suitable external databases are found, it is required to run a precursor simulation to create a library of turbulent inflow data, which can be computationally very expensive. Nonetheless, due to the available computational resources, the accuracy and simplicity of the method, the precursor method was found to be the most desirable method to generate an accurate inflow condition for the present study.

The Precursor Simulation

In order to generate a library of accurate inflow data, the most commonly used method is the recycling/rescaling method as proposed by Lund et al. [1998] employed on a zero pressure-gradient (flat plate) turbulent boundary layer flow. In this method, the inflow condition for the main simulation will be sampled by extracting data from a plane within the precursor simulation, corresponding with the desired boundary
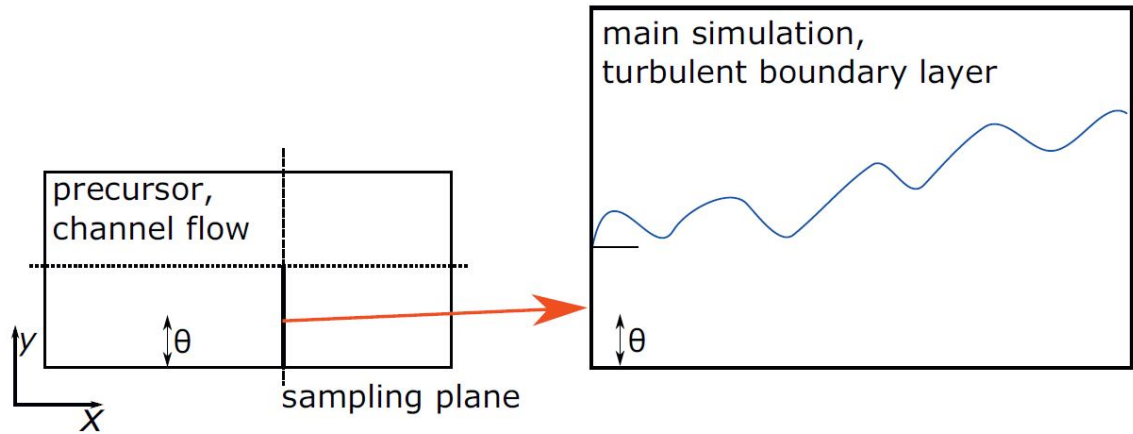
Figure 4.1: Schematic overview of the method proposed by Mukha and Liefvendahl [2017]. Data will be sampled at a plane in the TCF precursor simulation and is used as an inlet condition for the main simulation.

layer characteristics. As presented above, for the present study, the recycling/rescaling boundary condition is not a feasible method due to the fact that this method is not present by default within OpenFOAM. Instead, the method proposed by Mukha and Liefvendahl [2017] will be employed, which suggests to sample data from a fully developed turbulent channel flow (TCF), to use this data as an inlet condition for large eddy simulations. A schematic overview of this method is presented in Figure 4.1.

Using a turbulent channel flow as a precursor method has a few features which make it an attractive method. By using a turbulent channel flow, it eliminates the need for a recycling/rescaling approach and therefore, eliminates the wall-normal compression of the flow-structures at the inlet of the domain due to the rescaling. Furthermore, it reduces the the complexity of the precursor simulation. However, there is a difference between the structure of the boundary layer in a turbulent channel flow and the structure of a flat-plate turbulent boundary layer. It is generally known that the structure of wall-bounded turbulence in the inner part of the turbulent boundary is similar for all wall-bounded flows, given that there is an absence of a pressure-gradient. This was confirmed by Monty et al. [2009], which compared a pipe flow, a turbulent channel flow and a zero pressure-gradient turbulent boundary layer flow at a friction Reynolds number of approximately 3000. They found that within $y/\delta < 0.25$, the inner-scaled mean velocity profile is identical for all three cases. However, at heights beyond $y/\delta > 0.25$, there is a noticeable difference in the mean velocity profile between a flat plate turbulent boundary layer and a turbulent channel flow. This can be explained due to the flat that in a flat plate turbulent boundary layer simulation, there is an interaction with the outer part of the turbulent boundary layer and the freestream flow, while in a turbulent channel flow, different dynamics are at play and this interaction is not present.

It can be observed that both the recycling/rescaling method and the TCF precursor method will produce an inlet condition which deviates from an ideal zero-gradient turbulent boundary layer. Mukha and Liefvendahl [2017] found that the adaption length, which is the length required to generate a fully developed turbulent boundary layer with the desired properties, for the turbulent channel flow precursor method was on par with those of recycling/rescaling methods. Therefore, the turbulent channel flow precursor method was chosen to be used for the present study due to the fact it performs on par with recycling/rescaling methods and its conceptual simplicity.

The method proposed by Mukha and Liefvendahl [2017] is based on the main LES simulation where an inflow condition is required. For this method, the inflow is assumed to be a turbulent boundary layer at a wall, and a free-stream velocity U_∞ above the turbulent boundary layer, which is the case for the present study. The TCF precursor simulation will be designed such that it satisfies the desired conditions of the turbulent boundary layer at the inflow patch of the main simulation. The inflow patch of the main simulation should be rectangular and satisfy the following conditions:

$$0 < z < b_i$$

$$0 < y < h_i$$

In these conditions, b_i is the width of the inflow patch of the main simulation and h_i is the height of the inflow patch of the main simulation which is assumed to be significantly higher than the height of the boundary layer at the inlet patch. The boundary layer itself is specified by its momentum thickness, θ_i, and also the kinematic viscosity, ν_i, is specified. Hence, the following set of parameters are specified for the inlet patch of the main simulation:

$$b_i, h_i, U_\infty, \theta_i, \nu_i$$

From this set of parameters, a set of three independent non-dimensional parameters can be made. These parameters are the non-dimensional width of the inlet patch b_i/θ_i, the non-dimensional height of the inlet patch h_i/θ_i and the momentum thickness Reynolds number, Re_{θ_i}. Furthermore, a Cartesian axis system is assumed in which the x-axis is in the direction of the free-stream flow, the y-axis is the wall-normal direction and the z-axis is in the spanwise direction.

Given this set of parameters, it is the goal to design the turbulent channel flow precursor such that it satisfies the conditions at the inlet of the main simulation such that it can provide time-resolved simulation data. The size of the computational domain of the precursor simulation is defined as follows:

$$0 < x < l_p$$
$$0 < y < h_p = 2\delta$$
$$0 < z < b_p$$

Here, l_p is the length of the TCF, h_p is the height of the TCF, b_p is the width of the precursor and δ is the boundary layer thickness. The controller in OpenFOAM which drives the velocity flow through the turbulent channel flow is the *meanVelocityForce* controller. In this controller a desired bulk velocity, $\overline{U}$, is set. This bulk velocity is achieved by controlling a constant pressure gradient which drives the flow. The bulk velocity is defined in Equation 4.6, in which, $< u(y) >$, notates the time-averaged x-component of the velocity vector.

$$\overline{U} = \frac{1}{h_p} \int_0^{h_p} \langle u(y) \rangle \, dy \tag{4.6}$$

$$Re_{\theta_p} = \frac{U_c \theta_p}{\nu_p} \tag{4.7}$$

The centre-velocity, U_c, is defined as the velocity at the centre of the turbulent channel flow, hence, at a height of $0.5h_p$ or at a height of δ. This centre velocity is used to determine the momentum thickness Reynolds number of the turbulent channel flow, which is defined in Equation 4.7, which should match the momentum thickness Reynolds number of the inlet patch of the main simulation. Finally, a kinematic viscosity of the precursor, ν_p has to be defined. The following set of parameters, define the precursor simulation:

$$l_p, b_p, \delta, \overline{U}, U_c, \nu_p$$

The boundary conditions which are used in the precursor simulations are a no-slip wall at the bottom and top patch of the computational domain, while the side patches, the inlet patch and the outlet patch have cyclic boundary conditions.

Given the set of parameters of the main simulation, a four-step procedure will be given, based on the procedure presented by Mukha and Liefvendahl [2017], to determine the set of parameters of the precursor simulation with the main goal to match the momentum thickness of the turbulent channel flow to that of the inlet patch of the main simulation. The procedure is as follows:

1. The width of the precursor simulation will be set to be the same as the width in the main simulation, hence, the following condition will hold: $b_p = b_m$. This is done, such that when the data from the TCF is interpolated on the inlet patch of the main simulation, it will not stretch the flow structures of the TCF. Furthermore, the kinematic viscosity of the precursor simulation will be the same as in the main simulation, hence, $\nu_p = \nu_m$.

2. The length of the computational domain of the precursor will be defined as four times the height of the computational domain, hence, $l_p = 4h_p = 8\delta$. This length is considered to be sufficient to prevent coupling of the inflow and outlet patches of the precursor simulation.

3. The length scale which defines the precursor is the boundary layer thickness, δ, which is a given input from the main simulation. Using (4.13), a first order estimate is made of the momentum thickness. Given the boundary layer thickness, δ, the centre-velocity, U_c, which is set to be equal to the free-stream velocity of the main simulation, hence, $U_c = U_\infty$, and the kinematic viscosity, ν, one can solve (4.8) iteratively until a sufficiently converged updated momentum thickness is achieved.

$$\frac{\delta}{\theta} = f_2\left(Re_\theta\right) \tag{4.8}$$

$$f_2 \approx 11.28 + 2.603 \cdot 10^{-4} Re_\theta^{0.9834} \tag{4.9}$$

The function f_2 is a semi-empirical fit of Mukha and Liefvendahl [2017] to the DNS data of Lee and Moser [2015] and is presented in (4.9). Mukha and Liefvendahl [2017] noted that the error of (4.9) is within 2% of the DNS data and found that this approximation is sufficiently accurate for the current application. In Figure 4.2, one can find a plot of (4.9) and the DNS data of Lee and Moser [2015].
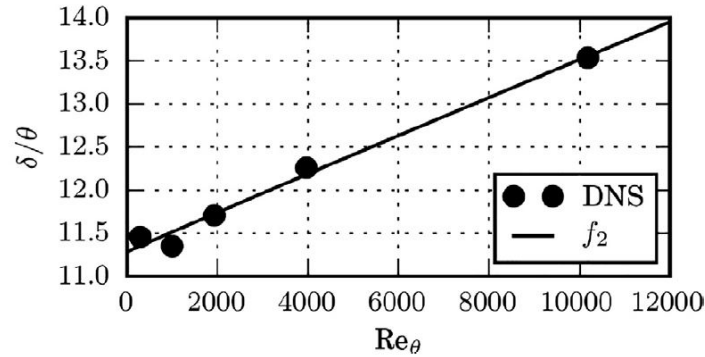
Figure 4.2: A plot of Equation 4.9 and corresponding DNS values of Lee and Moser [2015]. Illustration taken from Mukha and Liefvendahl [2017].

4. Finally, the bulk velocity which drives the turbulent channel flow will be determined by means of (4.10). In this equation, U_c is the centre-velocity of the turbulent channel flow and is set to be equal to the free-stream velocity of the main-simulation. The parameters f_1 is a function of the momentum thickness Reynolds number and is found by solving a semi-empirical fit of DNS data of Lee and Moser [2015], which is given in (4.11). The empirical fit of Mukha and Liefvendahl [2017] in (4.11) has an error of 0.3% with respect to the DNS-values and is therefore an acceptable fit.

$$\frac{U_c}{\overline{U}} = f_1\left(Re_\theta\right) \tag{4.10}$$

$$f_1 \approx 1.0 + 0.3427 Re_\theta^{0.1287} \tag{4.11}$$

The procedure above explains how to design the turbulent channel flow such that it satisfies the conditions at the inlet of the main simulation. Once the precursor simulation is running, data will be sampled for every time step at a yz-plane in the middle of the domain to eliminate the effect of the cyclic boundary conditions in the sampling space. Data over the entire span of the domain and up to half of the domain height is used, as this resembles the turbulent boundary layer at the inlet of the main-simulation. Hence, data is sampled at a location x=x_0 over the entire width of the precursor b_p and between values of $0 < y < \delta$. This data, is then given as an input at the inlet of the domain of the main simulation between $0 < y < \delta$. For the remainder of the height of the inlet patch, so between $\delta < y < h_m$, the constant free-stream velocity is specified.
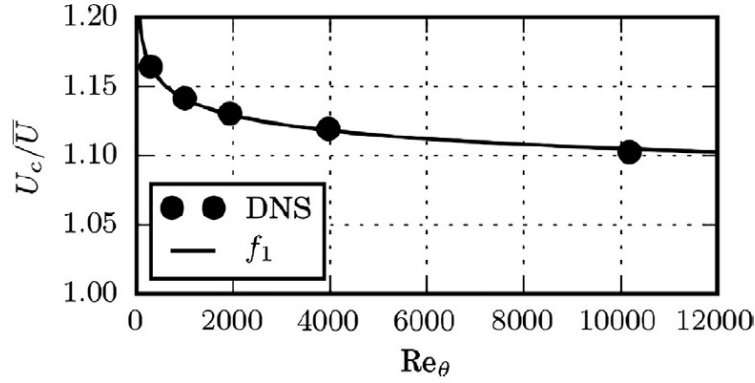
Figure 4.3: A plot of Equation 4.11 and corresponding DNS values of Lee and Moser [2015]. Illustration taken from Mukha and Liefvendahl [2017].

The Main Simulation

In the experiments of Devenport and Simpson [1990], the boundary layer at 2.15T upstream of the wing has a momentum thickness Reynolds number (Re_θ) of 6700 and a boundary layer thickness of 36mm at a freestream-velocity of 27 m/s. In order to mimic the conditions of the experiments of Devenport and Simpson [1990] and the LES of Ryu et al. [2016] in the present LES, the conditions of the boundary layer had to be determined at the inlet plane of the simulation. The boundary layer thickness at the inlet of the domain was determined by using (4.12). This equation is determined from a power-law fit for high-Reynolds number flows ($10^6 < Re < 10^9$) by Choi and Moin [2012]. By using the definition of the momentum thickness Reynolds number and (4.13) from Schlichting [2017], the kinematic viscosity of the fluid in the experiments was determined to be 1.41e-5 m^2/s.

$$\frac{\delta}{x} = 0.16 Re_x^{-\frac{1}{7}} \tag{4.12}$$

$$\theta = \frac{7}{72}\delta \tag{4.13}$$

In the equations above, δ is the boundary layer thickness, Re_x is the Reynolds number based on an equivalent flat plate length x, if the boundary layer starts growing from a length x=0 and θ is the boundary layer momentum thickness. By using the information of the experiments of Devenport and Simpson, the boundary layer thickness at the inlet of the domain was found to be δ_{inlet} = 0.0316m. This value is used in the procedure described above to generate a library of precursor simulation data to feed to the inlet of the simulation.

The remaining boundary conditions in the domain are more straightforward. The two sides and the top of the domain have a symmetry boundary condition, while the bottom and the wing have a no-slip wall boundary condition. At the outlet a boundary condition was used which fixes the pressure over the plane to 0. An overview of the boundary conditions for the simulation are given in Table 4.1.

Table 4.1: Overview of the boundary conditions for the main LES simulation.

Patch	Boundary Condition
INLET_BOT	Precursor-Method
INLET_TOP	Uniform free-stream velocity
OUTLET	Pressure = 0
SIDEL	Symmetry
SIDER	Symmetry
TOP	Symmetry
BOTTOM	No-slip wall
WING	No-slip wall

4.1.3. Geometry and Computational Domain

The geometry which will be used in the present LES-study is a 3:2 elliptical wing nose with a NACA0020-tail, which corresponds to the geometries used in the studies of Devenport and Simpson [1990] and Ryu et al. [2016], which will be used as validation data of the LES simulation. The wing has a maximum thickness of T = 71.7mm and a chord length of c = 4.254T. The wing is implemented on a flat plate which creates the wing-body junction geometry. The geometry is presented in Figure 4.4. The origin of the coordinate system is in the symmetry (xy-) plane at the location where the leading edge intersects with the flat plate geometry. A Cartesian coordinate system is used in which the x-coordinate is in the direction of the flow, the y-coordinate is in the wall-normal direction and the z-coordinate is in the spanwise direction.
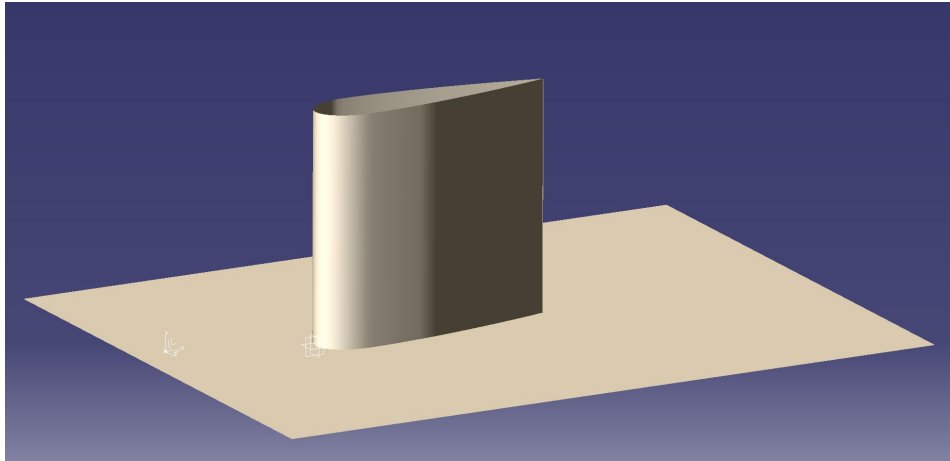
Figure 4.4: The wing-body junction geometry.

The computational domain is defined in Figure 4.5. The inlet of the domain is located upstream of the wing at a location of 1.4 chord lengths from the leading edge of the wing. The sides of the domain are indicated by SIDEL and SIDER, respectively, and are located at 1.5 chord lengths away from the symmetry plane. The height of the domain is four times the thickness of the wing, hence, y = 0.2868m. The outlet of the domain is located at 2.35 chord lengths from the trailing edge. The dimensions of the domain are inspired by the domain used by Ryu et al. [2016]. Furthermore, a height of 4T was chosen such that if spurious nonphysical velocities such as observed by Srikumar [2019] appear, they will not affect the region close to junction.

4.1.4. Solver Details

The LES simulations are conducted in the pimpleFoam solver of OpenFOAM, which is a transient solver of incompressible, turbulent flow of Newtonian fluids. In the pimpleFoam solver, the PIMPLE algorithm is employed to solve the filtered LES equations, which is a combination of the PISO (pressure-implicit split-operator) algorithm and the SIMPLE (semi-implicit method for pressure-linked equations) algorithm. These algorithms are iterative procedures to couple the momentum- and continuity equation. The PISO and PIM-PLE algorithm are used for transient simulations while the SIMPLE algorithm is used for steady-state simulations. Within each time- or solution step, the algorithms solve a pressure-equation in order to enforce mass conversation and then perform an explicit correction to the velocity field to satisfy the momentum equation.

In the solver, a set of numerical schemes are used to solve the equations. As a time scheme, the backward scheme is used, which is a second order implicit scheme. The numerical scheme that is used to solve gradients is the "Gauss linear" scheme. In the "Gauss linear" scheme, Gauss indicates the finite volume discretisation of Gaussian integration, while the "linear"-term indicates the interpolation scheme, which in this case is linear interpolation/central differencing. For the laplacian schemes, the "Gauss linear corrected" scheme was used. For the pressure solver the Preconditioned Conjugate Gradient (PCG) solver with a Diagonal Incomplete-Cholesky (DIC) preconditioner was used. This solver was chosen due to the fact that the performance (wall-time per time-step) of this solver at a high number of cores (n_{cores}>500) is much better than that of the Geometric Algebraic Multi-Grid (GAMG) solver. The tolerance of the solver is 1e-6. For the other equations the smoothSolver with the Gauss Seidel smoother is used. The number of nCorrectors was set to 2, which means that the algorithm solves the pressure equation and momentum corrector twice for every time-step. The number of nNonOrthogonalCorrectors was set to 1, which means that the solution of the
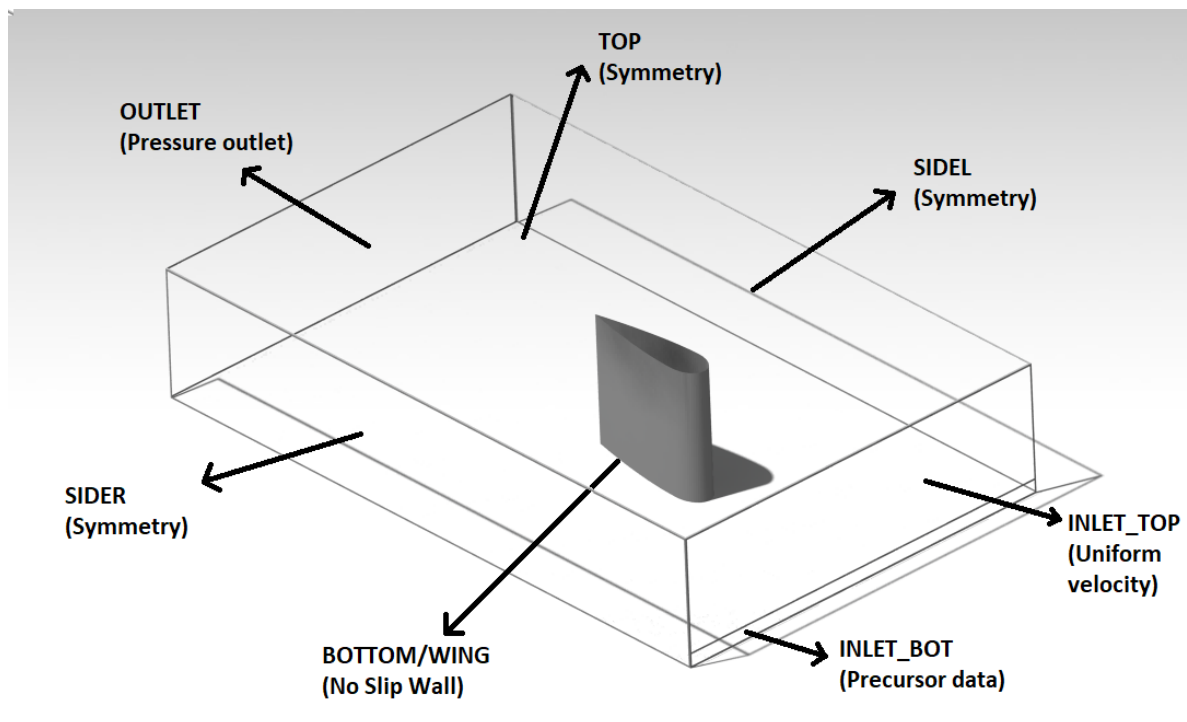
Figure 4.5: The computational domain of the LES-simulation.

pressure equation is repeated and corrected for non-orthogonality. The subgrid-scale model which is used in the simulation is the WALE model.

To maintain the numerical stability of the simulation, the time-step of the simulation was chosen to keep the maximum CFL-number from exceeding a value of 1.0. The CFL-number is defined in (4.14), in which U is the magnitude of the instantaneous velocity in a cell, Δx the length of this cell and Δt the time-step of the simulation. The time step which is used is determined by setting CFL=1 in (4.14) and determining the time-step for every cell given the velocity in the cell and the length of the cell. In order to keep the simulation stable, the smallest time-step is used. Based on the mesh used for the main-simulations, a time-step of $\Delta t = 1.85\text{e-}6$ s is used. A similar approach was taken for the precursor simulation, however, to initialise the precursor simulation, a variable time-stepping approach was used to speed up the initialisation of the simulation until the transient stage of the simulation was finished.

$$CFL = \frac{U\Delta t}{\Delta x} \tag{4.14}$$

In order to check whether the simulation is statistically stationary, instantaneous and time-averaged values of the three components of the velocity-vector and the pressure were plotted over time at several location in the domain for both the precursor simulation and main simulations. Examples of this are given in Figure 4.6a and in Figure 4.6b, in which the averaged and instantaneous flow quantities are plotted for two locations of the main simulation in the symmetry plane in front of the wing, respectively. Figure 4.6a is located at 100mm upstream from the wing and 5mm from the bottom wall. Due to the fact that the probe is in close proximity of the wall, one can see large fluctuations in the instantaneous-velocity components and this is an indication of near-wall turbulence. The second probe (Figure 4.6b) is located at 10mm upstream from the wing and 25mm from the bottom wall. One can observe that because the second probe is in closer proximity to the wing, the velocities are lower and the pressure is higher as the flow gets closer to the stagnation point on the wing. Once the transient stage of the simulation is over, the simulation is continued to sample the data of the flow.

Probe Location: X/T =-1.3947 Y/T =0.0697
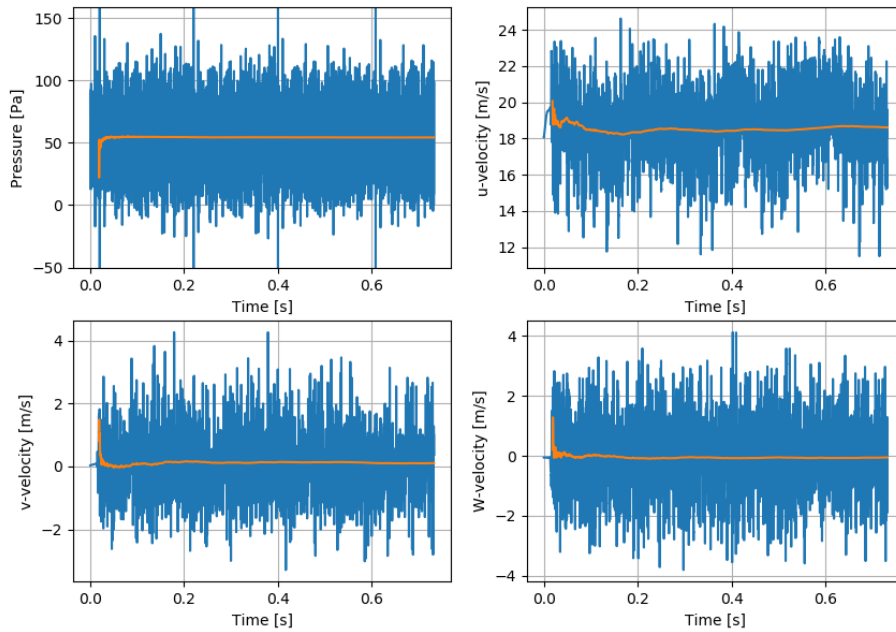
(a) Probe location: X/T = -1.3947 and Y/T = 0.069735

Probe Location: X/T =-0.1395 Y/T =0.3487
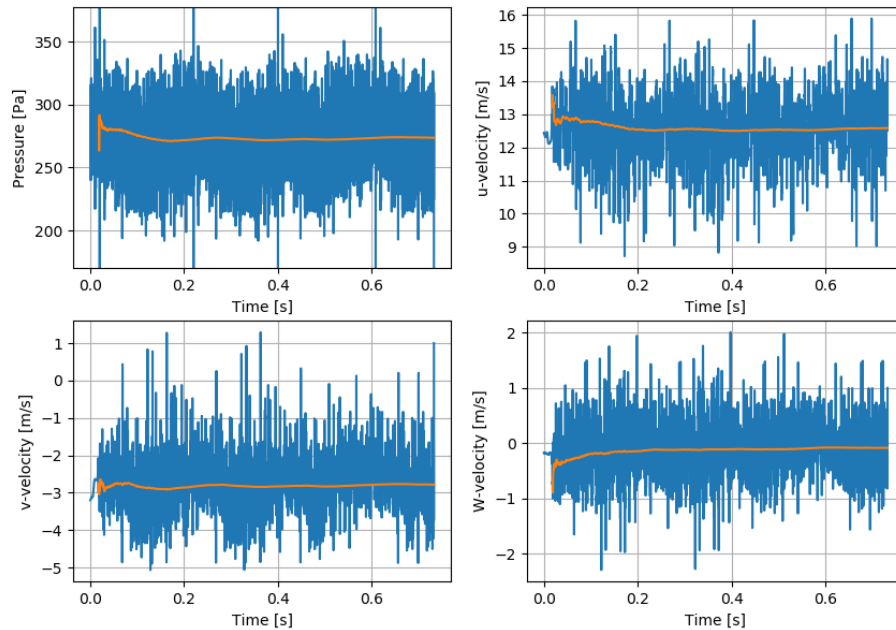
(b) Probe location: X/T = -0.13947 and Y/T = 0.348675

Figure 4.6: Instantaneous and averaged pressure and velocities at two probes in the symmetry plane ahead of the wing.

4.1.5. Mesh Generation

In this subsection, the generation of the computational mesh will be discussed. First the mesh generation of the main simulation will be discussed, which is followed by a discussion of the mesh generation of the precursor simulation.

The Main Simulation

The mesh of the simulation was generated with Ansys ICEM. A C-grid mesh was generated around the wing. The mesh count of the body-fitted mesh is 61.7 million hexahedral cells for the wall-resolved simulation. The mesh count and the meshing laws used when meshing were based on recommendations of Choi and Moin [2012] and the LES simulations of Ryu et al. [2016] and Gand et al. [2010b]. Choi and Moin [2012] notes that for wall-resolved large eddy simulations, typical values used for Δx^+ is between 50 and 130, for Δz^+ is approximately between 15 and 30 and the number of cells in y-direction (wall- normal direction) up to y^+ is between 10 and 30 cells. Gand et al. [2010b] used $\Delta x^+ = 50$ in the streamwise direction, $y^+ = 1$ in the wall-normal direction and $\Delta z^+ = 25$ in the spanwise direction. The meshing is for a large part controlled by bigeometric meshing laws, which allows to control the ratio of two successive cells such that the coarsening of the mesh is not too rapid.

The first cell-size in the wall normal direction has a cell-size of y = 1e-5 meter, which corresponds to a $y^+ < 1$, which is required for wall-resolved Large Eddy Simulations. Furthermore, an inflation ratio of 1.075 was used until a Δy^+ was achieved similar to those of Gand et al. [2010b] and Srikumar [2019] after which the cell size was kept constant until a height of 3T was reached. The inflation ratio is defined as the ratio between the length of two successive cells in the same direction. Between a height of 3T and 4T, quick coarsening of the mesh occurs at an inflation ratio of 1.09, such that this region is not too costly to compute, but still allows for spurious velocities to occur such as observed by Srikumar [2019], without affecting the first 3T of the simulation. In total, 81 cells are located in the boundary layer. In the x-direction of the domain, the mesh is spaced at most $\Delta x^+ = 50$, while closer to the wing this spacing is reduced towards the values which are required near the wall are reached. Finally, in the spanwise direction a Δz^+ of 20 has been used near the symmetry plane, after which the Δz^+ is slowly increased at an inflation ratio of 1.04. Again, near the wing, due to constraints on the mesh on resolving the wall, the Δz^+ was smaller than 20 at some locations. Near the sides (SIDEL and SIDER) of the domain, the requirements on the mesh are more relaxed as the flow quantities are less interesting near the boundaries of the domain and therefore a coarser mesh is present to keep the mesh count manageable. In Figure 4.7, one can find a cross-section of an x-normal plane at the middle of the domain from the mesh around the wing geometry, while in Figure 4.8 one can see a top view of the computational around the wing.
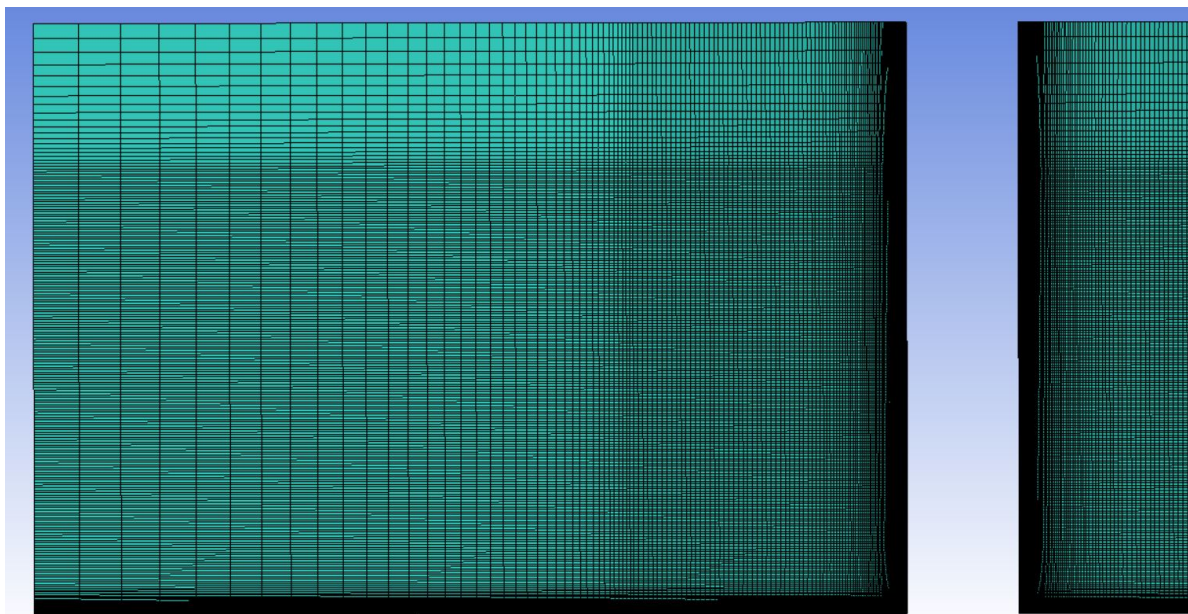
Figure 4.7: Cross-section of the mesh at an x-normal plane at the middle of the domain of the main simulation. The empty space between the meshes is the location of the wing.
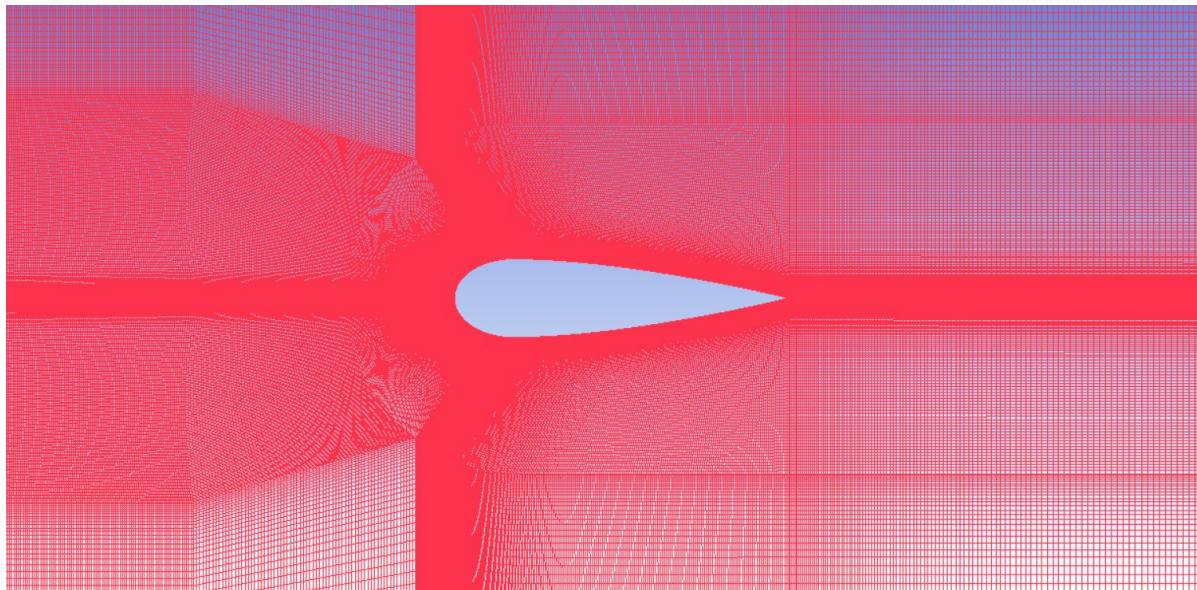
Figure 4.8: Top view of the computational mesh of the main simulation.

The Precursor Simulation

For the precursor mesh, similar guidelines as for the main simulation have been followed. Furthermore, Mukha and Liefvendahl [2017] suggests that for the sampling plane of the precursor simulation, the exact same grid as at the inlet plane of the main simulation should be used. However, due to the working mechanism of the *meanVelocityForce* function as a momentum source in OpenFOAM, it was found that it is required to use an uniform spacing in the spanwise direction to achieve good results for the turbulent channel flow. Therefore, a uniform spanwise spacing of $\Delta z+ = 25$ has been used. This results in a mesh of the precursor which is not matching that of the main simulation. Therefore, mesh interpolation techniques have been employed to generate a library of simulation data which matches the mesh of the inlet of the main simulation.

To achieve this library of simulation data, a Python package for turbulent inflow generation called *Eddylicious* was used as suggested by Mukha and Liefvendahl [2018]. Due to the fact that the Python package only takes into account the velocity field and no thermodynamic quantities, the package can only be used for incompressible flows. From the *Eddylicious* package, the *runInterpolation* functionality was employed to interpolate data from one 2-dimensional point set to another, which in this case is the sampled data from the precursor mapped on the bottom part of the inlet of the main simulation. The nearest-neighbour interpolation technique has been employed within this method and generates the *boundaryData* folder in the OpenFOAM native file format which is required for the *timeVaryingMappedFixedValue* boundary condition.

The height of the domain is two boundary layer thicknesses with at the top and bottom of the domain a wall. From both walls, the same y-spacing in the boundary layer has been used as in the boundary layer region of the main simulation. Furthermore, a spacing of $\Delta x+ = 50$ has been used in the x-direction of the domain. Resulting in a mesh count of 69.5 million hexahedral cells.

Computational Resources

In order to perform these wall-resolved Large Eddy Simulations, a large amount of computational resources are required. Therefore, a request was made to the NWO (Netherlands Organisation for Scientific Research) for computing time on Cartesius, the Dutch supercomputer. The NWO granted a total of 6.55 million core hours of computational time under projectnumber 2019.048.

In order to determine the required computational resources per simulation, a rule of thumb is followed which says that approximately 50.000 cells per core is desired. Given the mesh count of the precursor and main simulation, this results in a total number of cores per simulation in the 1200 to 1300 range. More specifically, the precursor was run at 1248 cores, while the main simulation was run at 1272 cores. Given this core count, the simulation takes approximately between 6 to 7 seconds per time step on average for both the precursor and the main simulation. To simulate 1.0 second in simulation time at a time-step of 1.85e-6 seconds, it would require 540541 time-steps which equals 1051 hours of non-stop running at an average of 7 seconds

per time-step. Which results in 44 days of non-stop running. In practice, the time to get the results is much larger due to queue time to acquire the required nodes and down time. Given the required simulation time, a total of 1.3 million core hours is required to run 1 second of simulation time for both the main-simulation and the precursor.

The simulations are run on the thin nodes of Cartesius which have 24 cores and a memory of 64GB. Within the thin nodes, a difference is made between Haswell nodes and Ivy Bridge nodes. The Haswell nodes have a higher clock frequency than the Ivy Bridge nodes, the clock frequencies are 2.6 GHz and 2.4 GHz, respectively. Furthermore, the Haswell nodes contain a newer generation of InfiniBand adapters and the bandwidth of the memory is larger (2133 MT/s DDR4 memory with respect to 1866 MT/s DDR3 memory for the Ivy Bridge nodes). As a result of this, the Haswell nodes can be up to 10%-40% faster in terms of computational speed. This was also the experience of the author, and therefore, the simulation was constraint to use only Haswell nodes.

Due to the fact that Cartesius only allows 8TB of data and 4 million files per user on the scratch file system and the large amount of data files that are generated by the LES simulations, data management and storage is very important. This is especially the case due to the fact that files older than 14 days, will be deleted automatically by the system.

4.2. Numerical Methodology: RANS Simulation

In this Section, the numerical methodology and the theory behind a Reynolds-Averaged Navier-Stokes Simulation will be presented. First, the equations which govern the simulation will be presented, which is followed by presenting the boundary conditions and solver details. As the RANS-simulation will be used as an initialisation of the flow field of the LES-simulation, the same mesh and domain as presented in the section above will be used. Furthermore, a coarse RANS simulation will be performed to compare to the results of the LES.

Governing Equations

Starting from the Navier-Stokes equations for an incompressible, Newtonian fluid as presented in differential form in (4.15) and (4.16), we will derive the Reynolds-Averaged Navier-Stokes (RANS) equations.

$$\frac{\partial u_i}{\partial x_i} = 0 \tag{4.15}$$

$$\frac{\partial u_i}{\partial t} + u_j \frac{\partial u_i}{\partial x_j} = -\frac{1}{\rho}\frac{\partial p}{\partial x_i} + \nu \frac{\partial^2 u_i}{\partial x_j \partial x_j} + f_i \tag{4.16}$$

The RANS-equations are the time-averaged equations of motion and are derived from doing a Reynolds decomposition on the Navier-Stokes equations, in which a decomposition is made of the instantaneous quantities into time-averaged and fluctuating quantities. The fluctuating quantities have the property that the mean of the fluctuating quantity is zero. The Reynolds decomposition of the velocity and the pressure are:.

$$u = \overline{u} + u', \tag{4.17}$$

$$p = \overline{p} + p'. \tag{4.18}$$

In the equations above, u and p are the instantaneous velocity and pressure, $\overline{u}$ and $\overline{p}$ are the mean velocity and pressure and u' and p' are the fluctuating velocity and pressure. By substituting these definitions in the incompressible Navier-Stokes equations and averaging these equations in time results in the RANS-equations:

$$\frac{\partial \overline{u}_i}{\partial x_i} = 0, \tag{4.19}$$

$$\frac{\partial \overline{u}_i}{\partial t} + \overline{u}_j \frac{\partial \overline{u}_i}{\partial x_j} + \overline{u'_j \frac{\partial u'_i}{\partial x_j}} = -\frac{1}{\rho}\frac{\partial \overline{p}}{\partial x_i} + \nu \frac{\partial^2 \overline{u}_i}{\partial x_j \partial x_j} + \overline{f}_i. \tag{4.20}$$

The momentum equation presented in (4.20) can be rewritten as:

$$\frac{\partial \overline{u}_i}{\partial t} + \overline{u}_j \frac{\partial \overline{u}_i}{\partial x_j} = -\frac{1}{\rho}\frac{\partial \overline{p}}{\partial x_i} + \nu \frac{\partial^2 \overline{u}_i}{\partial x_j \partial x_j} + \overline{f}_i - \frac{\partial \overline{u'_i u'_j}}{\partial x_j}. \tag{4.21}$$

One can see that (4.21) is similar in shape to the Navier-Stokes equation in (4.16), with an additional term due to the Reynolds decomposition. To get the steady RANS-equations, one can remove the time-varying term of (4.21). Due to the Reynolds decomposition, the RANS-equations are not closed due the new unknown term called the Reynolds Stress, $\left(-\overline{u_i' u_j'}\right)$. The Reynolds-stress is an additional term which requires to be modelled, which is done by turbulence models.

A very common approach to model the Reynolds-stress is by means of the turbulent-viscosity hypothesis, which was introduced by Boussinesq in 1877. In this so called Boussinesq approximation, a distinction is made between an isotropic-part ($\frac{2}{3} k \delta_{ij}$) and an anisotropic ($2 k b_{ij}$) part of the Reynolds stress, as described in (4.22). Pope [2000]; In this equation, k is the turbulent kinetic energy and $b_{ij} = -\frac{\nu_T S_{ij}}{k}$, where ν_T is the eddy viscosity and S_{ij} is the mean-strain rate tensor.

$$\overline{u_i' u_j'} \approx 2k \left(b_{ij} + \frac{1}{3} \delta_{ij} \right) \tag{4.22}$$

Linear Eddy Viscosity models (LEVM) try to model a relationship for the Reynolds stresses as a function of the mean strain-rate. This closure problem is solved by Linear Eddy Viscosity models by finding a model for the eddy viscosity ν_T. The turbulence model which is used in the present study is the k-ω SST model as proposed by Menter [1994], which involves solving two extra transport equations for the turbulent kinetic energy k and the dissipation rate ω.

Boundary Conditions

In contrast to a Large Eddy Simulation,, a RANS simulation does not require a time-resolved inflow boundary condition. Instead, the inflow condition at the inlet is steady and does not vary in the spanwise-direction. In the wall-normal direction, the velocity varies due to the boundary layer velocity profile. The boundary layer thickness is fixed at the inlet and has been determined by the power-law fit for high-Reynolds number flows of (4.12) of Choi and Moin [2012]. To reproduce the experiments of Devenport and Simpson [1990], it is required that the boundary layer has a momentum thickness Reynolds number of (Re_θ) of 6700 and a boundary layer thickness of 36mm at a freestream-velocity of 27 m/s at 2.15T upstream of the wing. Given this information, the boundary layer thickness at the inlet was found to be δ_{inlet} = 0.0316m. This is the same as for the LES simulation due to the fact that the same computational domain and grid are used in order to initialise the LES simulation.

In order to generate a proper boundary layer profile for the given boundary layer, the Reichardt profile as presented in the equations below is used:

$$u^+ = \frac{1}{\kappa} \ln\left(1 + \kappa y^+\right) + 7.8 \left[1 - e^{\left(\frac{-y^+}{11}\right)} - \frac{y^+}{11} e^{\left(\frac{-y^+}{3}\right)} \right], \tag{4.23}$$

$$u^+ = \frac{u}{u_\tau}, \tag{4.24}$$

$$y^+ = \frac{y u_\tau}{\nu}. \tag{4.25}$$

In the (4.23) u^+ is the non-dimensional velocity and y^+ is the non-dimensional wall distance and are defined in (4.24) and (4.25), respectively. Furthermore, κ is the von Kármán constant and u_τ is the friction velocity. In order to get a boundary layer profile which matches the requirements at the inlet of the domain, the corresponding friction velocity has to be found. The friction velocity is defined by (4.26). In (4.26), τ_w is the wall-shear stress and is defined by (4.27). To find a proper boundary layer profile, a correct coefficient of friction C_f corresponding to the boundary layer properties has to be defined. The above procedure has been implemented in a Python script in order to generate the inflow condition for the RANS-simulation for y < δ. For y > δ, a uniform velocity field which corresponds to the free-stream velocity of 27m/s has been assigned.

$$u_\tau = \sqrt{\frac{\tau_w}{\rho}} \tag{4.26}$$

$$\tau_w = \rho \nu \left(\frac{d\overline{u}}{dy} \right)_{y=0} = C_f \frac{1}{2} \rho U_\infty^2 \tag{4.27}$$

The remainder of the boundary conditions in the RANS-simulation are more straightforward. Similar as to the LES Simulation, the sides and the top of the domain are given a symmetry boundary condition while
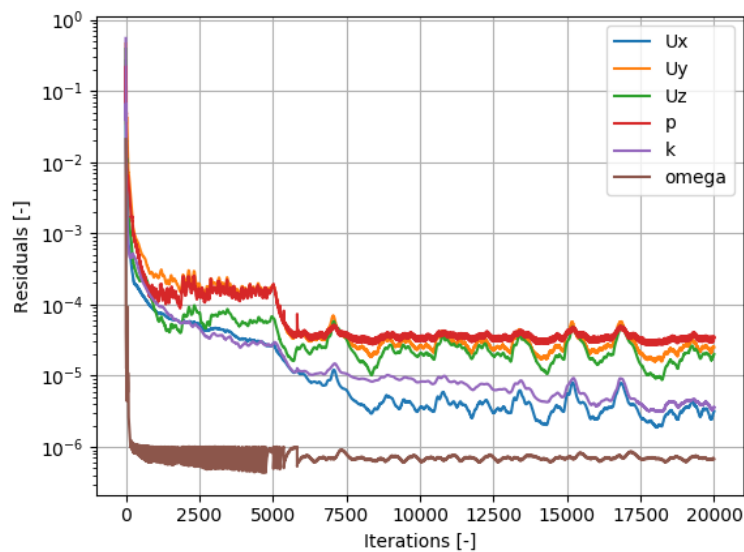
Figure 4.9: Residuals of the RANS-simulation to initialise the LES-simulation.

the wing and the bottom of the domain are given a no-slip wall boundary condition. The outlet has a zero pressure boundary condition. All boundary conditions are summarised in Table 4.1

Table 4.2: Overview of the boundary conditions for the RANS simulation.

Patch	Boundary Condition
INLET_BOT	Reichardt Boundary Layer Profile
INLET_TOP	Uniform free-stream velocity
OUTLET	Pressure = 0
SIDEL	Symmetry
SIDER	Symmetry
TOP	Symmetry
BOTTOM	No-slip wall
WING	No-slip wall

Solver Details

The RANS simulations are conducted in the SimpleFoam solver of OpenFOAM, which is a steady-state solver for incompressible, turbulent flow of Newtonian fluids. In the SimpleFoam solver, the SIMPLE (semi-implicit method for pressure-linked equations) algorithm is used to solve the RANS equations. As a turbulence model, Menter [1994] its k-ω SST model will be used based on the results of Apsley and Leschziner [2001], which found that from the turbulence models of the LEVM-type, the k-ω SST model performed best in junction flows. For the RANS simulation, a convergence criteria was set and the solver was deemed to be converged if the residuals of the velocity components U, V, W, the pressure p, the turbulent kinetic energy k and the specific dissipation rate ω are in the order of O(1e-5). Furthermore, a maximum iteration count was set to be 20,000 iterations, in the case not all the flow quantities reached the convergence criteria. In that case, it was checked if the residuals were sufficiently close to the convergence criteria to accept or reject the results of the simulation. In Figure 4.9, one can see the residuals of the RANS-simulation which was used to initialise the main LES simulation.

As the pressure solver the geometric-algebraic multigrid (GAMG) solver was used with a GaussSeidel smoother while for the rest the smoothSolver with as a smoother the symGaussSeidel was used. As a time scheme for the steady-state RANS simulation was chosen the "steady-state" option in OpenFOAM, which sets the time-derivative of the RANS-equations to zero and resulting in solving the steady-state RANS-equations. The discretisation scheme that is used by default for the gradient terms is the "Gauss linear" scheme. In the

Gauss linear scheme, the Gauss-term refers to the standard finite volume discretisation of Gaussian integration which requires the interpolation of values from cell centres to face centres. The linear term refers that as an interpolation scheme, linear interpolation is used, which means a central differencing scheme. For the divergence schemes, no default scheme can be used, due to the fundamentally different nature of the different terms in this sub-directory. For $div(\phi, U)$, the advection of the velocity, the Gauss linearUpwind grad(U) scheme is used which is an second order, upwind biased, unbounded scheme that requires the discretisation of the velocity gradient to be specified. For the remainder of the divergence schemes the Gauss linear scheme, which is a second order unbounded scheme, and the Gauss limitedLinear 1 scheme is used, which is a scheme that limits towards upwind in regions of rapidly changing gradient. Finally, as laplacianSchemes the Gauss linear corrected scheme was used.

<div style="text-align: right; font-size: 4em;">5</div>

Results & Discussion: Wall-Resolved LES

In this Chapter the results of the wall-resolved Large Eddy Simulation will be presented. First, the simulation is validated by making a comparison with experimental and numerical validation data. Furthermore, the results of the wall-resolved LES will be compared to a RANS simulation and the wall-modelled LES simulation of Srikumar [2019]. Finally, the regions of uncertainty in RANS-simulations will be identified by analysis of the high-fidelity data.

5.1. Comparison of the Wall-Resolved LES with Experimental and Numerical Data

In this section, the wall-resolved LES simulation will be validated by comparing the data of the wall-resolved large eddy simulation to experimental validation data of Devenport and Simpson [1990] and the numerical study of Ryu et al. [2016]. Furthermore, a comparison will be made with a coarse mesh RANS simulation and with the wall-modelled LES simulation of Srikumar [2019] to indicate the differences between a RANS Simulation, wall-modelled LES simulation and a wall-resolved LES simulation. To do so, comparisons will be made of the upstream boundary layer profiles at several locations upstream of the wing in the symmetry plane of the domain, comparisons of the time-averaged spanwise vorticity and comparisons of the time-averaged turbulent kinetic energy. Also, an analysis of the corner flow in the symmetry plane will be given and the mean flow at the bottom wall will be analysed.

5.1.1. Upstream Boundary Layer Profiles

First, a comparison of the boundary layer profiles upstream of the wing in the symmetry plane (Z = 0) will be made of both the U-velocity component and the V-velocity component. This comparison is made to test whether the inlet boundary condition generates a realistic turbulent boundary layer that corresponds to the experimental results of Devenport and Simpson [1990]. The U-velocity boundary layer profiles are given in Figure 5.1 and the V-velocity boundary layer profiles are given in Figure 5.2. It should be noted that in these figures that the X and Y-coordinates are normalised by the thickness of the wing (T = 0.0717m) and that the velocity components are normalised by the reference velocity ($U_\infty = 27.0 \, \text{m/s}$).

Figure 5.1 shows the comparison of the mean streamwise velocity profiles between a coarse RANS simulation, the wall-resolved LES simulation and the experimental results of Devenport and Simpson [1990]. In general, it can be observed that the LES-simulation shows good agreement to the experimental results. However, it should be noted that the upstream boundary layer is thinner than the results observed by Devenport and Simpson [1990], which accounts for differences observed in the horseshoe vortex system. Devenport and Simpson [1990] shows that flow separation occurs at X/T = -0.47 due to the strong adverse pressure-gradient imposed by the wing. The wall-resolved LES, correctly predicts this location of flow-separation, while for the RANS simulation the location of flow-separation is further upstream of the wing at X/T=-0.61. However, as one can see especially at the velocity-profiles at X/T=-0.25 and X/T=-0.15, there is an underprediction of the LES in the amount of flow reversal induced by the adverse-pressure gradient, while for the RANS simulation there is a strong flow recirculation. Another notable difference of the LES with experimental results is at X/T=-0.86, where the mean streamwise velocity is slightly overpredicted. The results of the wall-resolved LES of Ryu

et al. [2016] shows similar behaviour of the boundary layer profiles, which gives confidence in the correctness of the present wall-resolved LES simulation.

Figure 5.2 shows the comparison of the mean wall-normal velocity profiles between a coarse RANS simulation, the wall-resolved LES simulation and experimental validation data. The first observation that can be made is that in general the LES simulation is in agreement with the experimental validation data, with the exception for X/T=-0.15, where the LES result has the opposite sign of the experimental results. This can be explained by that the horseshoe vortex is observed at this location in the LES simulation, which is slightly downstream with respect to the experimental results and can also be observed in the vorticity (Figure 5.4) and turbulent kinetic energy (Figure 5.5) plots. For the RANS simulation at stations X/T=-0.3, X/T=-0.25 and X/T=-0.2 the velocity profile has the opposite sign of the results of the experimental data. Hence, the RANS simulation was unable to correctly predict the by Devenport and Simpson [1990] described ejected flow at these stations.
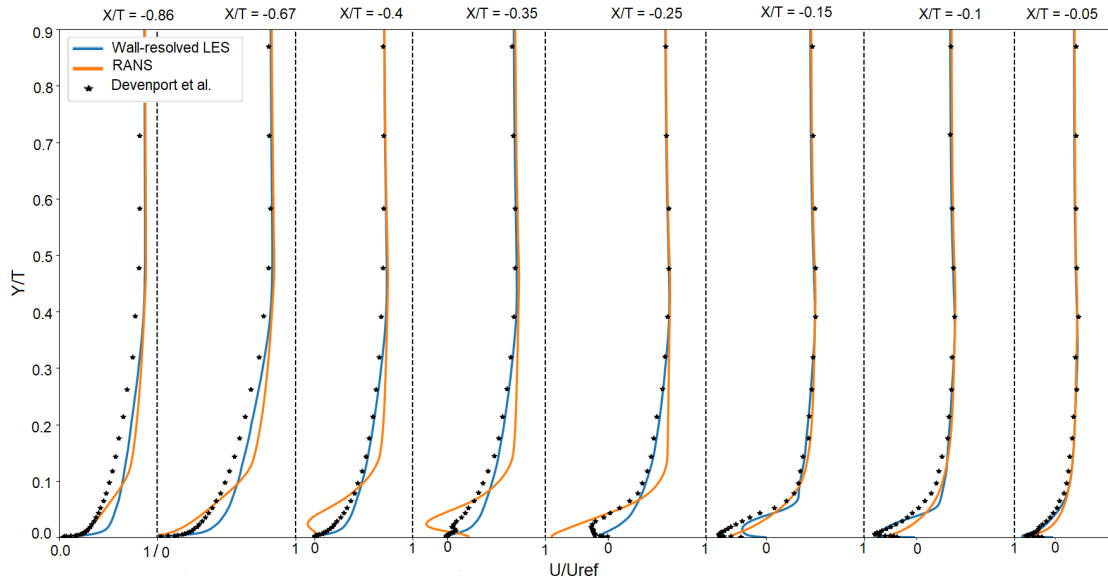
Figure 5.1: Comparison of the mean streamwise velocity boundary layer profiles upstream of the wing in the symmetry plane (Z = 0).
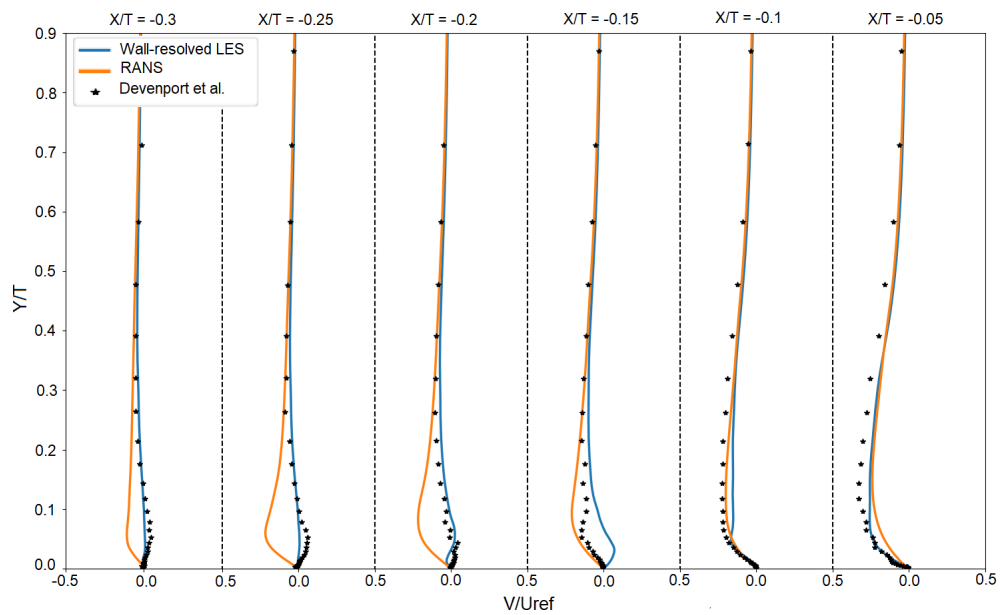
Figure 5.2: Comparison of the mean wall-normal velocity boundary layer profiles upstream of the wing in the symmetry plane (Z = 0).

5.1.2. Pressure Distribution

Figure 5.3 shows the comparison of the mean wall-pressure coefficient distribution around the wing nose between results from simulations and the experimental validation data. As can be seen from 5.3a, the wall-resolved LES shows good agreement to the measurements of Devenport and Simpson [1990]. The main difference with the experimental data is that the location and magnitude of the region of locally low pressure on the side of the wing. The location of the region of low pressure is in the LES simulation slightly upstream of the experimental results at X/T=-0.6, while the location of the region of low pressure for the experimental results is at X/T=-0.75.

Figure 5.3b shows that the RANS-simulation has also fairly good results when comparing to the experimental data. Similar to the LES results, the RANS-simulation predicts the region of low pressure further upstream than the experimental results do. Furthermore, the RANS-simulation shows highly kinked contour lines close to the leading edge of the wing, which are not observed in the LES simulation. Ryu et al. [2016] observed similar results to the present study while the DES of Paik et al. [2007] and the wall-modelled LES of Srikumar [2019] also showed the kinked lines in proximity of the wing nose. Since, RANS-simulations, DES-simulations and wall-modelled LES simulations all use wall-models and therefore, not completely resolve the near-wall dynamics of the flow, it is expected that these kinked lines are numerical artefacts of these wall-models. Overall, the mean wall-pressure coefficient distribution is resolved satisfactory.

(a) Wall-resolved LES

(b) RANS
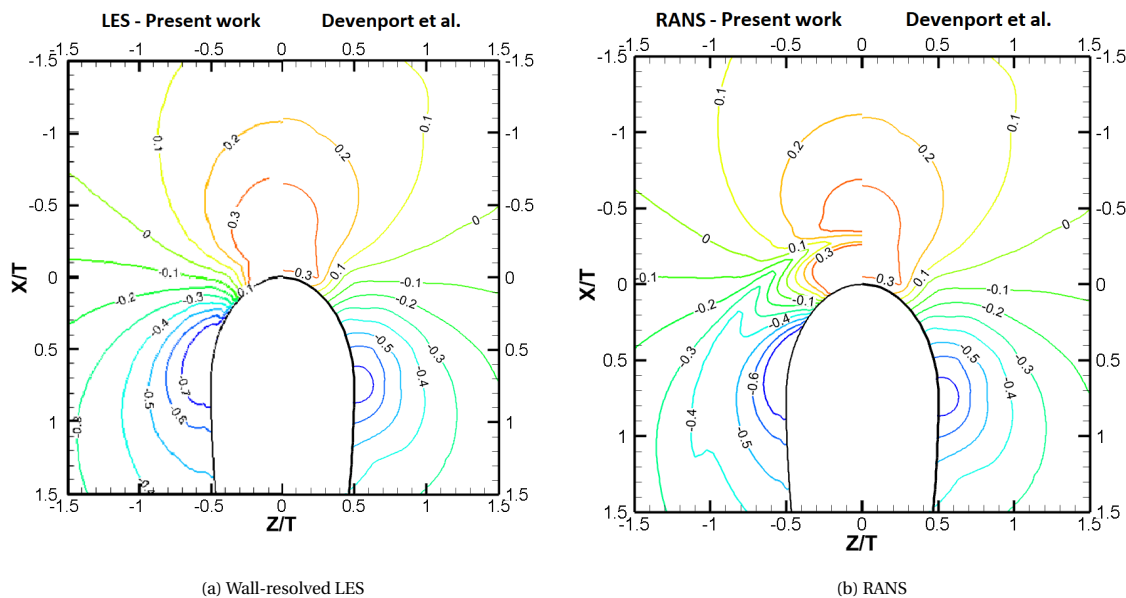
Figure 5.3: Comparison of the pressure coefficient distribution of the LES and RANS simulation with experimental validation data of Devenport and Simpson [1990].

5.1.3. Time-Averaged Spanwise Vorticity Contours

Contours of the time-averaged spanwise vorticity in the symmetry plane upstream of the wing can be found in Figure 5.4. The results of the wall-resolved LES simulation (Figure 5.4b) will be compared to the experimental results (Figure 5.4a), the results of the wall-modelled LES (Figure 5.4c) of Srikumar [2019] and the RANS simulation (Figure 5.4d) of the present study. It should be noted that the spanwise vorticity is non-dimensionalised by the thickness of the wing T and the freestream velocity U_∞.

In the results of Devenport and Simpson [1990] in Figure 5.4a, one can see the characteristic elliptical mean flow structure which is slightly lifted from the bottom wall due to the bimodal dynamics of the horseshoe vortex. When comparing the LES of the present study to the results of Devenport, one can see that the characteristic elliptical shape and the magnitude of the negative vorticity is nicely captured by the wall-resolved large eddy simulation. However, the location of the maximum magnitude is located slightly upstream (X/T=-0.15) with respect to the experimental data (X/T=-0.20). This can be explained due to the fact that for the inlet boundary condition, a larger development region for the boundary layer was required due to the use of a turbulent channel flow precursor instead of a fully developed flat plate turbulent boundary layer precursor, which results into a fully developed turbulent boundary layer closer to the region of interest with

respect to a flat plate turbulent boundary layer precursor which does not require any development region. As a results of this and the sensitivity of the flow physics to the inlet boundary condition, the flow structure is shifted closer to the wall.

Also, the wall-resolved LES correctly captures the region of positive vorticity near the wall which is induced by the large amount of backflow in the junction region which is also visible in the boundary layer profiles in Figure 5.1 and Figure 5.2. Similarly, there is a region of positive vorticity close the wall of the wing in the wall-resolved LES simulation. This region of positive vorticity close to the wing was not captured by the wall-modelled LES of Srikumar [2019], due to not having enough cells in the near-wall regions to properly capture the near wall-dynamics and the fact that they used an immersed-meshing approach with respect to a body-fitted mesh. However, Srikumar [2019] did capture the correct location of the horseshoe vortex at X/T=-0.20.

The RANS-simulation was not able to capture the characteristic elliptic lifted flow structure with the k-ω SST turbulence model, instead, it predicts a smooth blob of negative vorticity which is locally lifted slightly at X/T=-0.4. Furthermore, the core of the region of negative vorticity is located further upstream (X/T=-0.3) with respect to the experimental results. Overall, the results of the LES match very well to the experimental results, while there is some mismatch between the results of the RANS simulation and the experimental results.

(a) Experimental results of Devenport and Simpson [1990]

(b) Wall-resolved LES - present study

(c) Wall-modelled LES of Srikumar [2019]

(d) RANS - present study
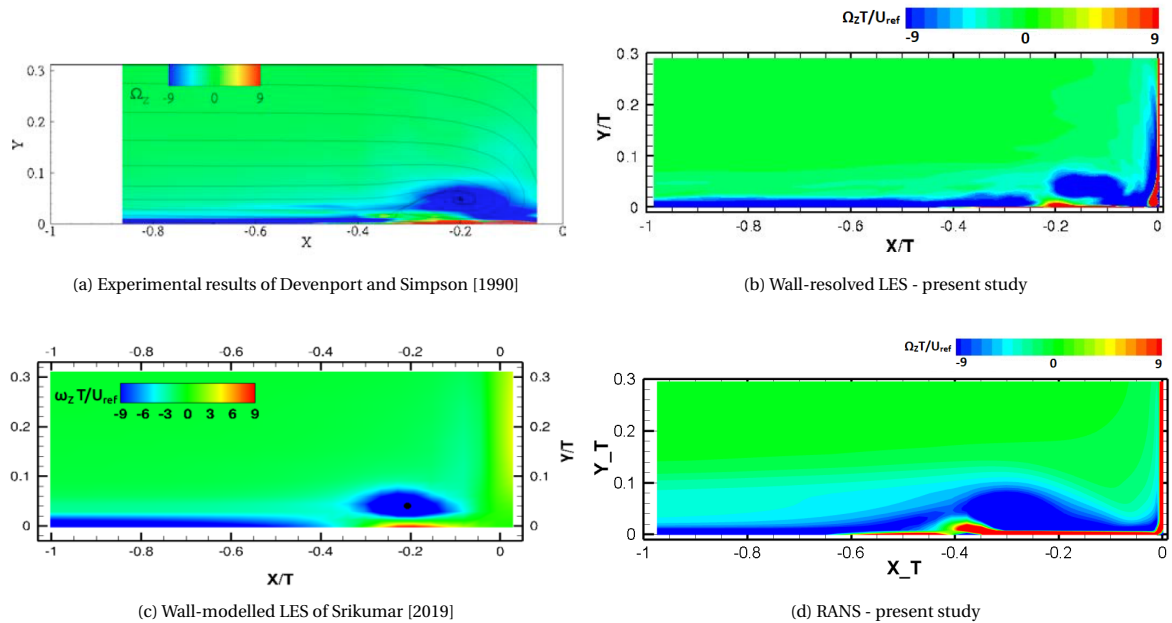
Figure 5.4: Contour plots of the time-averaged spanwise vorticity in the symmetry plane (Z=0) upstream of the wing.

5.1.4. Time-Averaged Turbulent Kinetic Energy Contours

Contours of the time-averaged (resolved) turbulent kinetic energy in the symmetry plane upstream of the wing can be found in Figure 5.5. The results of the wall-resolved LES simulation (Figure 5.5b) will be compared to the experimental results (Figure 5.5a), the results of the wall-modelled LES (Figure 5.5c) of Srikumar [2019] and the RANS simulation (Figure 5.5d) of the present study. It should be noted that the turbulent kinetic energy is non-dimensionalised by the freestream velocity squared, U_∞^2.

As can be seen from Figure 5.5, the turbulent kinetic energy peak is present close to the core of the horseshoe vortex, which is located for the experimental data at X/T=-0.2, while for the present LES study, it is located at X/T=-0.15. Again, the location of the peak of turbulent kinetic energy can be explained due to the sensitivity of the horseshoe vortex to the inlet boundary condition. The turbulent channel flow precursor results in a different boundary layer profile than a flat plate turbulent boundary layer precursor. This difference at the inlet boundary condition in combination with the sensitivity of the mean junction vortex to the boundary conditions possibly caused the shift of the location of the mean vortex structure. The peak turbulent kinetic energy is k/U_∞^2=0.05 for the experimental data and the shape of the peak region is a characteristic C-shape. This characteristic shape and the magnitude of the peak turbulent kinetic energy is nicely captured by the wall-resolved LES simulation. Furthermore, a secondary corner vortex can be indicated in the bottom

right corner close to the walls in Figure 5.5b.

In contrast to present LES, the wall-modelled LES of Srikumar [2019] in Figure 5.5c predicts the location of the peak turbulent kinetic energy (X/T=-0.23) closer to the location of the experimental results but in this case slightly upstream with respect to the experimental results. The peak turbulent kinetic energy of the wall-modelled LES is, with a value of k/U_∞^2=0.02, under predicted with respect to experimental data. Furthermore, the characteristic C-shape of the turbulent kinetic energy peak is not observed. The under prediction of the turbulent kinetic energy can be explained due to the wall-modelled approach of Srikumar [2019]. Since the peak turbulent kinetic energy is concentrated very close to the wall and in a wall-modelled approach the near-wall dynamics of the flow are not completely resolved, a large amount of the energy carrying eddies might not have been resolved, resulting in an under prediction of the turbulent kinetic energy.

Similarly to the results of the LES of Srikumar [2019], the peak turbulent kinetic energy determined by the RANS-simulation is about half the magnitude with respect to the wall-resolved LES results. However, the peak TKE magnitude is higher than that observed in the wall-modelled LES of Srikumar [2019]. Furthermore, also the characteristic C-shape of the peak cannot be identified in the RANS results. Finally, the location of the peak of turbulent kinetic energy is located at X/T=-0.3 more upstream with respect to the experimental results.

(a) Experimental results of Devenport and Simpson [1990]

(b) Wall-resolved LES - present study

(c) Wall-modelled LES of Srikumar [2019]

(d) RANS - present study
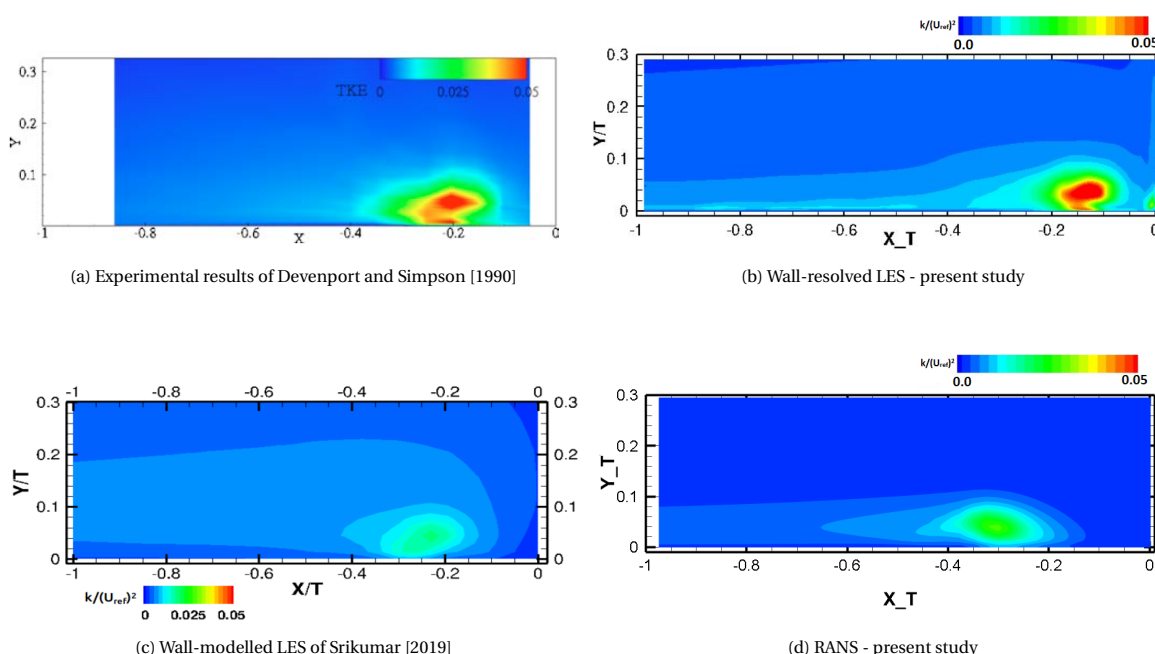
Figure 5.5: Contour plots of the time-averaged turbulent kinetic energy in the symmetry plane (Z=0) upstream of the wing.

5.1.5. Bimodal Dynamics of the Horseshoe Vortex

The most characteristic behaviour of the horseshoe vortex is the bimodal behaviour which was first reported by Devenport and Simpson [1990]. They explained the large turbulent stresses close to the junction vortex by a double-peaked probability density functions (pdf) of the U- and V- velocities in the region of the mean vortex structure due to the low-frequency bimodal oscillations of the horseshoe vortex system. The bimodal behaviour causes large pressure fluctuations in the region of the junction.

To validate whether the wall-resolved LES simulation properly resolves this bimodal behaviour, the time signal of the U-velocity component at the location of the horseshoe vortex has been analysed. Figure 5.6 shows the characteristic double-peaked pdf of the U-velocity component at X/T=-0.14 for several y-locations. Figure 5.6a shows a peak which is centered at a U-velocity of 0 m/s, which indicates the zero-flow mode of the horseshoe vortex system while the peak centered at a U-velocity of -12.5 m/s indicates the backflow mode. From Figure 5.6b and Figure 5.6c it can be observed that the back-flow mode gets stronger as one traverses the y-direction while the zero-flow mode dampens out, resulting eventually in a single backflow-peak in the pdf. As the y-location increases, this single-peaked pdf will shift towards a positively peaked pdf as observed in Figure 5.6d. Similar observations have been made in Figure 2.5 of Devenport and Simpson [1990].

(a) Y/T=0.00156 and X/T=-0.14

(b) Y/T=0.00462 and X/T=-0.14

(c) Y/T=0.01563 and X/T=-0.14

(d) Y/T=0.11343 and X/T=-0.14
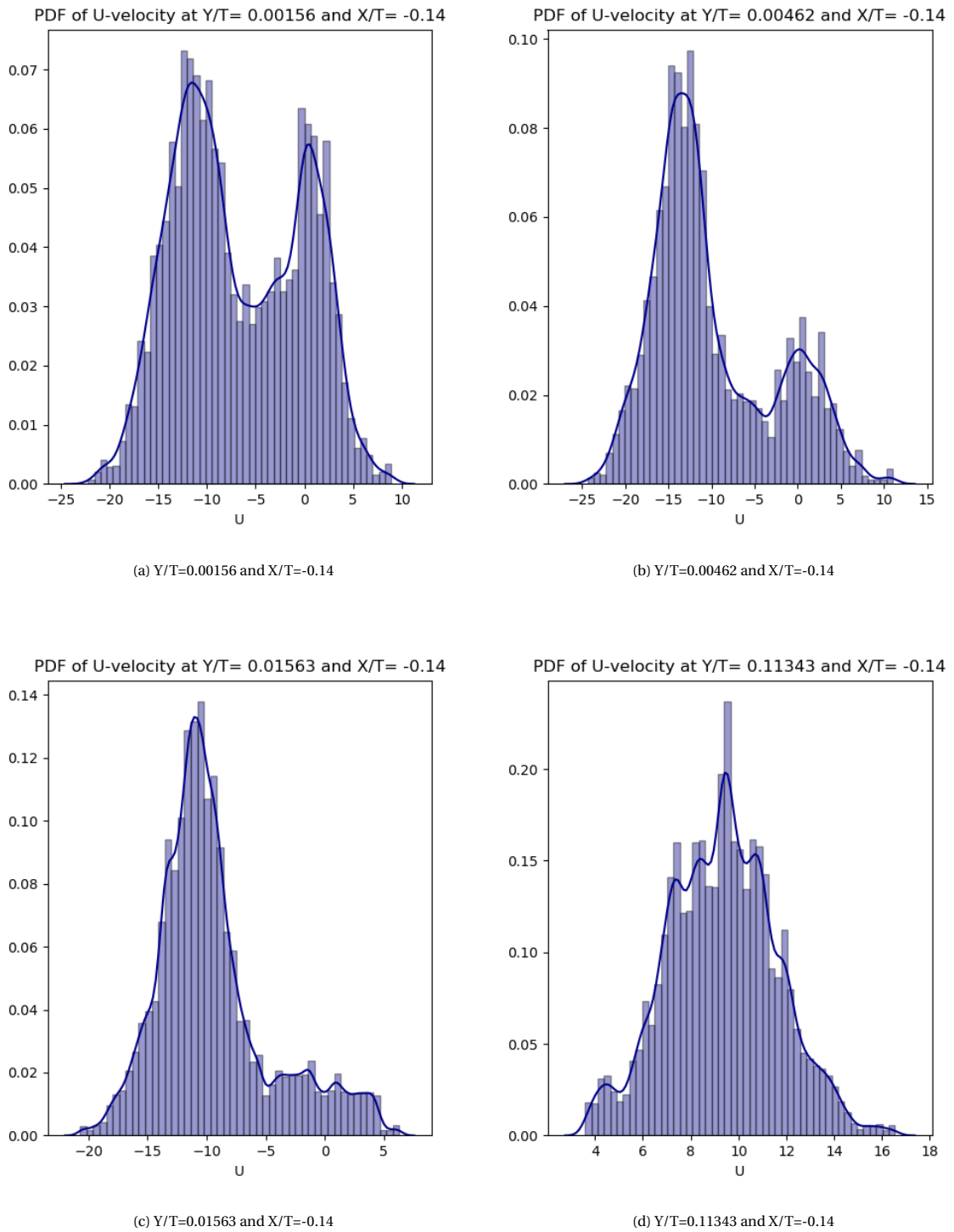
Figure 5.6: Probability density functions of the U-velocity component

5.1.6. Corner Vortex

The corner vortex located close to the wall and the leading edge of the wing, which is observed in Figure 5.4b and Figure 5.5b, is more closely displayed in Figure 5.7, which shows the time-averaged spanwise vorticity contour plots in the junction region for the LES simulation and RANS simulation. The spanwise vorticity is normalised by the thickness of the wing T and the freestream velocity U_∞. Furthermore, the velocity vector field visualises the secondary and tertiary corner vortex structures.

Figure 5.7a shows the results of the wall-resolved LES simulation. The main secondary corner vortex is located at X/T=-0.01 and Y/T=0.013 and is rotating counter-clockwise. Furthermore, two tertiary vortices can be observed in the figure: one counter-clockwise rotating vortex at X/T=-0.004 and Y/T=0.034 and a clockwise rotating vortex in the corner-region at X/T=-0.0015 and Y/T=0.0015. The tertiary vortex in the corner region is induced by the main secondary corner vortex and is therefore rotating in the opposite direction of the main corner vortex. The tertiary vortex located above the main corner vortex however, is created by the interaction of the boundary-layer flow which moves upward along the leading-edge above the corner region and the downward flow in the upper region of the figure located away from the leading-edge of the wing. Similar results have been observed by Ryu et al. [2016].

The results of the RANS simulation are presented in Figure 5.7b. The coarse RANS-simulation is not able to capture the secondary and tertiary vortices. There is a rotational motion observed in the velocity vector field at X/T=-0.007 and Y/T=0.007, however, the RANS-simulation clearly does not capture the strength nor the location of the main secondary corner vortex as well as the LES does. This can be explained due to the fact that the RANS-simulation is coarser than the LES-simulation in this region of the flow and is therefore not able to capture all the effects that occur near the wall and more importantly due to the fact that linear-eddy viscosity models are not good in predicting the anisotropy of the Reynolds stresses.

(a) Wall-resolved LES   (b) RANS
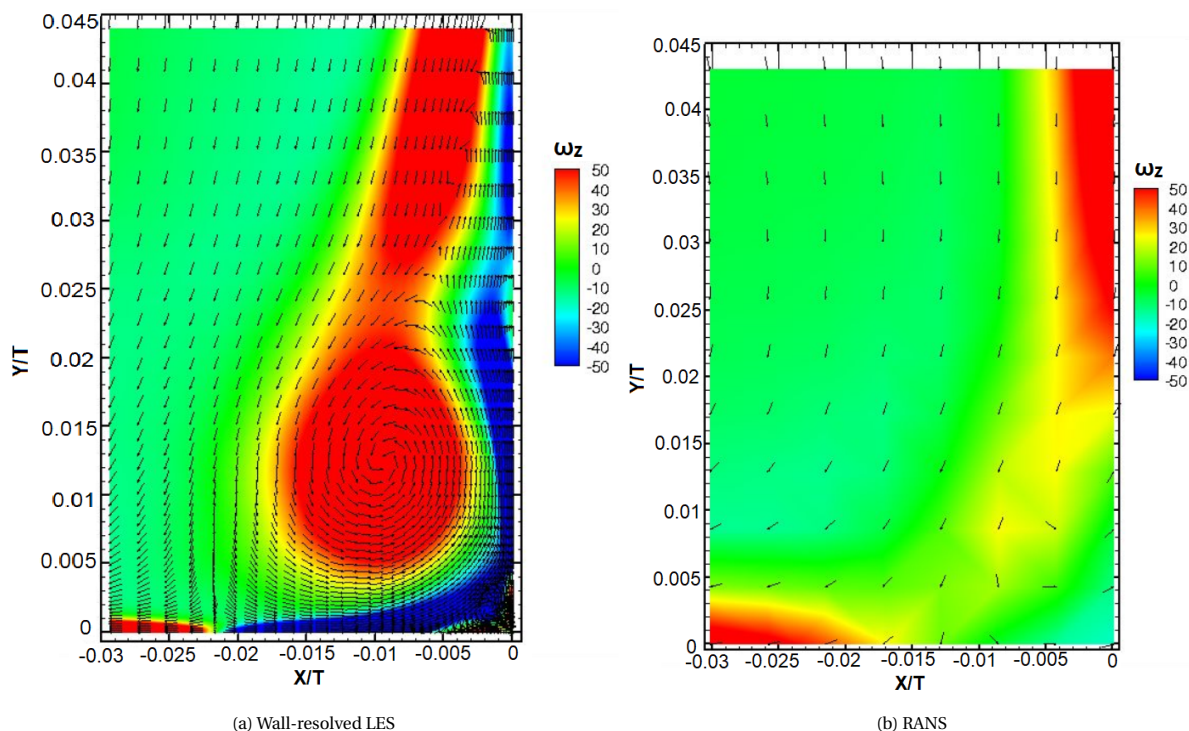
Figure 5.7: Contour plots of the time-averaged spanwise vorticity and velocity vectors which display the velocity field.

5.1.7. Mean Flow Visualisation on the Bottom Wall

Figure 5.9 shows the flow visualisation of the mean flow on the bottom wall of the domain. Figure 5.9a shows the experimental results of Ölcmen and Simpson [1995] by means of an oil flow visualisation. The line of separation starts upstream of the nose of the wing and moves along the side to the wing. This line of separation is generated due to the adverse pressure gradient and originates in the point of separation. Furthermore, the experimental results show the characteristic "fish tail"-structure at the trailing edge of the wing, which can be explained due the pressure recovery at the trailing edge which results in a reduction of the streamwise

velocity and the presence of the horseshoe vortex which induces spanwise velocities and therefore deflects the flow.

The visualisation of the mean flow on the bottom wall for the wall-resolved LES simulation is shown in Figure 5.9b. As background to the streamlines gives the pressure contour plots. The line of separation is predicted quite accurately by the wall-resolved LES simulation at a location of X/T=-0.5. Furthermore, the characteristic fish tail shape at the trailing edge of the wing is observed in the LES due to the presence of the horseshoe vortex and the pressure recovery near the trailing edge of the wing.

The mean flow visualisation on the bottom wall of the domain for the RANS-simulation is shown in Figure 5.9c. The figure shows that the line of separation is a bit farther upstream compared to the experimental results at a location of X/T=-0.6. Furthermore, at the trailing edge more flow separation is observed with respect to the experimental results. Also, the characteristic "fish tail"-structure is not observed in the RANS simulation results.

Furthermore, Devenport and Simpson [1990] observed a small region of secondary separation in the corner region between the wall and the wing by observing a reattachment line at the wall and a separation line on the wing at 0.025T from the corner in the symmetry plane. his secondary line of separation is observed in both simulations and is presented in Figure 5.8. In the results of the LES-simulation furthermore a tertiary line of separation is observed, corresponding to the tertiary corner vortex, which is not observed in the RANS results. Similar results were also observed by Ryu et al. [2016].

(a) Wall-resolved LES   (b) RANS
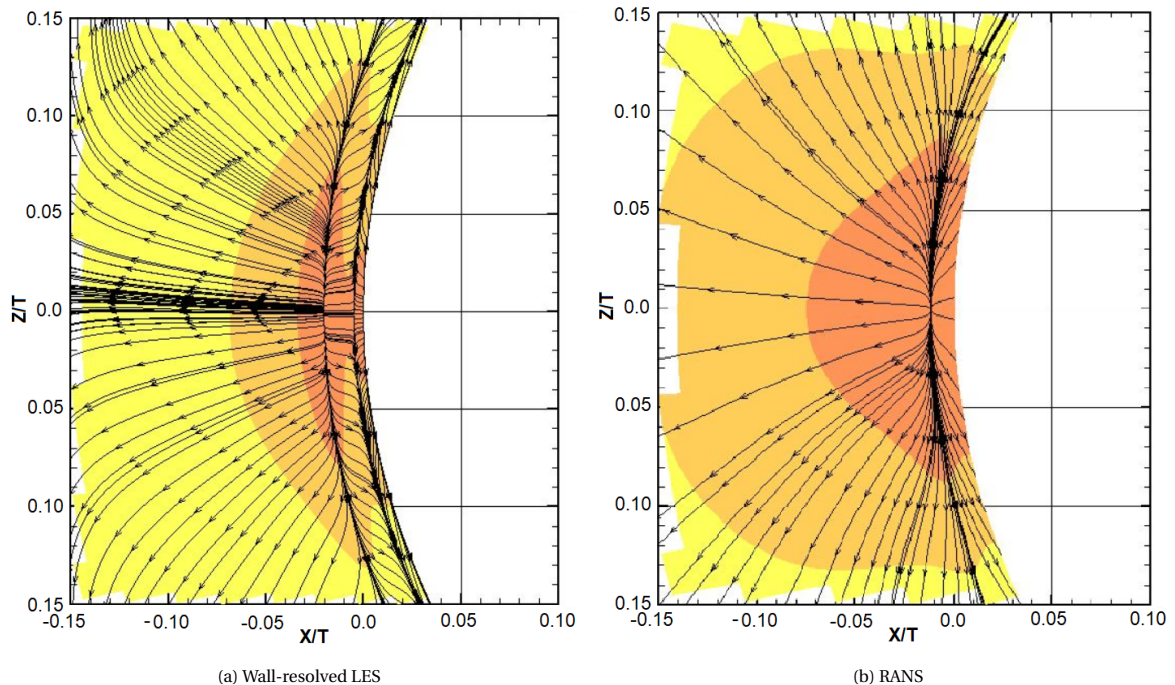
Figure 5.8: Secondary line of separation visualised by streamlines on the bottom wall.

Overall, the comparison of the results of the wall-resolved LES with experimental and numerical validation data show that the present wall-resolved LES is a good method to analyse these complex junction flows. The contours of spanwise vorticity and the turbulent kinetic energy show that the magnitude of these two variables and the characteristic C-shape of the turbulent kinetic energy peak is excellently captured by simulation. The location of these peaks however, is slightly more downstream with respect to the experimental data due to the sensitivity of the flow to the inlet boundary condition of the simulation. Furthermore, the boundary layer profiles predicted by the LES show good agreement with the results of Devenport and Simpson [1990] beside the regions of backflow close to the wall, which have been slightly underpredicted. Also, the pressure distribution contour plot shows good agreement with the experimental results. In the corner of the junction, secondary and tertiary corner vortices were captured by the wall-resolved LES, similar to those seen in the results of Ryu et al. [2016] and a mean flow visualisation on the bottom wall of the domain showed that the LES accurately captures the characteristic fish-tail structure at the trailing-edge of the wing and the line-of-separation upstream of the wing. Based on these results, it can be concluded that the wall-resolved

LES simulation is validated and can accurately capture the complex flow phenomena of the junction flow.

In contrast to the wall-resolved LES simulation, the RANS-simulation clearly does not perform as well when comparing the results to the experimental data. When comparing the vorticity contours, the peak vorticity is located upstream with respect to the experimental data. Similar to the vorticity, also the turbulent kinetic energy estimates are located more upstream and its magnitude is underpredicted. Also, the RANS-simulation was unable to capture the secondary and tertiary corner vortices. Furthermore, in the streamwise boundary layer profiles one can see that close to the wall, the amount of backflow is overpredicted while for the wall-normal boundary layer profiles at the three most upstream stations the RANS-simulation profiles have the opposite sign to the experimental results. In terms of pressure distribution, the results of the RANS-simulation are quite accurate. Finally, the characteristic fishtail-structure is not observed in the RANS-simulation when looking at the mean flow visualisation at the bottom wall of the domain. From this analysis, it can be concluded that the RANS-simulation is unable to capture all the complex flow physics in junction. This can be explained due to the limitations of RANS-methods, which are unable to correctly capture the Reynolds stress anisotropy due to the breakdown of the Boussinesq hypothesis. Therefore, in regions where the Boussinesq hypothesis is not valid, a significant improvement of RANS turbulence models can be achieved by using data-driven methods and high-fidelity data.
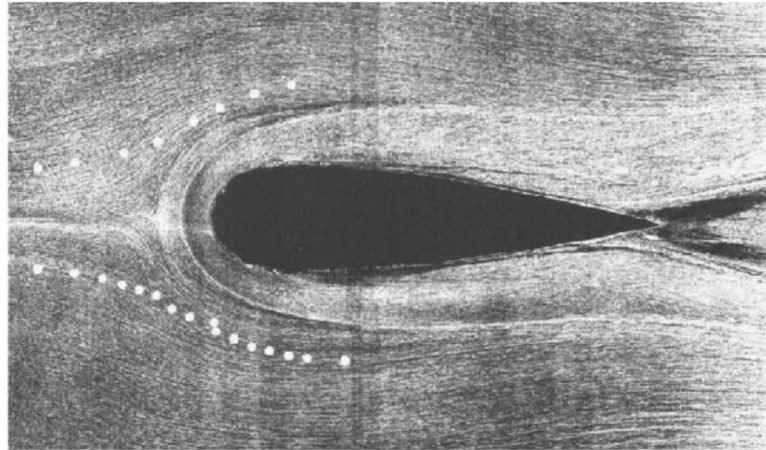
(a) Experimental results of Ölcmen and Simpson [1995].
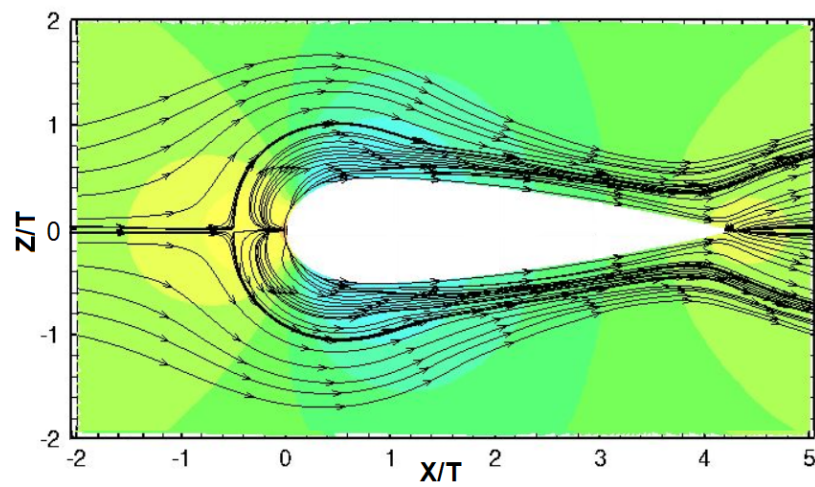
(b) Wall-resolved LES
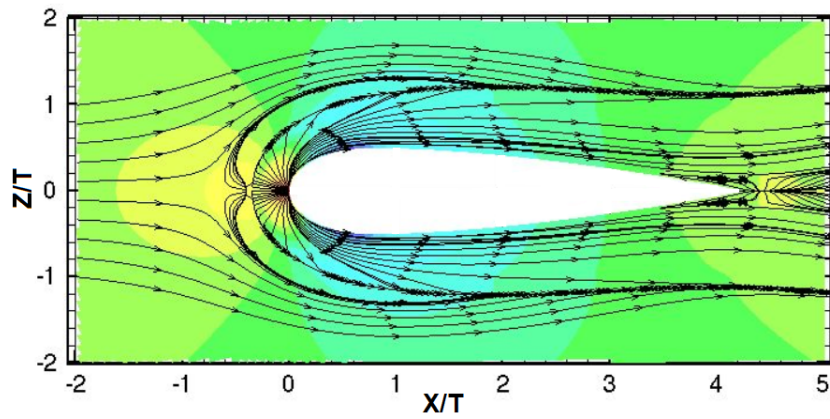
(c) RANS

Figure 5.9: Representation of the mean flow on the bottom wall. a) Oil flow visualisation on the bottom wall of the experiments of Ölcmen and Simpson [1995], and the mean flow visualisation by streamlines on the bottom wall of b) the wall-resolved LES simulation and c) the RANS-simulation.

5.2. Quantification of the Boussinesq Validity of the flow

In this section, the high-fidelity flow data of the wall-resolved LES simulation will be analysed to identify regions where the Boussinesq hypothesis would fail in junction flows and therefore yield inaccurate results in a RANS-simulation. In the Boussinesq hypothesis, the intrinsic assumption is made that the Reynolds stress anisotropy tensor is determined by the mean velocity gradients and the specific assumption is made that there is an alignment between the Reynolds stress anisotropy tensor and the mean rate-of-strain tensor S_{ij}, hence, the following equation should hold:

$$a_{ij} = \overline{u_i' u_j'} - \frac{2}{3} k \delta_{ij} \approx -2\nu_T S_{ij} \tag{5.1}$$

Many models rely on the Boussinesq hypothesis due to the fact that it gives acceptable results in simple shear flows (Pope [2000]) as these flows follow the specific assumption, but also, due to the fact that the eddy viscosity adds numerical stability to the model. However, in many engineering applications, the Boussinesq assumption is not valid in regions of the flow. To identify these regions, several approaches will be presented in this section of the report. In the regions where the Boussinesq hypothesis breaks down, data-driven turbulence models informed by the high-fidelity data have the potential to result into credible results which can be used in engineering applications to improve design procedures.

5.2.1. Deviation from Parallel Shear Flow

The first analysis that will be performed to indicate regions where the Boussinesq hypothesis might break down is by means of the marker function m as defined by Gorlé et al. [2014]:

$$m = |g_j s_j|. \tag{5.2}$$

The marker of Gorlé et al. [2014] measures the deviation from parallel shear flows. The reasoning behind the marker is that for parallel shear flows, where the gradients of mean quantities are almost perpendicular to the streamlines, linear-eddy viscosity models are giving reasonably accurate results. This is because of the specific assumption that there is an alignment between the Reynolds stress anisotropy tensor and the strain-rate tensor which is related through each other by means of the eddy viscosity. The specific assumption works reasonably well for simple parallel shear flows and the eddy viscosity is well defined, however, for more complex three-dimensional flows (such as junction flows) the Boussinesq hypothesis fails. To get a measure of the validity of the specific assumption in the Boussinesq hypothesis, Gorlé et al. [2014] defined the marker function m, which indicates the local deviation from parallel shear flow. In (5.2), g_j is the gradient of the streamline-aligned velocity and s_j is the unit velocity vector along the streamline. For perfect parallel shear flows, m is zero. However, as the angle between the gradients g_j and the direction of the streamline decreases, the value of m will increase. Furthermore, for a fixed angle between the gradients and the streamline, the marker function m will scale with the strain-rate tensor.

The marker function is applied to the wall-resolved LES simulation results, resulting in the results presented in Figure 5.10. As can be seen from Figure 5.10, at the location of the horseshoe vortex and at the location of the secondary and tertiary corner vortices the value of the marker m is high, which means a large deviation from parallel shear flow and therefore this is a region where the Boussinesq hypothesis breaks down. This is to be expected due to the high unsteady nature of the phenomenon and the three-dimensional effects. Furthermore, between Y/T=0.2 and Y/T=0.3 at X/T=-0.1 one can see the start of region with a high deviation of parallel shear flow. This region goes all the way up towards the top of the domain and is due to the interaction of the flow with the leading edge of the wing. Furthermore, it can be observed that when moving further upstream, away from the wing, the value of the marker function m reduces due to the fact that there is less interaction with the wing. All the way upstream at the inlet of the domain, the marker value of m approaches towards zero.

5.2.2. Implied Ideal Eddy Viscosity

The Boussinesq hypothesis implies that there is a linear relationship between the Reynolds stress anisotropy tensor a_{ij} and the mean strain-rate tensor S_{ij} through the positive scalar coefficient, ν_T, the eddy viscosity. However, in regions of quick changing gradients, the assumption that the eddy viscosity is strictly positive may not be valid. If the assumption of strictly positive eddy viscosity breaks down, it means that the RANS-turbulence models are not able of capturing the complex junction flows, which necessitates the need of different methods to capture these complex flows.
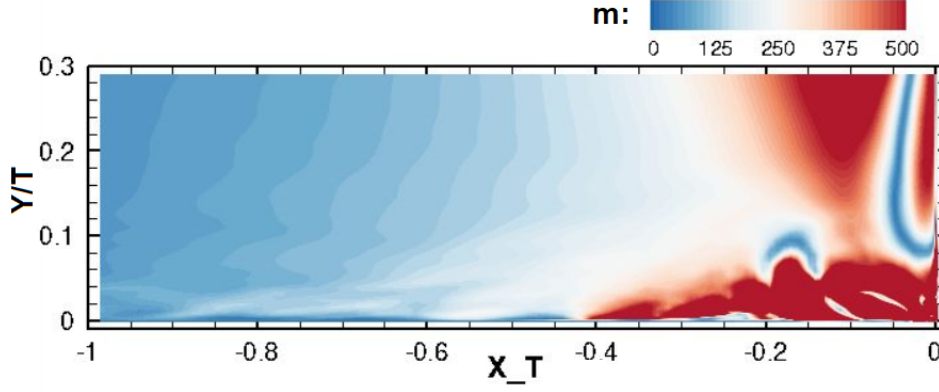
Figure 5.10: Contour plot of marker function "m", which shows the deviation of parallel shear flow.

Given the high-fidelity LES data, the ideal/perfect eddy viscosity which maps the mean strain-rate tensor S_{ij} on the Reynolds stress anisotropy tensor a_{ij} was determined by rewriting (5.1) into:

$$\nu_T = -\frac{1}{2} S_{ij}^T a_{ij}. \tag{5.3}$$

The ideal eddy viscosity based on the simulation results of the wall-resolved LES are presented in Figure 5.11. Figure 5.11a shows a binary contour plot of the ideal/perfect eddy viscosity and the blue regions indicate the regions where the ideal eddy viscosity based on the wall-resolved LES data becomes negative. This means that the assumptions made in the turbulent-viscosity hypothesis would break down in these regions of negative eddy viscosity.

Furthermore, one can observe in Figure 5.11b the contour plot in the junction region of the ideal eddy viscosity. Due to the relationship between the Reynolds stress anisotropy and the mean strain-rate tensor by the eddy viscosity, the eddy viscosity can also be seen as a factor which defines alignment. It can be seen from Figure 5.11b, higher values of the ideal eddy viscosity are required to map the mean strain-rate tensor to the Reynolds stress anisotropy tensor at the location of the horseshoe vortex. Since the specific assumption in the Boussinesq hypothesis assumes an alignment of the Reynolds stress tensor and the mean strain-rate tensor, for high values of the implied ideal eddy-viscosity the Boussinesq hypothesis might not be valid.

5.2.3. Alignment of the Reynolds anisotropy tensor a_{ij} and the mean strain-rate tensor S_{ij}

The assumptions made in the Boussinesq hypothesis imply that the Reynolds stress anisotropy tensor a_{ij} is linearly related to the mean strain-rate tensor S_{ij}. Pope [2000] noted that even for the simplest shear flows, this can be incorrect due to the fact that for a turbulent shear flow, the normal strain-rates are zero, however, the normal Reynolds stresses are significantly different from one another. He also proposed the different perspective that the principal axis of a_{ij} are misaligned with the principal axis of S_{ij}. Several authors introduced methods to capture the alignment of the principal axis of the two tensors.

Schmitt [2007] was the first to propose a measure of alignment to indicate the validity of the Boussinesq hypothesis. The proportionality between the Reynolds stress anisotropy and the mean strain-rate can be tested easily if one has the two tensors R and S_{ij}, which are readily available in the data of the wall-resolved LES simulation. Schmitt [2007] introduced an indicator ρ_{RS} which is based on the inner product of the two tensors and resembles the cosine between the two axis of the tensors. The indicator ρ_{RS} can vary between 1 and 0, where a value of 1 indicates perfectly aligned tensors and a value of 0 indicates perpendicular tensors. Schmitt [2007] suggested that for ρ_{RS} larger than 0.86, the alignment of the two tensors is approximately verified. This corresponds to an angle between the principal axis of smaller than $\frac{\pi}{6}$.

Akolekar et al. [2019] used a similar alignment indicator to Schmitt [2007]. The indicator of Akolekar et al. [2019], γ, ranges from -1 to 1 and measures the orthogonality of the measured anisotropy tensors and is therefore a useful indicator of the Boussinesq approximation. Similar to Akolekar et al. [2019], a value of 1 indicates perfect alignment of the tensors while a value of 0 indicates that the tensors are completely orthogonal. A value of -1 means that the the alignment is predicted in the opposite direction.

The method employed in the present study will be similar to those of Akolekar et al. [2019] and Schmitt

(a) Binary contour of the ideal eddy viscosity. Blue regions indicate negative eddy viscosity while red regions indicate positive eddy viscosity.

(b) Contour plot of the ideal eddy viscosity.
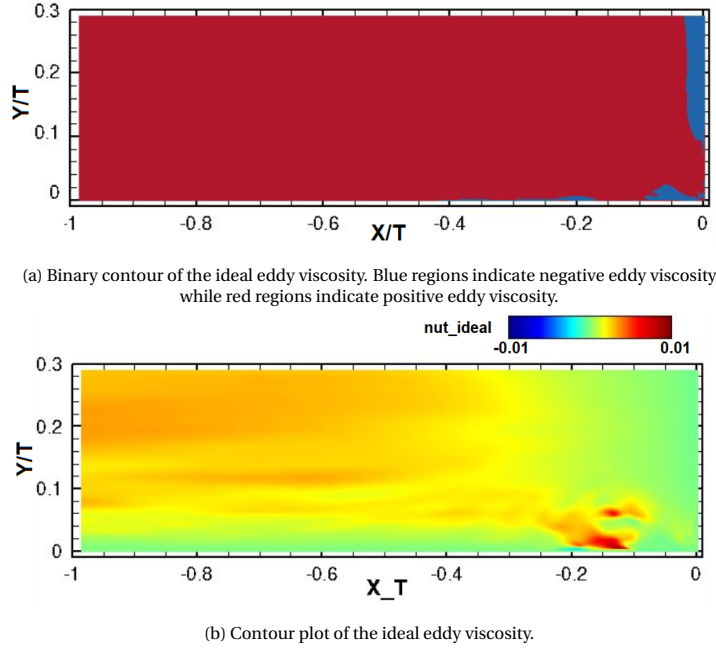
Figure 5.11: Contour plots of the ideal/perfect eddy viscosity ν_T based on the wall-resolved LES data. a) Binary contour plot and b) Contour plot of the ideal eddy viscosity.
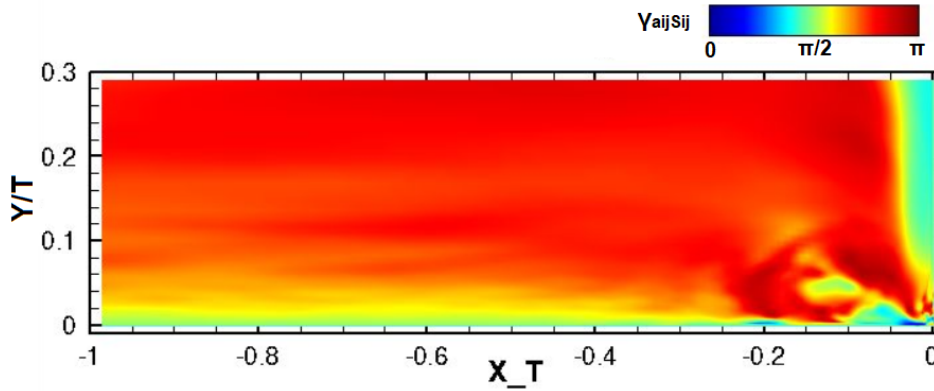
Figure 5.12: Contour plot of the angle of alignment $\gamma_{a_{ij}S_{ij}}$ in the region of the junction.

[2007] and will be determined by means of the methodology proposed by Tape and Tape [2012], which describes how to determine the smallest angle required to rotate the principal axes from one tensor to the principal axes of another tensor. Figure 5.12 shows a contour plot of the required angle to align the principal axis of the two tensors named $\gamma_{a_{ij}S_{ij}}$. The value of the angle of alignment $\gamma_{a_{ij}S_{ij}}$ ranges between 0 and π, where 0 means complete alignment between the two tensors, $\frac{\pi}{2}$ indicates complete orthogonality of the two tensors and π indicates that the alignment is predicted with the opposite orientation. Similar to Schmitt [2007], for values of the angle of alignment $\gamma_{a_{ij}S_{ij}} < \frac{\pi}{6}$ the two tensors are considered aligned. As can be observed from Figure 5.12 at almost every location of the contour plot the value of the angle of alignment exceeds the value of $\frac{\pi}{6}$, which shows that Boussinesq hypothesis is not valid in the region of the junction and improvements can be made of the RANS-predictions by means of data-driven turbulence modelling. More specifically, high angles of $\gamma_{a_{ij}S_{ij}}$ are observed at the location of the horseshoe vortex and the location of the corner vortices. Another interesting observation is that the regions where the angle of alignment is close to $\frac{\pi}{2}$, indicating complete orthogonality of the two tensors, is the region where the ideal eddy viscosity is negative (see Figure 5.11a), which confirms that the Boussinesq hypothesis is not valid in this region of the flow.

(a) True TKE production based on the Reynolds stress tensor.

(b) Boussinesq TKE production based on the ideal eddy viscosity.

(c) Difference between the true TKE production and the Boussinesq TKE production.
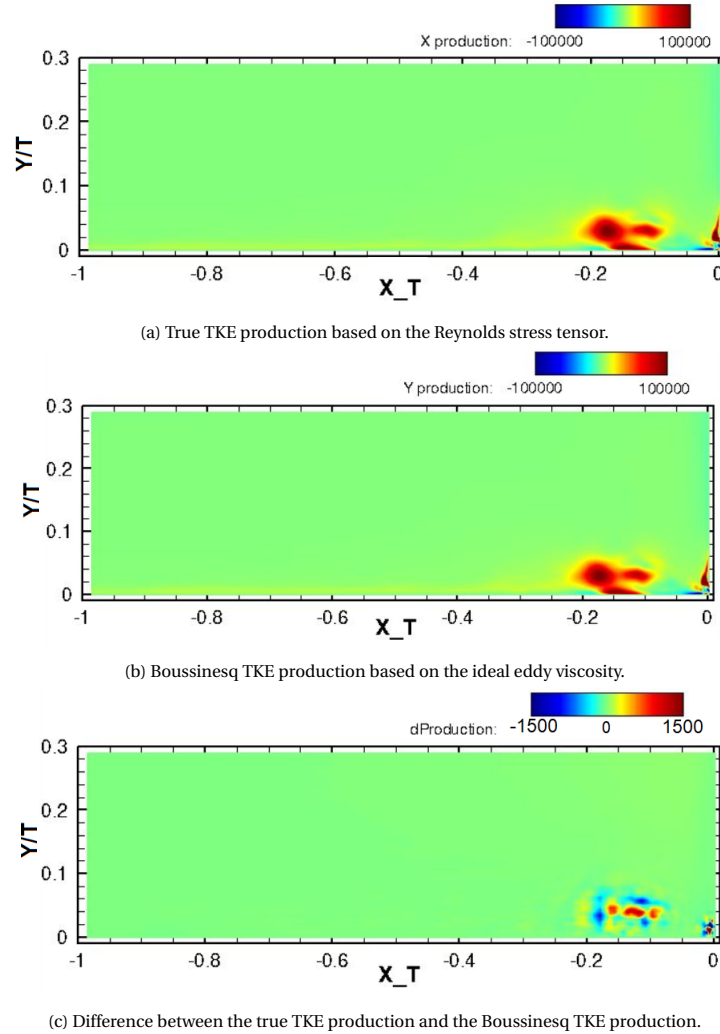
Figure 5.13: Contour plots of the turbulent kinetic energy production.

5.2.4. Turbulent Kinetic Energy Production

In order to check the effect of the Boussinesq hypothesis on the production of turbulent kinetic energy, an analysis of the turbulent kinetic energy production based on the high-fidelity data of the wall-resolved LES simulation was performed. The production term was computed based on the k-equation. Both the exact production based on the Reynolds stress tensor and the Boussinesq production based on the ideal eddy viscosity have been determined and are shown in Figure 5.13. Furthermore, also the difference between the two production terms is plotted in Figure 5.13. As can be observed in Figure 5.13, the turbulent kinetic energy production looks very similar for the true TKE production based on the Reynolds stress tensor and the Boussinesq TKE production. As can be expected, most of the turbulent kinetic energy production is located at the location of the horseshoe vortex and the location of the corner vortices. When looking at the difference between the two production contours in Figure 5.13c, once can observe that the largest differences are observed at the locations where also the most turbulent kinetic energy is produced. However, it should be noted that these difference are only +-1.5% of the total turbulent kinetic energy production plotted in Figure 5.13a and Figure 5.13b. Furthermore, it seems like that the positive and negative differences would approximately cancel each other out. Hence, the difference in turbulent kinetic energy production due to the Boussinesq hypothesis given an ideal eddy viscosity is small.

Based on the results of the analyses above, one can conclude that in the region close to the junction the Boussinesq hypothesis is breaking down. Most notably the hypothesis breaks down at the location of the junction vortex and the location of the corner vortices. This phenomenon in the region of the junction is

explained by the adverse pressure gradient, affecting the velocity gradient tensor and as a result the linear relationship between the Reynolds stress tensor and the mean strain-rate tensor is no longer accurate. This is also observed in the contourplots showing the angle of alignment in which almost all angles are larger than the threshold of $\frac{\pi}{6}$, indicating the breakdown of the specific assumption in the Boussinesq hypothesis. Furthermore, large deviations from parallel shear flow were shown by the marker m in the region close to the junction. However, only a difference of +-1.5% was observed in turbulent kinetic energy production when comparing the TKE production based on the true Reynolds stress tensor to the TKE production based on the ideal eddy viscosity, which is relatively small. The breakdown of the Boussinesq hypothesis explains why the RANS-simulation was not able to give an accurate prediction of the secondary flow structures in the junction region. Due to these limitations, employing a data-driven approach to turbulence modelling could provide significant improvements with respect to conventional turbulence models.

6

Conclusions & Recommendations

Junction flows are encountered in many engineering applications, such as the junctions present in aircraft. According to Filippone [2000], approximately 5% of the total drag of subsonic transport aircraft can be allocated to the presence of junctions. It is therefore important for aircraft manufacturers to understand the behaviour and be able to predict the behaviour of these complex flows. Several numerical methods exist to analyse such flows of which Reynolds-Averaged Navier-Stokes (RANS) methods are most commonly used in engineering applications due to its relatively cheap computational cost. However, the turbulence models which are used to model the turbulent effects are unable to accurately model these complex flow phenomena. An alternative which is able to capture these complex flow phenomena, is to perform a large eddy simulation. However, the computational cost of these simulations is too high to be used for engineering applications. With the increase of computational power and availability of high-fidelity data sets, research has been focused on informing turbulence models with data to enhance and improve the performance of these turbulence models by means of machine learning. Due to the limited amount of available high-fidelity junction flow data, it is not possible to enhance turbulence models for junction flows by means of a data-driven turbulence modelling approach. Therefore, the objective of this research was formed to close this gap and is given as follows:

> "*The objective of the research is to generate high-fidelity junction flow data, to be used in a data-driven turbulence modelling approach to improve the accuracy of RANS simulations in junction flows, by performing a wall-resolved Large Eddy Simulation of the wing-body junction originally studied experimentally by Devenport and Simpson [1990].*".

The conclusions drawn from the present research and recommendations for future research will be presented in this chapter.

6.1. Conclusions
In the present study a detailed wall-resolved large eddy simulation of the wing-body junction which was originally first analysed experimentally by Devenport and Simpson [1990] has been presented. The wall-resolved LES was initialised by a turbulent channel flow precursor-simulation and the WALE subgrid-scale model was used. The LES results were compared to validation data to validate whether the simulation captured all the flow physics correctly. The parameters used for the validation were the upstream boundary layer profiles, the mean surface pressure coefficient, mean spanwise vorticity in the symmetry plane and the mean turbulent kinetic energy in the symmetry plane.

Overall, the comparison of the LES results with the validation data shows good agreement and therefore validates the methodology. The contours of the mean spanwise vorticity and the mean turbulent kinetic energy in the symmetry plane show that the magnitude of these two variables and the characteristic C-shape of the turbulent kinetic energy peak is excellently captured by the wall-resolved LES simulation. The location of these peaks, which corresponds with the location of the horseshoe vortex, is located slightly downstream with respect to the validation data. This can be explained by the sensitivity of the flow to the inlet boundary condition and the fact that the turbulent channel flow precursor needs a larger development region at the beginning of the domain to transform into a fully developed flat plate boundary layer. Furthermore, a secondary

vortex structure in the corner region of the junction flow was observed in the vorticity and turbulent kinetic energy contours plots. Also, a comparison of the boundary layer profiles upstream of the wing in the symmetry plane was made. The boundary layer profiles predicted by the LES show overall good agreement with the results of Devenport and Simpson [1990] beside the regions of backflow close to the bottom-wall, which have been slightly underpredicted. Furthermore, the mean surface pressure coefficient contour plot shows good agreement to the experimental results, with the only difference being that the location of low pressure at the wing is located slightly upstream for the LES with respect to the validation data. The wall-resolved LES also captures the characteristic bimodal dynamics of the horseshoe vortex by having a double peaked probability density function at the location of the horseshoe vortex, indicating the zero-flow mode and the back-flow mode of the horseshoe vortex system, similar to the double-peaked probability density function observed by Devenport and Simpson [1990]. In the corner of the junction, secondary and tertiary vortices were captured by the wall-resolved LES, similar to those observed by Ryu et al. [2016] and a mean flow visualisation on the bottom wall of the domain showed that the LES captures the characteristic fish-tail structure at the trailing edge of the wing and the line-of-separation upstream of the wing. Based on these results, it can be concluded that the wall-resolved LES accurately captures the flow physics of the junction flow and therefore is validated.

As the present study is a follow-up based on a recommendation of the research of Srikumar [2019], a comparison was made between the results of the wall-resolved LES and the wall-modelled LES of Srikumar [2019]. The wall-modelled LES captures the location and magnitude of the mean spanwise vorticity and also has the characteristic lifted elliptic shape. However, the wall-modelled LES does not capture the trail of positive and negative vorticity close to the leading-edge of the wing. This can be explained by the fact that the wall-modelled LES of Srikumar [2019] has not enough cells in the region close to the wall to capture the highly localised vorticity which the wall-resolved LES does manage to capture. For the same reason, the secondary and tertiary corner vortices are not observed in the simulation of Srikumar [2019]. When comparing the mean turbulent kinetic energy peak of the wall-modelled LES, it is observed that with respect to the validation data and the wall-resolved LES, the turbulent kinetic energy peak is about 40% of the turbulent kinetic energy peak observed in the validation data and located slightly upstream with respect to the validation data. Also, the characteristic C-shape is not observed. Based on these results, it can be concluded that the wall-resolved LES in the present study is an improvement with respect to the wall-modelled LES of Srikumar [2019].

Also, a comparison to a coarse-grid RANS simulation was made. In contrast to the wall-resolved LES simulation, the RANS-simulation does not compare as well to the validation data. When making a comparison of the mean spanwise vorticity and mean turbulent kinetic energy contour plots in the symmetry plane upstream of the wing, the mean spanwise vorticity peak and the mean turbulent kinetic energy peak, which indicates the location of the horseshoe vortex, are located upstream with respect to the validation data. Furthermore, the magnitude of the turbulent kinetic energy is approximately half that of the wall-resolved LES while the vorticity contour of the RANS-simulation shows a smooth blob of negative vorticity instead of the characteristic elliptic lifted flow structure. Furthermore, the RANS-simulation was unable to capture the secondary and tertiary corner vortices. The streamwise boundary layer profiles show that close to the bottom wall, the RANS-simulation overpredicts the amount of backflow while for the wall-normal boundary layer profiles the three most upstream boundary layer profiles have the opposite sign of the experimental data. However, the pressure distribution around the wing are quite accurate. Finally, the characteristic fish-tail structure is not observed in the RANS-simulation. From the results above, it can be concluded that a RANS-simulation is unable to accurately capture the complex flow physics in the region of the junction. This can be explained by the limitations of the RANS-methods, which are unable to capture the Reynolds stress anisotropy due to the breakdown of the Boussinesq hypothesis. Therefore, in the regions where the Boussinesq hypothesis is not valid, a significant improvement of RANS turbulence models can be achieved by using data-driven methods to improve and inform turbulence models with high-fidelity data.

Finally, an analysis on the high-fidelity data was performed to indicate regions where the Boussinesq hypothesis breaks down. First of all, this was shown by local large deviations from parallel shear flow by the marker m of Gorlé et al. [2014] in the region close to the junction. Furthermore, the breakdown of the Boussinesq hypothesis is also observed in the contourplot which shows the angle of alignment between the Reynolds stress anisotropy tensor and the mean strain-rate tensor. The angle of alignment was for almost all angles larger than the threshold of $\frac{\pi}{6}$, which indicates the breakdown of the specific assumption in the Boussinesq hypothesis. Also, an estimate of the ideal implied eddy-viscosity was made based on the wall-resolved large

eddy simulation. In this mapping, negative values for the "ideal" eddy-viscosity were observed, which indicates that the Boussinesq hypothesis will not be valid in those regions. Finally, a comparison was made between the true turbulent kinetic energy production and the turbulent kinetic energy production based on the implied ideal eddy-viscosity. However, for this analysis, only a difference of +-1.5% was observed in turbulent kinetic energy production, which is relatively small. From these analyses, it can be concluded that in the region close the junction, where the complex three-dimensional flows are located, the Boussinesq hypothesis breaks down. Most notably the hypothesis breaks down at the location of the junction vortex and the location of the corner vortices. This breakdown of the Boussinesq hypothesis in the region of the junction is explained by the adverse pressure gradient, which affects the velocity gradient tensor and as a result the linear relationship between the Reynolds stress tensor and the mean strain-rate tensor is no longer accurate.

The breakdown of the Boussinesq hypothesis explains why the RANS-simulation was not able to give an accurate prediction of the secondary flow structures in the junction region. Due to the limitations of RANS simulations and the availability of high-fidelity LES data of the present study, significant improvements of junction flow RANS-simulations can potentially be achieved by implementing a data-driven approach to turbulence modelling of junction flows.

6.2. Recommendations for Future Research

Based on the present research, a set of recommendations can also be made for future research:

- As mentioned throughout the report, the wall-resolved LES predicted the location of the horseshoe vortex system slightly closer to the wall with respect to the validation data. This can be explained by the inlet boundary condition using precursor data from a turbulent channel flow (TCF), which results in a discontinuity at the inlet between the precursor data and the freestream velocity. Due to the sensitivity of the simulation to the inlet boundary condition, a longer development region for the turbulent boundary layer to develop is recommended to possibly mitigate the effect of the TCF precursor.

- Furthermore, for future research of junction flows, it is recommended to perform a wall-resolved LES of the novel wing-body junction: the anti-fairing to get a better understanding of the working mechanism and the flow characteristics of the novel wing-body junction.

- Finally, given the high-fidelity data of the wall-resolved LES simulation, a data-driven turbulence modelling approach could be implemented to improve the performance of RANS-simulations in junction flows.

Bibliography

A. Ahmed and M. Javed Khan. Effect of sweep on wing-body juncture flow. In *33rd Aerospace Sciences Meeting and Exhibit*, 1995.

H. D. Akolekar, J. Weatheritt, N. Hutchins, R. D. Sandberg, G. Laskowski, and V. Michelassi. Development and Use of Machine-Learnt Algebraic Reynolds Stress Models for Enhanced Prediction of Wake Mixing in Low-Pressure Turbines. *Journal of Turbomachinery*, 141(4), 03 2019. ISSN 0889-504X. doi:10.1115/1.4041753.

N. Alin and C. Fureby. Large eddy simulation of junction vortex flows. 2008. ISBN 978-1-62410-128-1. doi:10.2514/6.2008-668.

D.D. Apsley and M.A. Leschziner. Investigation of advanced turbulence models for the flow in a generic wing-body junction. *Flow, Turbulence and Combustion*, 67(1):25–55, 9 2001. ISSN 1573-1987. doi:10.1023/A:1013598401276. URL https://doi.org/10.1023/A:1013598401276.

C.J. Baker. The laminar horseshoe vortex. *Journal of Fluid Mechanics*, 95(2):347–367, 1979. doi:10.1017/S0022112079001506.

C.J. Baker. The turbulent horseshoe vortex. *Journal of Wind Engineering and Industrial Aerodynamics*, 6(1-2): 9–23, 1980. doi:10.1016/0167-6105(80)90018-5.

T. J. Barber. An investigation of strut-wall intersection losses. *Journal of Aircraft*, 15(10):676–681, 1978. doi:10.2514/3.58427.

D. Barberis, P. Molton, and T. Malaterre. Control of 3d turbulent boundary layer separation caused by a wing–body junction. *Experimental Thermal and Fluid Science*, 16(1):54 – 63, 1998. ISSN 0894-1777. doi:https://doi.org/10.1016/S0894-1777(97)10012-7.

Z. Belligoli, A.J. Koers, R.P. Dwight, and G. Eitelberg. Using an anti-fairing to reduce drag at wing/body junctions. *AIAA Journal*, 57(4):1468–1480, 2019. doi:10.2514/1.J057481.

L. Bernstein and S. Hamid. On the effect of a strake-like junction fillet on the lift and drag of a wing. *The Aeronautical Journal (1968)*, 100(992):39–52, 1996. doi:10.1017/S0001924000027275.

P Bradshaw. Turbulent secondary flows. *Annual Review of Fluid Mechanics*, 19(1):53–74, 1987. doi:10.1146/annurev.fl.19.010187.000413.

J. Brezillon and R. Dwight. Applications of a discrete viscous adjoint method for aerodynamic shape optimisation of 3d configurations. *CEAS Aeronautical Journal*, 3, 10 2011. doi:10.1007/s13272-011-0038-0.

S.H. Cheung, T.A. Oliver, E.E. Prudencio, S. Prudhomme, and R.D. Moser. Bayesian uncertainty analysis with applications to turbulence modeling. *Reliability Engineering & System Safety*, 96(9):1137 – 1149, 2011. ISSN 0951-8320. doi:https://doi.org/10.1016/j.ress.2010.09.013. Quantification of Margins and Uncertainties.

J.-J. Cho and K.-S. Kim. Controlling the horseshoe vortex by leading-edge chamfer at a generic wing-body junction. *Journal of the Korean Society of Propulsion Engineers*, 13, 01 2009a.

J.-J. Cho and K.-S. Kim. Controlling the horseshoe vortex by the leading-edge fence at a generic wing-body junction. *Journal of the Korean Society for Aeronautical & Space Sciences*, 37:336–343, 01 2009b. doi:10.5139/JKSAS.2009.37.4.336.

H. Choi and P. Moin. Grid-point requirements for large eddy simulation: Chapman's estimates revisited. *Physics of Fluids*, 24(1):011702, 2012. doi:10.1063/1.3676783.

J. Dandois. Improvement of corner flow prediction using the quadratic constitutive relation. *AIAA Journal*, 52(12):2795–2806, 2014. doi:10.2514/1.J052976.

W.J. Devenport and R.L. Simpson. Time-dependent and time-averaged turbulence structure near the nose of a wing-body junction. *Journal of Fluid Mechanics*, 210(23):23–55, 1990. doi:10.1017/S0022112090001215.

W.J. Devenport, N.K. Agarwal, M.B. Dewitz, R.L. Simpson, and K. Poddar. Effects of a fillet on the flow past a wing-body junction. *AIAA Journal*, 28(12):2017–2024, 1990. doi:10.2514/3.10517.

W.J. Devenport, R.L. Simpson, M.B. Dewitz, and N.K. Agarwal. Effects of a leading-edge fillet on the flow past an appendage-body junction. *AIAA Journal*, 30(9):2177–2183, 1992a. doi:10.2514/3.11201.

W.J. Devenport, R.L. Simpson, M.B. Dewitz, and N.K. Agarwal. Effects of a leading-edge fillet on the flow past an appendage-body junction. *AIAA Journal*, 30(9):2177–2183, 1992b. doi:10.2514/3.11201.

Nitin S. Dhamankar, Gregory A. Blaisdell, and Anastasios S. Lyrintzis. Overview of turbulent inflow boundary conditions for large-eddy simulations. *AIAA Journal*, 56(4):1317–1334, 2018. doi:10.2514/1.J055528.

S.C. Dickinson. Experimental investigation of appendage-flat plate junction flow. volume 2. elliptical nose appendage data base. *Final Report Naval Ship Research and Development Center, Bethesda, MD.*, 2, 11 1986.

F. Ducros, F. Nicoud, and T. Poinsot. Wall-adapting local eddy-viscosity models for simulations in complex geometries. *Numerical Methods for Fluid Dynamics VI*, pages 293–299, 01 1998.

Karthik Duraisamy, Gianluca Iaccarino, and Heng Xiao. Turbulence modeling in the age of data. *Annual Review of Fluid Mechanics*, 51(1):357–377, 2019. doi:10.1146/annurev-fluid-010518-040547.

W.N. Edeling, P. Cinnella, and R.P. Dwight. Predictive rans simulations via bayesian model-scenario averaging. *Journal of Computational Physics*, 275:65 – 91, 2014. doi:https://doi.org/10.1016/j.jcp.2014.06.052.

A. Filippone. Data and performances of selected aircraft and rotorcraft. *Progress in Aerospace Sciences*, 36(8): 629 – 654, 2000. ISSN 0376-0421. doi:https://doi.org/10.1016/S0376-0421(00)00011-7.

J.L. Fleming, R.L. Simpson, and W.J. Devenport. An experimental study of a turbulent wing-body junction and wake flow. Master's thesis, Virginia Polytechnic Institute and State University, Virginia Tech, 7 1991.

J.L. Fleming, R.L. Simpson, J.E. Cowling, and W.J. Devenport. An experimental study of a turbulent wing-body junction and wake flow. *Experiments in Fluids: Experimental Methods and their Applications to Fluid Flow*, 14(5):366–378, 1993. doi:10.1007/BF00189496.

S. Fu, Z. Xiao, H. Chen, Y. Zhang, and J. Huang. Simulation of wing-body junction flows with hybrid rans/les methods. *International Journal of Heat and Fluid Flow*, 28(6):1379–1390, 2007. doi:10.1016/j.ijheatfluidflow.2007.05.007.

F. Gand, V. Brunet, and S. Deck. A combined experimental, rans and les investigation of a wing body junction flow. In *40th AIAA Fluid Dynamics Conference*, 2010a.

F. Gand, S. Deck, V. Brunet, and P. Sagaut. Flow dynamics past a simplified wing body junction. *Physics of Fluids*, 22(11), 2010b. doi:10.1063/1.3500697.

M. Germano, U. Piomelli, P. Moin, and W. H. Cabot. A dynamic subgrid-scale eddy viscosity model. *Physics of Fluids A: Fluid Dynamics*, 3(7):1760–1765, 1991. doi:10.1063/1.857955.

F.B. Gessner. The origin of secondary flow in turbulent flow along a corner. *Journal of Fluid Mechanics*, 58(1): 1–25, 1973. doi:10.1017/S0022112073002090.

C. Gorlé, J. Larsson, M. Emory, and G. Iaccarino. The deviation from parallel shear flow as an indicator of linear eddy-viscosity model inaccuracy. *Physics of Fluids*, 26(5):051702, 2014. doi:10.1063/1.4876577.

B.E. Green and J.L. Whitesides. Method for designing leading-edge fillets to eliminate flow separation. *Journal of Aircraft*, 40(2):282–289, 2003. doi:10.2514/2.3121.

S. Hickel, N.A. Adams, and J.A. Domaradzki. An adaptive local deconvolution method for implicit les. *Journal of Computational Physics*, 213(1):413 – 436, 2006. ISSN 0021-9991. doi:https://doi.org/10.1016/j.jcp.2005.08.017.

R. Huang, C.M. Hsu, and C. Chen. Effects of an upstream tetrahedron on the circular cylinder–flat plate juncture flow. *Experiments in Fluids*, 56, 07 2015. doi:10.1007/s00348-015-2020-9.

M. Johnson, K. Ravindra, and R. Andres. *Comparative study of the elimination of the wing fuselage junction vortex by boundary layer suction and blowing.* doi:10.2514/6.1994-293.

A. Keating, U. Piomelli, E. Balaras, and H. Kaltenbach. A priori and a posteriori tests of inflow conditions for large-eddy simulation. *Physics of Fluids*, 16(12):4696–4712, 2004. doi:10.1063/1.1811672.

M.A. Kegerise, D. Neuhart, J. Hannon, and C.L. Rumsey. *An Experimental Investigation of a Wing-Fuselage Junction Model in the NASA Langley 14- by 22-Foot Subsonic Wind Tunnel.* doi:10.2514/6.2019-0077.

G. Kirkil, S.G. Constantinescu, and R. Ettema. Coherent structures in the flow field around a circular cylinder with scour hole. *Journal of Hydraulic Engineering*, 134(5):572–587, 2008. doi:10.1061/(ASCE)0733-9429(2008)134:5(572).

L. Kubendran, A. Bar-Sever, and W. Harvey. *Flow control in a wing/fuselage-type juncture.* doi:10.2514/6.1988-614.

L. R. Kubendran, H. Mcmahon, and J. E. Hubbartt. Interference drag in a simulated wing-fuselage juncture. Technical report, NASA, Washington, United States, 7 1984.

L. R. Kubendran, H. M. McMahon, and J. E. Hubbartt. Turbulent flow around a wing/fuselage-type juncture. *AIAA Journal*, 24(9):1447–1452, 1986. doi:10.2514/3.9464.

Myoungkyu Lee and Robert D. Moser. Direct numerical simulation of turbulent channel flow up to $Re_\tau \approx 5200$. *Journal of Fluid Mechanics*, 774:395–415, 2015. doi:10.1017/jfm.2015.268.

J. Ling and J. Templeton. Evaluation of machine learning algorithms for prediction of regions of high reynolds averaged navier stokes uncertainty. *Physics of Fluids*, 27(8):085103, 2015. doi:10.1063/1.4927765.

J. Ling, A. Kurzawski, and J. Templeton. Reynolds averaged turbulence modelling using deep neural networks with embedded invariance. *Journal of Fluid Mechanics*, 807:155–166, 11 2016. doi:10.1017/jfm.2016.615.

J.-H. Liu and C.-Y. Song. Efficient suction control of unsteadiness of turbulent wing-plate junction flows. *Journal of Hydrodynamics*, 29(2):353–360, 2017. doi:10.1016/S1001-6058(16)60745-X.

Y. Liu, Z. Duan, and S. Chen. Aerodynamic shape optimization design of wing-body configuration using a hybrid ffd-rbf parameterization approach. In *Journal of Physics: Conference Series*, volume 916, 2017. doi:10.1088/1742-6596/916/1/012001.

T.S. Lund, X. Wu, and K.D. Squires. Generation of turbulent inflow data for spatially-developing boundary layer simulations. *Journal of Computational Physics*, 140:233–258, 1998.

R. D. Mehta. Effect of wing nose shape on the flow in a wing/body junction. *The Aeronautical Journal (1968)*, 88(880):456–460, 1984. doi:10.1017/S000192400001455X.

F. R. Menter. Two-equation eddy-viscosity turbulence models for engineering applications. *AIAA Journal*, 32 (8):1598–1605, 1994. doi:10.2514/3.12149.

J.P. Monty, N. Hutchins, H.C.H. Ng, I. Marusic, and M.S. Chong. A comparison of turbulent pipe, channel and boundary layer flows. *Journal of Fluid Mechanics*, 632:431–442, 2009. doi:10.1017/S0022112009007423.

T. Mukha and M. Liefvendahl. The generation of turbulent inflow boundary conditions using precursor channel flow simulations. *Computers Fluids*, 156:21 – 33, 2017. ISSN 0045-7930. doi:https://doi.org/10.1016/j.compfluid.2017.06.020. Ninth International Conference on Computational Fluid Dynamics (ICCFD9).

T Mukha and M. Liefvendahl. Eddylicious: A python package for turbulent inflow generation. *SoftwareX*, 7: 112 – 114, 2018. ISSN 2352-7110. doi:https://doi.org/10.1016/j.softx.2018.04.001.

T.A. Oliver and R.D. Moser. Bayesian uncertainty quantification applied to RANS turbulence models. *Journal of Physics: Conference Series*, 318(4):042032, dec 2011. doi:10.1088/1742-6596/318/4/042032.

R. Paciorri, A. Bonfiglioli, A. Di Mascio, and B. Favini. Rans simulations of a junction flow. *International Journal of Computational Fluid Dynamics*, 19(2):179–189, 2005. doi:10.1080/10618560410001729126.

J. Paik, C. Escauriaza, and F. Sotiropoulos. On the bimodal dynamics of the turbulent horseshoe vortex system in a wing-body junction. *Physics of Fluids*, 19(4), 2007. doi:10.1063/1.2716813.

S. Peigin and B. Epstein. Aerodynamic optimization of essentially three-dimensional shapes for wing-body fairing. *AIAA Journal*, 46(7):1814–1825, 2008. doi:10.2514/1.35465.

D.B. Philips, J.M. Cimbala, and A.L. Treaster. Suppression of the wing-body junction vortex by body surface suction. *Journal of Aircraft*, 29(1):118–122, 1992. doi:10.2514/3.46134.

F. J. Pierce and J. Shin. The Development of a Turbulent Junction Vortex System (Data Bank Contribution). *Journal of Fluids Engineering*, 114(4):559–565, 12 1992. ISSN 0098-2202. doi:10.1115/1.2910068.

S. B. Pope. A more general effective-viscosity hypothesis. *Journal of Fluid Mechanics*, 72(2):331–340, 1975. doi:10.1017/S0022112075003382.

S. B. Pope. *Turbulent Flows.* Cambridge University Press, 2000. doi:10.1017/CBO9780511840531.

L.F. Richardson. Weather prediction by numerical process. *Quarterly Journal of the Royal Meteorological Society*, 48(203):282–284, 1922. doi:10.1002/qj.49704820311.

M.C. Rife, W.J. Devenport, and R.L. Simpson. An experimental study of the relationship between velocity and pressure fluctuations in a wing-body junction. Technical report, Virginia Polytechnic Institute and State Univ., Arlington, 1 1992.

S. Ryu, M. Emory, G. Iaccarino, A. Campos, and K. Duraisamy. Large-eddy simulation of a wing-body junction flow. *AIAA Journal*, 54(3):793–804, 2016. doi:10.2514/1.J054212.

K.-C. San, Y.-Z. Lin, and S.-C. Yen. Effects of sweep angles and angles of attack on junction-flow patterns. *Journal of Marine Science and Technology (Taiwan)*, 22(2):204–210, 2014. doi:10.6119/JMST-013-0325-1.

D. Sasaki, Y. Yang, and S. Obayashi. *Automated Aerodynamic Optimization System for SST WIng-Body Configuration.* doi:10.2514/6.2002-5549.

H. Schlichting. *Boundary-Layer Theory.* Springer-Verlag Berlin Heidelberg, Berlin, 9 edition, 2017. ISBN 978-3-662-52917-1.

M. Schmelzer, R.P. Dwight, and P. Cinnella. Machine learning of algebraic stress models using deterministic symbolic regression, 2019.

F.G. Schmitt. About boussinesq's turbulent viscosity hypothesis: historical remarks and a direct evaluation of its validity. *Comptes Rendus Mécanique*, 335(9):617 – 627, 2007. ISSN 1631-0721. doi:https://doi.org/10.1016/j.crme.2007.08.004.

C. Seal and C. Smith. The control of turbulent end-wall boundary layers using surface suction. *Experiments in Fluids*, 27:484–496, 11 1999. doi:10.1007/s003480050373.

T. Shizawa, S. Honami, and M. Yamamoto. Experimental study of horseshoe vortex at wing/body junction with attack angle by triple hot-wire. In *34th Aerospace Sciences Meeting and Exhibit*, 1996.

R.L. Simpson. Junction flows. *Annual Review of Fluid Mechanics*, 33:415–443, 2001. doi:10.1146/annurev.fluid.33.1.415.

A. P. Singh and K. Duraisamy. Using field inversion to quantify functional errors in turbulence closures. *Physics of Fluids*, 28(4):045110, 2016. doi:10.1063/1.4947045.

W. Song and P. Lv. Two-level wing-body-fairing optimization of a civil transport aircraft. *Journal of Aircraft*, 48(6):2114–2121, 2011. doi:10.2514/1.C031472.

S.K.R Srikumar. LES of a novel wing/body junction: Anti-fairing. Master's thesis, Delft University of Technology, Faculty of Aerospace Engineering, 9 2019.

W. Tape and C. Tape. Angle between principal axis triples. *Geophysical Journal International*, 191(2):813–831, 11 2012. ISSN 0956-540X. doi:10.1111/j.1365-246X.2012.05658.x.

B. Tracey, K. Duraisamy, and J. Alonso. *Application of Supervised Learning to Quantify Uncertainties in Turbulence and Combustion Modeling.* 2013. doi:10.2514/6.2013-259.

B.W. Van Oudheusden, C.B. Steenaert, and L.M.M. Boermans. Attachment-line approach for design of a wing-body leading-edge fairing. *Journal of Aircraft*, 41(2):238–246, 2004. doi:10.2514/1.353.

A. W. Vreman. The filtering analog of the variational multiscale method in large-eddy simulation. *Physics of Fluids*, 15(8):L61–L64, 2003. doi:10.1063/1.1595102.

Q. Wang and E. Dow. Quantification of structural uncertainties in the k -w turbulence model. 04 2011. doi:10.2514/6.2011-1762.

J. Weatheritt and R. Sandberg. A novel evolutionary algorithm applied to algebraic modifications of the rans stress–strain relationship. *Journal of Computational Physics*, 325:22 – 37, 2016. ISSN 0021-9991. doi:https://doi.org/10.1016/j.jcp.2016.08.015.

D.H. Wood and R.V. Westphal. Measurements of the flow around a lifting-wing/body junction. *AIAA Journal*, 30(1):6–12, 1992. doi:10.2514/3.10875.

H. Xiao, J.L. Wu, J.X. Wang, R. Sun, and C.J. Roy. Quantifying and reducing model-form uncertainties in reynolds-averaged navier–stokes simulations: A data-driven, physics-informed bayesian approach. *Journal of Computational Physics*, 324:115 – 136, 2016. ISSN 0021-9991. doi:https://doi.org/10.1016/j.jcp.2016.07.038.

S. Xu, S. Timme, O. Mykhaskiv, and J.-D. Müller. Wing-body junction optimisation with cad-based parametrisation including a moving intersection. *Aerospace Science and Technology*, 68:543–551, 2017. doi:10.1016/j.ast.2017.06.014.

J.S. Yi and C. Kim. Design optimization of vortex generators for a junction vortex of wing-body configuration by discrete adjoint approach. In *51st AIAA Aerospace Sciences Meeting including the New Horizons Forum and Aerospace Exposition 2013*, 2013.

S.M. Ölcmen and R.L. Simpson. An experimental study of a three-dimensional pressure-driven turbulent boundary layer. *Journal of Fluid Mechanics*, 290:225–262, 1995. doi:10.1017/S0022112095002497.